

Fundamental Studies on the Blow Forming of Polymeric Micro-Tubes and Components

DOCTORAL THESIS

Presented in Partial Fulfilment of the Requirements for the
Doctoral Degree of Philosophy (PhD) in the Faculty of Engineering of
The University of Strathclyde, Glasgow Scotland, UK

By

Gerald Njiribeako Anyasodor

Advisors

Prof. Dr. Yi Qin, Strathclyde, Scotland, UK
Prof. Dr. Christoph. Hartl, Cologne, Germany

Department of
Design, Manufacture and Engineering Management
University of Strathclyde

2014

This thesis is the result of original research by the author. The thesis was composed by the author and has not been previously submitted for examination that led to the award of a degree.

The copyright of this thesis belongs to the author under the terms of the United Kingdom Copyright Acts as qualified by University of Strathclyde Regulation 3.50. Due acknowledgement must always be made of the use of any material contained in, or derived from this thesis.

Signed:

Date:

Dedicated to the loving memory of my beloved parents:

Columba Arima Anyasodor

Janet Adaku Anyasodor (nee Enwere)

Acknowledgements

First, I would like to thank Professor Christoph Hartl, my supervisor at the Cologne University of Applied Sciences in Germany, for his support and advice throughout the research and as research assistant in Cologne. I truly appreciate his kind and genuine interest in my succeeding in research and engineering. He pushed this work to the cutting edge. His passion for perfection and brilliant inputs were the main basis in this research. Thank you!

My sincere gratitude equally goes to Professor Yi Qin, my supervisor at the University of Strathclyde, Glasgow UK, who suggested the idea of coming to Glasgow and greatly encouraged me to pursue a PhD program at the Design, Manufacture and Engineering Management (DMEM) Department of University of Strathclyde in Glasgow. He never doubted my ability and potential. His constructive and enviable professionalism were vital in this research. Thank you!

Their invaluable assistance in technical areas and personal development will always be remembered.

A special note of thanks goes to the Cologne University of Applied Sciences POLYTUBES TEAM, colleagues, professors and staffs at the Institute of Production, Cologne University of Applied Sciences, Germany for all the supports and words of encouragement in this research work and during my employment as research assistant at the institute.

Further, I would like to thank the following departments and partners for their technical supports:

- Cologne University of Applied Sciences, Optic Institute and Central Mechanical Workshop
- All project partners in EU 7th Framework Programme Project, POLYTUBES, especially Swerea IVF AB, Mölndal, Sweden for supplying the PET and PC micro-tube prototypes, Imperial College London, UK for the dynamic mechanical analysis (DMA) experiments on the polymeric micro tubes and Pascoe Engineering Ltd Scotland, UK for the manufacture of die-inserts used in the study cases. In addition, I would like to acknowledge EU 7th Framework Programme Project, which made this research work possible

Finally, I wish to express my deepest gratitude to my brothers Charles, Evaristus, Stanley, Peter, Augustine, Andrew, my only sister Helen, nephews and nieces, who were my source of courage and strength during the difficult periods.

Table of Contents

Acknowledgements	i
Table of Contents	ii
List of Figures	v
List of Tables	x
Nomenclature	xii
Publications	xvii
Abstract	xviii
1. Introduction	1
1.1 Background.....	1
1.2 Aim and Objectives of the Study.....	2
1.3 Study Methodology	2
2. Literature Review	4
2.1 Polymers	4
2.1.1 Introduction.....	4
2.1.2 Classification of Polymers	5
2.1.3 Mechanical Properties of Thermoplastics.....	9
2.2 Manufacturing in Micro Technology of Polymer Forming.....	10
2.2.1 Introduction.....	10
2.2.2 Micro Products/Components and Applications	11
2.2.3 Micro Manufacturing Processes	12
2.2.4 Micro Manufacturing Equipment for Polymeric Micro Components	12
2.2.5 Polymeric Materials for Micro Manufacturing.....	14
2.2.6 Design Considerations for Micro Manufacturing	14
2.2.7 Development Issues in Micro Manufacturing	15
2.3 Micro Blow Moulding	15
2.3.1 Introduction.....	15
2.3.2 Process Design Considerations in Micro Blow Moulding.....	16
2.3.3 Forming Equipment in Micro Blow Moulding	18
3. Process Concepts for the Forming of Polymeric Micro Tubes	20
3.1 Introduction.....	20
3.2 Process Concept in Forming of Polymeric Micro Tubes	20

4.	Theories of Polymer Forming -----	27
4.1	Introduction-----	27
4.2	Deformation Behaviour of Thermoplastic Polymers -----	28
4.3	Yield Criteria -----	34
4.4	Plastic Forming -----	42
4.5	Hardening Laws-----	44
4.5.1	Isotropic Hardening -----	46
4.5.2	Kinematic Hardening -----	47
4.6	Temperature and Strain Rate Dependences of Yield -----	49
4.7	Instability -----	52
4.7.1	Necking -----	52
4.7.2	Strain Softening -----	54
5.	Dynamic Mechanical Analysis (DMA) -----	56
5.1	Introduction-----	56
5.2	Determining Glass Transition Temperature T_g of Polymeric Micro Tubes using DMA-----	57
5.3	DMA Experiments with the Polymeric Micro Tubes -----	61
5.3.1	Materials -----	61
5.3.2	Experimental Methods -----	64
5.3.3	Experimental Results and Discussion -----	66
6.	Free Forming Experiments -----	69
6.1	Introduction-----	69
6.2	Free-Forming Experiments with Polymeric Micro Tubes -----	70
6.2.1	Materials and Sample Geometry -----	70
6.2.2	Experimental Equipment -----	73
6.2.3	Experimental Method and Plan -----	82
6.3	Results and Discussion-----	85
6.4	Failures Classification in Free Formed of Polymeric Micro Tubes -----	97
7.	Calibration of a Constitutive Model -----	103
7.1	Introduction-----	103
7.2	Material Flow Stress Law -----	103
7.3	Constitutive Model Parameter Identification -----	104
7.4	Calibrated Model -----	104
8.	Prediction of Micro-Tube Free-Forming Process -----	106
8.1	Introduction-----	106
8.2	Numerical Modelling -----	106
8.3	Results and Discussion-----	109
9.	Forming Limit Prediction of the Free-Forming of	

PET Micro Tubes -----	116
9.1 Introduction-----	116
9.2 Forming Limit Prediction Concept-----	117
10. Case Study-Forming of Tubular Micro-Components	
and Conclusions -----	120
10.1 Machine Concept for the Forming of Tubular Polymeric	
Micro-Components-----	120
10.2 Micro Blow Moulding Machine for Polymeric Micro Tubes -----	122
10.3 Case Study-Polymeric Tubular Micro-Components-----	123
10.4 Conclusions-----	124
11. Contribution to Knowledge and Suggestions for Future Work -----	128
12. List of References -----	130
A. Appendix -Materials Properties at Room Temperature [9, 99 and 108-114] ----	A-1

List of Figures

- Figure 1** Chemical structure of important polymers: (a) Polyethylene terephthalate PET, (b), Polyamide PA and (c) Polycarbonate PC. The index n_L denotes the repeat of the monomer according to the degree of polymerization and R represents an arbitrary molecular chain [13]----- 4
- Figure 2** Schematic representations of polyethylene (PE) polymer: (a) linear, (b) branched, and (c) cross-linked. Two chains are chemically bonded together at cross-link point [15, 16]----- 6
- Figure 3** Schematic drawing of the crystalline regions in a polymer [12]: (a) Crystalline region (lamellar chain-folded crystallite) [12, 17], and (b) Alignment of polymer chains in the crystalline region [12] ----- 7
- Figure 4** Structure of spherulites. The crystalline regions in a spherulite are arranged radially, starting from a centre point, with the folded chain molecules being oriented tangentially. In between the crystalline regions the material is amorphous [12]: (a) Schematic structure [12, 18], and (b) Macrograph [12] - 7
- Figure 5** Influence of the amorphous structure on the macroscopic mechanical behavior in terms of stress-strain curves. Measured Von Mises equivalent stress against equivalent strain under uniaxial tension, uniaxial compression and pure shear loads for an amorphous polymer Polycarbonate/Acrylonitrile Butadiene Styrene (PC/ABS) [22]----- 8
- Figure 6** Terminology and relative size for microsystems and related technologies [23]----- 11
- Figure 7** Process configuration of micro blow forming process ----- 21
- Figure 8** Process Control Configuration to form Polymeric Micro Tubes: (a) Concept 1 and (b) Concept 2 ----- 23
- Figure 9** User Interface or Front Panel of the LabVIEW Software implementation of the Free Blow Forming Configuration----- 25
- Figure 10** E-modulus versus Temperature for a model polymer. T_g is the glass transition temperature [13, 71]----- 28
- Figure 11** Spring-damper representations of polymer behaviour: (a) Maxwell model (b) Kelvin-Voigt model and (c) 3-Parameter linear solid model [15]----- 29
- Figure 12** Basic features of the stress-strain behavior of PET [58]----- 30

- Figure 13** (a) Schematic representation of the breakdown of the total resistance into an intermolecular resistance occurring in parallel with a network resistance, (b) Elastic-viscoplastic representation of the intermolecular resistance acting in parallel with a time and temperature dependent network, and (c) The network resistance is modeled as a network orientation process and a molecular relaxation process acting together to accommodate deformation [58] ----- 31
- Figure 14** Deformation of a material line element with length $d\xi$ into a spatial line element with length dx [12]----- 32
- Figure 15** Definition of the yield point as the point of intersection of two tangent lines on the load-elongation curve. σ_Y is the yield stress of a thermoplastic polymer [81]----- 35
- Figure 16** Yield surface for a state of plane stress. If the stress state reaches the yield surface, yielding occurs----- 37
- Figure 17** Shear stress versus strain curves for PMMA showing fracture envelope. The “x”, represents fracture points and black-spots “•”, show yield points [83] -- 38
- Figure 18** Von Mises yield criterion including a hydrostatic stress term: σ_{YT} tensile stress at yield and σ_{YC} compressive stress at yield----- 40
- Figure 19** Schematic yield loci in thermoplastics resulting from shear band and craze formation [22]----- 41
- Figure 20** Illustration of No hardening in a tensile test: (a) Perfectly plastic and elastic (b) Rigid perfectly plastic ----- 45
- Figure 21** Isotropic hardening: (a) Evolution of the yield surface (b) Stress versus strain curve with reversed load for an isotropically hardening material [12]----- 46
- Figure 22** Kinematic hardening: (a) Shift of the yield surface caused by kinematic hardening (b) Stress-strain curve for reversed with low hardening material (c) Stress-strain curve for reversed with strong hardening material [12]----- 48
- Figure 23** The measured ratio of yield stress to temperature as a function of the logarithm of strain rate for polycarbonate PC in a tensile test. “o”, represents measured data and the set of parallel straight lines are calculated from Equation 42 [15]----- 51
- Figure 24** Construction by Considère. The point d, which is a maximum on the engineering stress curve, σ_n , is also a tangent from the point $l_e = 0$ on the true stress curve [97]----- 53
- Figure 25** Schematic true stress versus nominal strain curves for amorphous

glassy polymers -----	54
Figure 26 DMA curves for polycarbonate at several frequencies [105] -----	60
Figure 27 Thermal Analysis Equipment Model Q800 from TA Instruments -----	65
Figure 28 Evolution of Storage Modulus E' and Loss Modulus E'' and $\tan \delta$, as a function of Temperature for the PET Tubes Materials of different Dimensions -----	66
Figure 29 Evolution of Storage Modulus E' and Loss Modulus E'' and $\tan \delta$, as a function of Temperature for the PA 6 Tubes Material -----	67
Figure 30 Evolution of Storage Modulus E' and Loss Modulus E'' and $\tan \delta$, as a function of Temperature for the PC Tubes Material-----	68
Figure 31 (a) PET Micro Tube Coil, $d_{a0} = 1.02$ mm and $s_0 = 0.125$ mm (b) PA 6 Micro Tube Coil (supply length 5m), $d_{a0} = 1.34$ mm and $s_0 = 1$ mm -----	70
Figure 32 Schema of the Polymeric Micro Tube Cut Section-----	71
Figure 33 Material: PET micro tube section with tagged measuring points, desired dimension: $d_{a0} = 1.02$ mm and $s_0 = 0.125$ mm. Cut Section length $L_0 = 45$ mm -----	71
Figure 34 The Free Forming Experimental Equipment and Platform-----	73
Figure 35 Schematic of the Connections for the Process Pressurization Module -----	75
Figure 36 Micro Infrared (IR) Heaters. Model MSH/20 -----	76
Figure 37 Typical Transmission Characteristics of Filters from Thorlabs GmbH, Gemany -----	78
Figure 38 Image Grabbing Sub-Module: Illustration of the Elements of the Illuminant -----	79
Figure 39 IR-Radiators Calibration: Thermal Image of Temperature Distribution with IR-Camera and Thermo Sensing Element at the Centre-Line of a clamped Micro Tube -----	80
Figure 40 IR-Radiators Calibration: Temperature Sensing of the Micro Tube Surface with Thermo Sensing Element; (a) PET Micro Tube (b) PA 6 Micro Tube -----	81

Figure 41 Schema of the Experimental Method for the Free Forming of the Micro Tubes -----	83
Figure 42 Digital Image Correlation Technique in the Free Forming Experiments: (a) Initial Dimensions of the Tagged Measuring Point; d_{r0} Dimension in the Hoop Direction and d_{z0} Dimension in the Axial Direction (b) Dimensions at Time t -----	84
Figure 43 Stretch Ratio λ and the Maximum Internal Pressure p_{imax} versus Time t development for PET1 Tube Material: $p_{imax} = 1$ bar, Process Control Prog_01 -----	86
Figure 44 Stretch Ratio λ and the Maximum Internal Pressure p_{imax} versus Time t development for PET1 Tube Material: $p_{imax} = 2.5$ bar, Process Control Prog_01 -----	88
Figure 45 Stretch Ratio λ and Maximum Internal Pressure p_{imax} versus Time t development for PET1 Tube Material: $p_{imax} = 3$ bar, Process Control Prog_01 -----	90
Figure 46 Stretch Ratio λ and Internal Pressure p_{imax} versus Time t development for PET1 Tube Material: $p_{imax} = 6$ bar, Process Control Prog_02 -----	92
Figure 47 Comparison of the True Strain Rates $\dot{\epsilon}$ versus Stretch Ratio λ for the different Experiments -----	95
Figure 48 (a) Schematic Crazing Deformation Mechanism in Poly (methylmethacrylate) PMMA [143]. (b) Crazing Failure of PET134 Tube Material: $d_{a0} = 1.34$ mm and $s_0 = 1$ mm, $p_{imax} = 4$ bar and Process Control Prog_02 -----	100
Figure 49 Local Ductile Failure in the Free Forming Experiment. Tube Material PA 6: $d_{a0} = 1.34$ mm and $s_0 = 1$ mm, $p_{imax} = 6$ bar and Process Control Prog_02 -----	101
Figure 50 Yield Curves based on Equation 57 for different True Strain Rates $\dot{\epsilon}$ and at Constant $T = 93$ °C -----	105
Figure 51 FE Analyses Model for the PET1 Micro Tube: $d_{a0} = 1.34$ mm and $s_0 = 1$ mm and $L_0 = 5$ mm -----	107
Figure 52 Stretch Ratio λ versus Time t development in the FE Analysis of the Experiment: $p_{imax} = 1$ bar and Process Control Prog_01. Tube Material: PET1-----	110

Figure 53 Stretch Ratio λ versus Time t development in the FE Analysis of the Experiment: $p_{imax} = 2.5$ bar and Process Control Prog_01. Tube Material: PET1-----	111
Figure 54 Stretch Ratio λ versus Time t development in the FE Analysis of the Experiment: $p_{imax} = 3$ bar and Process Control Prog_01. Tube Material: PET1-----	112
Figure 55 Stretch Ratio λ versus Time t development in the FE Analysis of the Experiment: $p_{imax} = 6$ bar and Process Control Prog_02. Tube Material: PET1-----	113
Figure 56 Comparison of the Normalised True Strain Rates $\dot{\epsilon}$ versus Stretch Ratio λ for the FE Analyses and the Experiments: $p_{imax} = 1, 2.5, 3$ and 6 bar with Process Controls Prog_01 and Prog_02. Tube Material: PET1-----	114
Figure 57 Uncoupled Approach to Predict Forming Limit in Polymer Forming using Criterion of Brozzo-----	118
Figure 58 Critical Values C_f versus Stretch Ratio λ development. Tube Material: PET1 Tube-----	119
Figure 59 Design concept considerations of the test equipment layout-----	120
Figure 60 Micro Blow Moulding Machine System-----	122
Figure 61 Demonstrators to validate Mould-Insert Blow Forming Process of Polymeric Micro Tubes: (a) Material PET; Fluidic Connector (b) Material PET; Micro Heat Exchanger Housing (c) Material PA 6; Component for a Sperm Cell Separator Device-----	123

List of Tables

Table 1 Selected Polymeric Materials Properties at room Temperature [18, 99 and 108-114] -----	62
Table 2 Polymer Micro Tube Dimensions and Conditions for the DMA Experiments with Q800 -----	65
Table 3 Dimensions of the Micro Tubes Investigated in the Free-Forming Experiments -----	70
Table 4 Deviations recorded across the Coil Section of the PET Tube Material with Supplied Dimensions: $d_{a0} = 1.02$ mm and $s_0 = 0.125$ mm -----	72
Table 5 Calibration results of the Micro IR-Radiators -----	82
Table 6 Experimental Plan to Investigate Formability of the Micro Tubes -----	84
Table 7 Zones illustrated in Figure 43 with associated Images, Instabilities and Failure Mode -----	87
Table 8 Zones illustrated in Figure 44 with associated Images, Instabilities and Failure Mode -----	89
Table 9 Zones illustrated in Figure 45 with associated Images, Instabilities and Failure Mode -----	91
Table 10 Zones illustrated in Figure 46 with associated Images, Instabilities and Failure Mode -----	93
Table 11 Comparison of the different Experimental Results for Tube Material PET1 -----	96
Table 12 Tensile Force F_z Effects on the Formability of PET1 Tube Material at $p_{imax} = 4$ bar -----	97
Table 13 Evolution of the Ductile Failure in PET1 Tube Material. Experiment: $p_{imax} = 6$ bar and Process Control Prog_02-----	99
Table 14 Material Parameters obtained from the Regression Analyses of the Biaxial Experimental Data for PET Films in [51] -----	105
Table 15 PET Material Elastic Behaviour Data for the FE Analyses [57, 99] -----	107

Table 16 FE Analyses Solution Procedure for the PET1 Tube Material-----	109
Table 17 Comparison of the Maximum Stretch Ratios λ_{max} recorded for the Experiments and the FE-Analyses for Tube Material PET1 -----	115
Table 18 Forming Parameters for the Demonstrators [153] -----	124

Nomenclature

List of Symbols

Alphabetic Symbols

a	material constant
A	area
A_1	material constant
A_f	material constant
b	material constant
b_0	width of a barrier
C_f	critical value
C_{fmax}	maximum critical value
c_p	specific heat capacity
\mathbf{C}	Cauchy-Green strain tensor
d_m	mean micro tube diameter
d, d', l_e	points or absolute value
d_{a0}	initial outer diameter
d_{i0}	initial inner diameter
d_{at}	micro tube outer diameter at time t
d_{rt}	measuring point value in the radial direction at time t
d_{zt}	measuring point value in the axial direction at time t
D_f	ductile fracture or damage function
$E, E_1, \text{ and } E_2$	E-modulus
E'	storage modulus
E''	loss modulus
e	engineering strain
F_z	tensile force
F_s	seal force
F_c	closing force
\mathbf{F}	deformation gradient tensor
\mathbf{F}_A	deformation gradient tensor part a
\mathbf{F}_B	deformation gradient tensor part b
f	function
G	shear modulus
g	function
G'	shear storage modulus
G''	shear loss modulus

h_e	initial stiffness slope
h_f	hardening slope
i	principal spatial directions enumerations: 1, 2 and 3
J	Jacobian matrix (determinant)
J_A	Jacobian matrix (determinant) part a
J_B	Jacobian matrix (determinant) part b
k	Boltzmann constant
k_0	material constant
l, l_e	length
l_0, L_0	initial lengths
l_i	deformed length
$m_1 - m_8$	material parameter
m	mass
\dot{m}_1, \dot{m}_2	mass flow rate
n_L	number of monomers
n	hardening parameter
p	hydrostatic stress
p_i	internal pressure
p_{i0}	initial internal pressure
p_{imax}	maximum internal pressure
P_{r0}	probability
P_{r1}	total probability
Q	activation energy
\dot{Q}	heating rate
r	radial direction
R	universal gas constant
\mathbf{R}	rotation tensor
S_{ij}	true stress deviator
s_0	initial micro tube wall thickness
s_t	micro tube wall thickness at time t
t	time
t_o	total forming time
t_h	heat-up time
t_p	pressurization time
t_R	relaxation time
t_q	quenching time
T_0	room temperature
T_g	glass transition temperature
T_m	melting temperature
T, T_f	working temperature
\mathbf{U}	right stretch tensor

\dot{V}	volume flow rate
V	volume
W	work done
$d\mathbf{x}$	length of spatial line element
Y	material constant
Z	axial direction

Greek Symbols

α_{ij}	back stress (kinematic hardening)
α_p	coefficient of thermal expansion
Γ	scale factor
γ	relaxation time
δ	phase angle
δ_{ij}	Kronecker's delta
$p\delta_{ij}$	spherical or hydrostatic stress tensor
Δ	delta
ε	strain field
ε_{ij}	Ludwik-Hencky strain
$\varepsilon_s, \varepsilon_{s1}, \varepsilon_{s2}$	strains in spring
ε_d	strain in damper
ε^e	elastic strain
ε^p	plastic strain
$d\varepsilon_{ij}^p$	small increment of plastic strain
$\bar{\varepsilon}^p$	effective plastic strain
$\bar{\varepsilon}$	von Mises (effective) strain
$\dot{\varepsilon}$	strain rate
η	damper viscosity
λ	stretch ratio
λ_{max}	maximum stretch ratio
λ_i	stretch vector
λ_p	coefficient of heat transfer
$\dot{\lambda}$	stretch ratio rate
$\dot{\lambda}_t$	stretch ratio rate at time t
$d\dot{\lambda}$	positive scalar stretch rate
μ	coefficient of internal friction
ν	Poisson ratio
$d\xi$	vector between two adjacent points
π	pi
ρ	density
σ_n	engineering stress

σ_t	true stress
$\sigma, \sigma_0, \sigma_{ij}$	Cauchy stress, true stress
σ'_{ij}	gradient of the yield surface
$d\sigma_{ij}$	stress increment
$\bar{\sigma}$	von Mises (effective) stress
σ_{YT}	tensile stress at yield
σ_{YC}	compressive stress at yield
σ_{UTS}	ultimate strength in tension
σ_{UCS}	ultimate strength in compression
σ_m	mean or hydrostatic stress
σ_f	flow stress in tension
σ_{fr}	flow stress in compression
$\sigma_1, \sigma_2, \sigma_3$	three principal stresses
$\sigma_s, \sigma_{s1}, \sigma_{s2}$	stresses in spring
σ_d	stress in damper
τ	shear stress
$\tau_{23}, \tau_{31}, \tau_{13}$	Cauchy shear stress
τ_{max}	maximum shear stress

Abbreviations

ABS	acrylonitrile butadiene styrene
CAX4R	continuum axisymmetric 4-node, reduced-integration element
CWL	central wavelength
DAQ	data acquisition
DAQMS	Data acquisition monitoring and storage
DIO	digital input and output
DIC	digital image correlation
DIN	deutsches institut für normung
DMA	dynamic mechanical analysis
EDM	electric discharge machining
FE	finite element
FTIR	fourier transform infrared spectroscopy
FWHM	full width at half maximum
HDPE	High-density polyethylene
I/O	input and output
IR	infrared
ISBM	Injection Stretch Blow Molding
LED	light emitting diode
LIGA	lithography, electroplating, and moulding
NI	national instrument
PCI	Peripheral Component Interconnect

Prog_01	process control algorithm-01
Prog_02	process control algorithm-02
PLC	programmable Logic Controllers
PET	polyethylene terephthalate
PETG	polyethylene terephthalate Glycol
PC	polycarbonate
PA	polyamide
PA 6	polyamide 6
PE	polyethylene
PP	polypropylene
PMMA	poly(methyl methacrylate)
TPCD	temperature and pressure calibration devices
WAXS	wide-angle X-ray scattering

Publications

Ch. Hartl, G. Anyasodor, Micro Blow Moulding, chapter in Micro-Manufacturing Engineering and Technology, Edition 2, edited by Y. Qin, submitted and accepted

Gerald Anyasodor, Christoph Hartl, Investigation into fundamentals and machine system design for polymeric micro-tube expansion with pressurized media, Key Engineering Materials, 597, 2013, pp.153-158

Ch. Hartl, G. Anyasodor and J. Lungershausen, Formability of micro-tubes in hydroforming, The 14th international ESAFORM conference on material forming 2011. AIP Conf. Proc. 1353, pp. 529-534 (2011)

C. Hartl and G. Anyasodor, Experimental and numerical investigations into micro-hydroforming processes and machine design, Metal Forming 2010, edited by K. Mori et al., Conference Proceedings, Wiley-VCH Verlag, 2010, pp. 1193-1196

Ch. Hartl, G. Anyasodor, Design and development of a new machine system for the mass manufacture of complex shaped tubular components by micro hydro-forming, 9th International conference and exhibition on laser metrology, machine tool, CMM and robotic performance (LAMDAMAP 2009), 30th June-2nd July 2009, pp. 206-214

C. Hartl, G. Anyasodor, T. Ptaschlik, J. Lungershausen and S. Lippert, Investigation into reduction of die-cavity deflection in micro hydro-forming processes using FEA, International Journal of Advanced. Manufacturing Technology, Springer, June 2009

Ch. Hartl, J. Lungershausen, G. Anyasodor, T. Ptaschlik, Development of tools and machines for micro hydro-forming with improved accuracy, Zeszyty Naukowe, Instytutu Pojazdów, 5(72), 2008, pp. 157-164.

Abstract

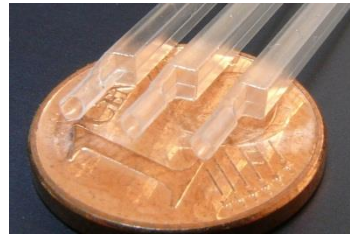
There is increasing demand for micro components in large quantities for medical as well as non-medical applications [1, 2]. To a large extent, the required components are hollow shaped made from polymers such as micro-needles for drug infusion, microfluidic systems for the life-sciences, micro-pumps and fluidic connectors in micro-heat exchanger [2]. However the manufacture of polymeric micro hollow (tubular) components requires innovative and economically competitive micro manufacturing processes. Blow forming processes are based on internal pressurization of an extrusion shaped polymer micro tube could provide an economic and reliable micro manufacturing process to the mass production of precise complex-shaped hollow micro parts. Despite the advantages of blow forming process in conventional polymeric tubes expansion, the application to micro manufacturing has not been investigated to date. This work represents therefore a systematic investigation of the polymeric micro tube blow forming process aimed at providing fundamentals for micro manufacturing applications. Based on reviews of micro forming, conventional stretch blow forming of polymers and other forming processes such as hydroforming, process configuration and machine and tools design consideration were defined. Investigations to miniaturize the design consideration concepts were conducted, which focused on the influences of tube dimensions (handling, flow stress, materials forming limit, instabilities, and friction), quality of extruded polymer micro-tubes, complexity of polymeric material properties, heat distribution and heat transfer in the mold insert, new sealing, and pressurization technique and process cycle-time variations.

Practical experiments supported by numerical analysis formed the basis of the investigations. Experimental investigations were conducted with a flexible-custom designed pneumatic-electric hybrid device, while numerical analyses were FE program based. For systematic blow forming processing tests, process parameters were varied systematically to analyze their influence. The parameters were: temperature (cavity temperature), pressure, elongation compensation force (axial tension), and cycle time. Dimensions of micro tubes used were: initial outer diameter d_{a0} between 630 μm and 1300 μm and initial inner diameter d_{i0} between 500 μm and 1000 μm . Customized software was developed in-house, to implement the expansion process configuration defined. The process software was written in LabVIEW, although data acquisition and control were possible via appropriate hardware interface. In the experiments, the mould was first heated to a polymer processing temperature and other parameters were varied systematically to analyze their influences and interrelations in the process.

The research objectives of a functional demonstrator as shown in the Figure on page II, were achieved through application of precise control of the process parameters. The manufactured machine specifications are: maximum internal pressure of 50 bar, sealing

force 120 N, closing force 132 N and local heating temperature up to 600 °C (heating cartridge 100 Wcm²) and a cycle times variation from 30 to 40 ms (without handling time). Machine design specifications supports processing of polymeric micro tubes with d_{a0} below 1340 μm and d_{i0} below 1000 μm and a tube length of 60 mm. Operation on industrial automation control environment such as programmable logic controllers (PLC) was also supported, to enable integration on micro manufacturing platform for volume manufacture of hollow polymer components

Experimental results conducted with the developed machine showed significant process temperature deviation for a failure free process and part compared to results from the literature for PA 6 and PC micro-tube materials. PET showed less deviation. Achieved suitable process parameters for PET were a maximum internal pressure of 18 bar and working temperature T_f of 90 °C, while optimal parameters to form PA 6 are maximum internal pressure, 15 bars and process temperature of 190 °C. Tube outer diameter of 1300 μm and inner diameter of 1000 μm was used in both cases to achieve maximum formed hoop ratio of 2. Cooling and handling were conducted manually and will require more investigations and refinement to enable integration in a full automated system.



Demonstrator manufactured using Micro Blow Moulding Process: Material PET;
 d_{a0} : 1340 μm, s_0 : 170 μm

1. Introduction

1.1 Background

Many medical applications as well as non-medical applications of consumer goods show an increasing demand for hollow complex shaped micro-sized products with dimensions below 1000 μm . These applications have increased a worldwide trend towards miniaturization and the demand for the manufacture of polymer micro components in recent years [2, 3-6]. The development of new products in the automotive sector, optical industry, telecommunication and electronics, medical and biomedical industry has stimulated the rapid growth in micro system technology.

For these technologies, constant increases in the challenge exist to create reliable fundamentals for an industrial large scale production of micro products. Manufacturing systems that are reliable and economical remain the main focus in the development of micro systems technology for volume manufacture of micro components. To introduce micro products to a large market it is imperative to develop materials, processes and manufacturing technologies that can support an industrial production.

Polymer materials show a great potential for volume manufacture of micro components due to the availability of vast varieties of polymer materials that can be tailored to provide the desired processing and application properties. Currently available production techniques of micro hollow parts made from polymeric materials are predominantly based on injection stretch injection blow moulding.

A wide range of conventional hollow macro products are manufactured today by injection stretch injection blow moulding for polymeric parts and hydroforming for metallic parts [7]. Despite the advantages of injection stretch blow moulding process in the manufacture of conventional polymeric hollow parts, their applications to micro manufacturing has not been much investigated to date.

In contrast to the forming of polymeric micro tubes, for the forming of hollow micro parts made of metallic materials, the required fundamentals to conduct the production process and to design suitable tools and machines were already developed and presented in [8] for an application to micro tubes with an initial outer diameter d_{a0} of 800 μm . Although several medical applications, for example based on [9] M. Saab, U.S. Patent 5, 624, 392 (1997), show the feasibility for a down-scaling of the conventional blow moulding process to the small batch manufacture of medical components from polymeric micro tubes.

Beside the work presented in [10] on the forming of polymeric foils with a thickness s_0 below 300 μm under pressurizing media and [11] that investigated medical balloon fabrication using micro stretch blow moulding, no systematic investigations into this process and its application to volume production had been published up to date.

The lack of suitable volume production facilities for micro components made of polymeric materials gave rise to the here presented research work, which consist of the development of a tube expansion process for the shaping as well as the first fundamentals to design tools and production systems for volume manufacturing.

1.2 Aim and Objectives of the Study

Although stretch blow molding process is intensively used for the industrial production of conventional sized polymeric hollow components, their application for mass production in micro manufacturing has not been investigated. The non-availability of any systematic studies to date on stretch blow molding application in the micro manufacturing for large scale production makes this thesis needful.

Therefore, the overall objective is to develop fundamentals for process and tools design to enable large scale manufacture of polymer tubular micro components by blow forming process.

1.3 Study Methodology

Practical experiments and theory formed the basis of the investigations. The experimental investigations were conducted with a flexible-custom designed pneumatic-electric hybrid device, while the theoretical aspect of the work included literature review in micro technologies, and polymeric material and Finite Element (FE) Analysis.

Polymer micro tube with initial outer diameter d_{a0} below 1300 μm and initial inner diameter d_{i0} below 1000 μm were investigated. Polymer materials tested were PET, PA 6, and PC.

There were 6 process parameters identified for the micro blow forming process investigation conducted in this work based on the literature reviews and background knowledge in micro manufacturing technologies. The parameters are: working temperature T_f , internal pressure p_i , tensile force F_z , sealing force F_s , closing force F_c and time t . The time was divided into the following process periods: total forming time t_o , heat-up time t_h , pressurization time t_p , relaxation time t_R and quenching time t_q .

To effectively investigate the parameters and address the design challenges, the experiments were conducted in three stages. The initial stage of the investigations focused mainly on the performance and suitability of the new sealing and pressurization unit developed in this work to address the challenges reviewed on the applicability of conventional injection stretch blow moulding process in micro manufacturing. The following parameters were defined to systematically investigate and quantify the performance: working temperatures T_f for different polymeric micro tubes, sealing force F_s , and tensile force F_z . The tensile force F_z applied externally eliminated stretch rod application in micro manufacturing and offered a suitable multidimensional orientation stretching during blow forming process. The experiments in this stage were

supported by analytical and FE analyses. The choice of air as forming medium in the micro blow forming process in this work was established in this stage. The results of the investigations in the first stage were applied as constants in the second stage of the investigations.

In the second stage of the investigation, the research focused on the process defined adjustable ratio p_{imax}/t_p required for the forming of polymeric tubular micro components. The p_{imax} represents maximum applied internal pressure, while t_p is the pressurization time. To achieve the objective of the second stage investigations, blow forming experimental concepts were defined based on the process concept and configuration presented in Chapter 3. For systematic and repeatable investigations, a process algorithm for software implementation was developed for the blow forming experimental concept. The process algorithm was implemented in LabVIEW programming environment. Cooling and cooling rate investigations were conducted manually in the second stage of the investigations.

Precision is a major requirement in micro manufacturing, which requires evaluation and validation to measure the performance of the micro manufacturing process and micro part quality. The collected process parameters results were analyzed with appropriate engineering tools. Physical measurement and optical assessment of the formed micro part dimensions were also conducted.

The experiments were quantified with the values of evolution of micro tube outer diameter during the free-forming process. A digital camera was used to acquire on-line evolution of the dimensions. The acquired results were post-processed with image software.

In the third and final stage of this fundamental research, the results of the second stage of the investigations were transferred to mould-insert investigations. The systematic approach in the second stage of the investigations enabled easy transfer to the final stage experimentations, where the optimization measure focused mainly on the heating and cooling management with the mould-insert-system. Localized heating strategy was employed in this work due to size-effect associated with polymeric micro-tubes as explained in section 3.2. The investigations in this last stage were validated and quantified with the study case in Chapter 10, the demonstrators namely: Micro heat exchanger housing, fluidic connector, component for sperm cell separator. While micro heat exchanger and fluidic connector parts were manufactured from PET micro tubes d_{a0} 1340 μm and d_{i0} 1000 μm , the component for sperm cell separator was manufactured from PA 6 micro tubes of the same dimensions.

2. Literature Review

2.1 Polymers

2.1.1 Introduction

Polymers are materials of very high molecular weight, which have multifarious applications in society. These materials usually consist of several units (monomers) bounded together by strong primary forces due to covalent bonding, whereas the bonds between the different chains are weaker secondary bonds caused by van der Waals forces. For this reason, chain molecules can be considered as the basic building units of a polymer [12, 13].

Contrary to metals and ceramics, polymers are thus composed of chain molecules as the basic building units. Therefore, their structure is more complicated than that of the other classes of materials [12].

Chain linking, average molecular weight, and morphology define fundamental concepts of polymers [12]. Chain-like molecules made up of a repeating link or monomers characterize polymer materials. Figure 1(a), 1 (b) and 1 (c) represent the monomers of Polyethylene terephthalate PET, Polycarbonate PC and Polyamide PA.

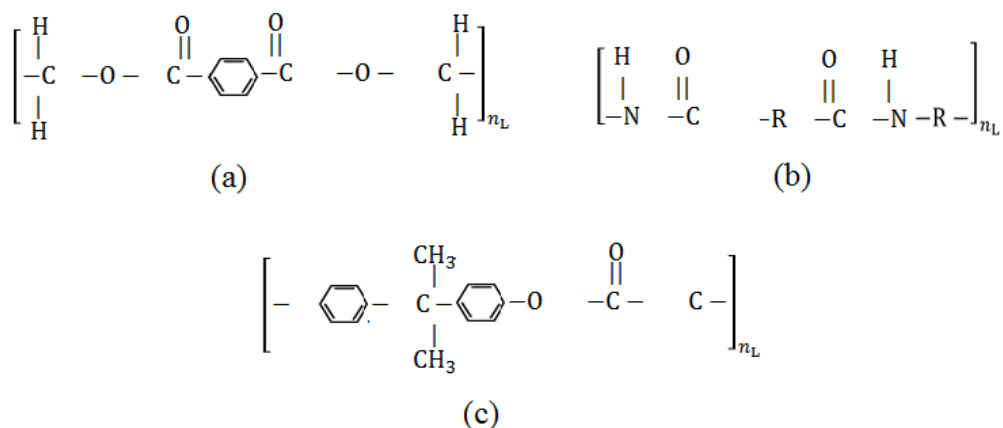


Figure 1 Chemical structure of important polymers: (a) Polyethyleneterephthalate PET, (b), Polyamide PA and (c) Polycarbonate PC. The index n_L denotes the repeat of the monomer according to the degree of polymerization and R represents an arbitrary molecular chain [13]

The number of links n_L , which make up the chain represents the chain length or molecular weight and can vary considerably from one grade to another. Most materials are available in a wide variety of molecular weights, or more correctly, average

molecular weights. Unlike most other materials, polymer material grades do not have a fixed molecular weight, but rather have a distribution of variable chain lengths leading to an average molecular weight [13]. Like molecular weight, the chemical structure of the repeating unit or link will influence the properties of a material. The degree of polymerization (chain length/molecular weight) determines flow properties and also may affect the mechanical properties of a solid polymer indirectly by influencing the final physical state [12, 13]. Two materials with the same average chain length, but different repeating unit structures depicted in Figure 1, will typically have different properties [12]. The study of the structure and properties of materials is applied to polymers in much the same way as it is to metals and ceramics. Morphology is the way that the chains arrange themselves relative to one another. Knowledge of microstructure and morphology are needed to develop relations between the structures and properties of these materials [12, 13].

Polymers have advantages over other types of materials, such as metals and ceramics, because their low processing costs, low weight, and properties such as transparency and toughness form unique combinations with characteristics, such as tensile strength, modulus, elongation, and impact strength that make them more cost effective than metals and ceramics. They are used extensively in food packing, clothing, home furnishing, transportation, medical devices, information technology and others. New technologies have however emerged resulting in novel polymers with highly oriented structures [12, 13].

2.1.2 Classification of Polymers

Polymer could be classified according to the general types of polymerization processes used to produce them or classification based on structure, linear and branched or cross-linked polymers as shown in Figure 2. Classification could also be based on properties namely thermoplastics, elastomers (rubbers) and thermosets (duromer) [14]. Thermoplastic polymers are listed with other materials in the Appendix, to compare the properties of the different materials.

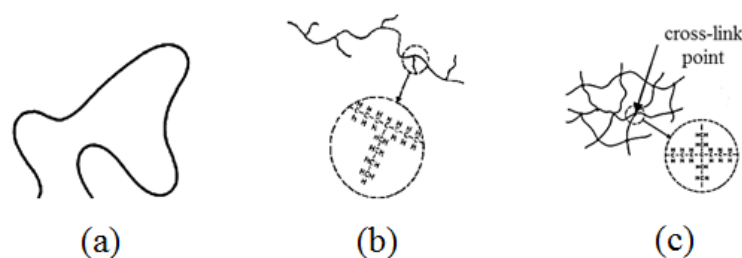


Figure 2 Schematic representations of polyethylene (PE) polymer: (a) linear, (b) branched, and (c) cross-linked. Two chains are chemically bonded together at cross-link point [15, 16]

In linear chains, the repeat units are held by strong covalent forces, while different molecular chains are held together by weak van der Waals forces. Thermoplastics with linear structure include nylons polyvinyl chloride and polyethylene depicted in Figure 2. However, it is possible to covalently cross-link the chains to form molecular network. These cross-links are crucial in determining the mechanical properties of the polymer because they fix the chains relative to each other and thus render it impossible to draw out single chain molecules. Therefore a distinction is drawn between thermoplastics with no cross-linkage, elastomers (or rubbers) with a small number of cross-links and thermosets (duromers) with many cross-links. Classifications based on structure and properties are intimately linked [12, 15]. Hence a description of the types of polymer according to thermoplastic, elastomers (rubbers) or thermosets will be discussed further.

Thermoplastics form the bulk of polymers in use. Thermoplastics soften or melt when heated, so that they can be molded and remolded by heating. Hence they show most promise in moulding processes [16]. In the molten state they consist of a tangled mass of molecules [12, 15]. On cooling they may form glassy state below a temperature called the glass transition temperature, T_g or they may crystallize. If they crystallize they do so only partially forming semi-crystalline, the rest remaining in a liquid-like state which is usually called amorphous or glassy polymers. In general, amorphous polymers have less shrinkage when cooled compared to semi-crystalline polymers [12, 15].

Rubbers, or elastomers, are network polymers that are reversibly stretchable to high extensions. When unstretched they have fairly tightly randomly coiled molecules that are stretched out when the polymer is stretched. This causes the chains to be less random, so that the material has lower entropy, and the retractive force observed is due to this lowering of the entropy. The cross-links prevent the molecules from flowing past each other when the material is stretched. On heating, they cannot melt in the conventional sense, i.e. they cannot flow, because of the cross-links [15].

Thermosets are network polymers with dense three-dimensional network. They are normally rigid. They cannot melt on heating and they decompose if the temperature is high enough. The name arises because it was necessary to heat the first polymers of this type in order for the cross-linking, or curing, to take place. The term is now used to

describe this type of material even when heat is not required for the cross-linking to take place. Examples of thermosets are the epoxy resins, such as Araldites, and the phenol- or urea-formaldehyde resins [15].

Elastomers and thermosets are always completely amorphous because the chemical bonds make a regular arrangement of the chain molecules impossible. Thermoplastics, on the other hand, can be completely amorphous as in glassy polymers or semi-crystalline [19] which contains a mixture of crystalline and amorphous regions [20]. The volume fraction of the crystalline regions in a semi-crystalline thermoplastic is called its crystallinity. In a semi-crystalline thermoplastic, the crystalline regions do not consist of straight chain molecules aligned in parallel, but rather of regularly folded molecules depicted in Figure 3. The crystalline regions typically have a thickness of approximately 10 nm and a length between 1 μm and 10 μm and in between them are amorphous regions. The crystalline regions themselves are frequently arranged radially with gaps filled by amorphous material, forming the spherulites shown in Figure 4 that are analogous to the crystallites in a metal. Their extension is about 0.01 mm to 0.1 mm [12].

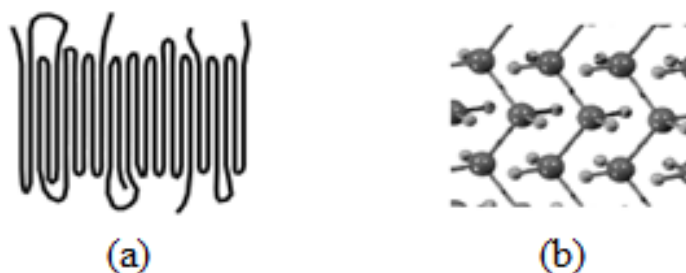


Figure 3 Schematic drawing of the crystalline regions in a polymer [12]: (a) Crystalline region (lamellar chain-folded crystallite) [12, 17], and (b) Alignment of polymer chains in the crystalline region [12]

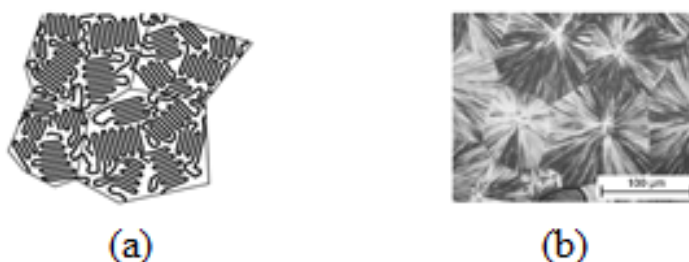


Figure 4 Structure of Spherulites. The crystalline regions in a spherulite are arranged radially, starting from a centre point, with the folded chain molecules being oriented tangentially. In between the crystalline regions the material is amorphous [12]: (a) Schematic structure [12, 18], and (b) Macrograph [12]

The amorphous regions within the spherulite in Figure 4 confer onto the material some flexibility while the crystalline platelets give the material strength, just as in the case with largely amorphous materials. The effect of amorphous flexibility and crystalline strength (and brittleness) is the central idea in polymer structure versus property relationships [13].

Properties of thermoplastics change depending upon temperature [21] as discussed in Chapter 3. Thermoplastics can be amorphous or crystalline once they cool below the melting temperature T_m . The crystallinity in thermoplastics can be introduced by temperature (slow cooling) or by stress-induced crystallization [20, 21].

Crystallization is important in polymers since it affects mechanical and optical properties. Crystallinity evolves in the processing of polymers as a result of temperature changes and applied stress such as in stretch blow molding of PET bottles. Crystallization of the polymer also helps to increase density, resistance to chemical attack, and mechanical properties also at higher temperatures due to the strong bonding between the chains. In addition, deformation straightens and aligns the chains, producing a preferred orientation as in Figure 5. Deformation of a polymer is often used in producing fibers having mechanical properties in the direction of the fiber that exceed those of many metals and ceramics [21].

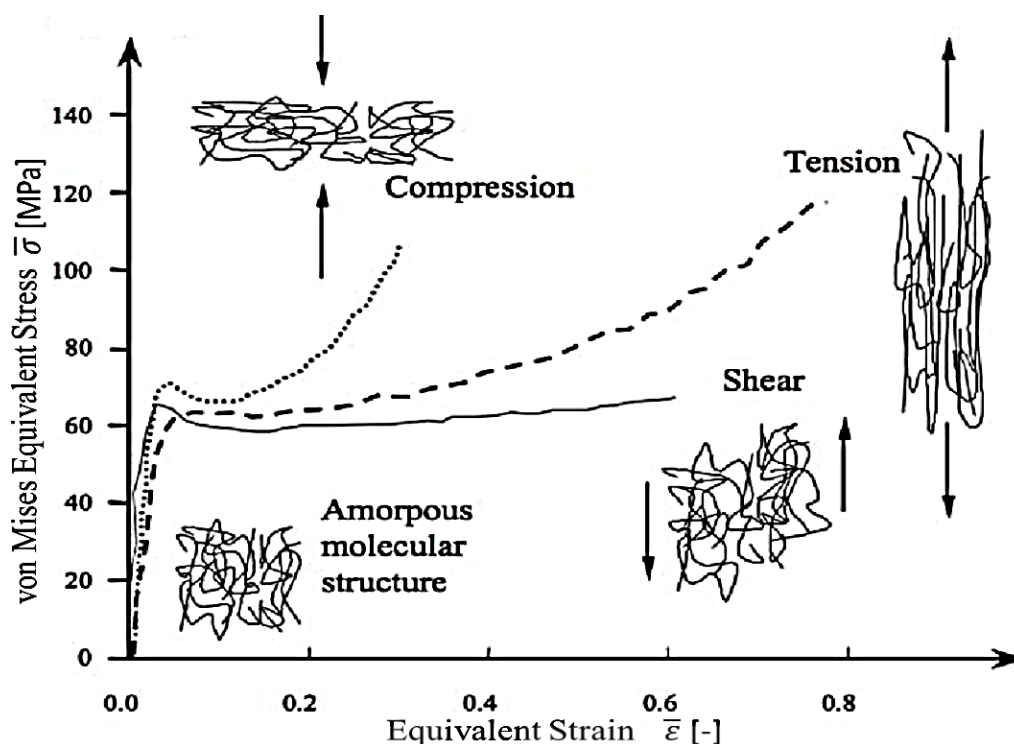


Figure 5 Influence of the amorphous structure on the macroscopic mechanical behavior in terms of stress-strain curves. Measured Von Mises equivalent stress against equivalent strain under uniaxial tension, uniaxial compression and pure shear loads for an amorphous polymer Polycarbonate/Acrylonitrile Butadiene Styrene (PC/ABS) [22]

2.1.3 Mechanical Properties of Thermoplastics

Stress analysis of polymer products is in many ways identical to that of metallic structures. Some mechanical properties of typical thermoplastics are listed in Chapter 4 and Appendix Most thermoplastics (molten and solid) exhibit a non-Newtonian and viscoelastic behavior. Non-Newtonian behaviour means that the stress and strain are not linearly related for most parts of the stress-strain curve. By viscoelastic behaviour when an external force is applied to a thermoplastic polymer, both elastic and plastic (or viscous) deformation occurs. The mechanical behavior is strongly influenced by the morphology of the polymer, which determines the manner in which the polymer chains move relative to one another under load. The deformation process depends on both time and the rate at which the load is applied [22]. Qualitative descriptions of viscoelastic behavior are shown in Chapter 3 using spring-damper or mechanical models.

Elastic Behaviour

Elastic deformation in thermoplastics can be described by two mechanisms: An applied stress causes the covalent bonds within the chain to stretch and distort, allowing the chains to elongate elastically. When the stress is removed, recovery from this distortion is almost instantaneous. This behavior is similar to that in metals and ceramics, which also deform elastically by the stretching of metallic, ionic, or covalent bonds. In addition, entire segments of the polymer chains may be distorted; when the stress is removed, the segments move back to their original positions only over a period of time that can span hours or even months. This time-dependent, or viscoelastic, behavior may contribute to some nonlinear elastic behavior [13, 15].

Plastic Behaviour

Thermoplastic polymers deform plastically when the stress exceeds the yield strength at the deformation temperature. Unlike deformation in the case of metals, however, plastic deformation is not a consequence of dislocation movement. Instead, chains stretch, rotate, slide, and disentangle under load to cause permanent deformation. The drop in the stress beyond the yield point can be explained by this phenomenon. Initially, the chains may be highly tangled and intertwined. When the stress is sufficiently high, the chains begin to untangle and straighten. Necking also occurs, permitting continued sliding of the chains at a lesser stress. Eventually, however, the chains become almost parallel and close together; stronger van der Waals bonding between the more closely aligned chains requires higher stresses to complete the deformation and fracture process. This type of crystallization due to orientation played an important role in the discovery of nylon as a material to make strong fibers [20].

PET bottles formed from semi-crystalline polymer PET develop biaxial orientation and strength along the radial and length direction during processing at elevated temperature. Properties of thermoplastics dependence on temperature is an importance consideration in the choice of polymer for a processing technique or component design.

Creep and Stress Relaxation

Thermoplastics exhibit creep, a time-dependent permanent deformation with constant stress or load as well as stress relaxation. In stress relaxation the stress level decreases with time under a constant strain [20]. Stress relaxation, like creep, is a consequence of the viscoelastic behavior of the polymer [21].

In a simple model, the rate at which stress relaxation occurs is related to the relaxation time γ , which is considered a property of the polymer [21]. The stress after time t is given by Equation 1:

$$\sigma = \sigma_0 \exp\left(-\frac{t}{\gamma}\right) \quad (1)$$

where σ_0 is the original stress.

The relaxation time, in turn, depends on the viscosity and, thus, on the temperature [21]. Relationship between relaxation time γ and temperature T can be developed using Arrhenius activation energy in Equation 2:

$$\gamma(T) = A_1 \exp\left(-\frac{Q}{RT}\right) \quad (2)$$

where A_1 is a constant, R is the universal gas constant, T is the temperature in Kelvin and Q is the activation energy related to the ease with which polymer chains slide past each other. Stress relaxation occurs more rapidly at higher temperatures and for polymers with a low viscosity [21].

2.2 Manufacturing in Micro Technology of Polymer Forming

2.2.1 Introduction

An important trend in engineering design and manufacturing is the growth in the number of products and/or components of products whose features sizes are measured in microns (μm) [23] as well as hollow shaped products [2]. Microsystem technology is a more generally term that refers to miniaturized components as well as the manufacturing technologies used to produce the components mostly in the electronic industry. Figure 6 shows the terminologies, relative sizes and other factors associated with microsystems [23] as well as related technologies. Designing products, which are smaller and comprised of smaller components and sub-assemblies mean less material usage and greater functionality [2, 23]. However, the price of a given product is influenced by the cost of research, development, and manufacturing, and how these costs can be spread over the number of units sold [23].

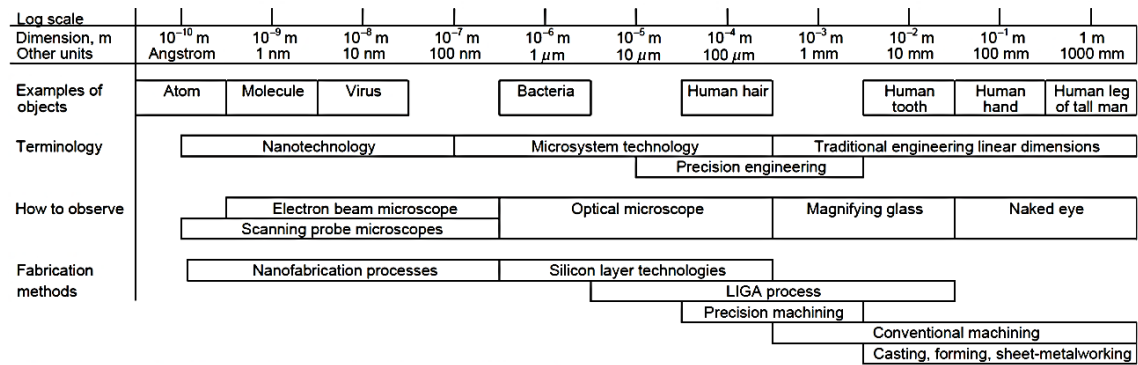


Figure 6 Terminology and relative size for microsystems and related technologies [23]

Micro system products in Figure 6 can be classified by the type of device such as sensor, actuator or as well as by application area like medical or automotive fields [23].

In addition to existing micro manufacturing technologies of silicon or glass-based microsystems, the increasing demand for polymer based devices requires the establishment of equivalent technologies for the manufacture of polymeric micro parts. While many micro optical applications cannot use polymeric materials due to extremely high tolerances, it is especially the quickly growing field of microfluidic systems for the life-sciences, where polymers are the preferred materials. Polymers show high compatibility to many biologically active molecules and living cells [3-5, 24-28 and 31]. Micro manufacturing technologies for polymers can be divided mainly in two classes of products namely semi-finished products or finished products. The shaping of polymer tubes during extrusion or pre-forms in injection moulding represents semi-finished product, while blow moulding applied to manufacture plastic bottles and other geometrical shapes of plastic products represent finished products [2]. Micro blow moulding of thermoplastic polymers is one of the most promising micro manufacturing techniques for non-electronic micro devices [2-6, 24-28 and 31].

2.2.2 Micro Products/Components and Applications

Micro moulding of thermoplastic polymers has great potential for producing low-cost microfluidic devices. Microfluidics is a rapidly growing area with many applications and a strong potential for further development [3].

Examples of polymeric microfluidics include components for micropumps, which are used for medical, chemical and environmental technology [29, 30]. In industry, Bartels Microtechnik [32], for example, is specialised in micropumps for the delivery of small amount of fluids for different applications, such as point-of-care platforms or small fuel cells. The pumps are designed to be low in cost and disposable. Other producers, such as Microfluidic ChipShop [33] produce polymeric microfluidic platforms for medical diagnostics and point-of-care applications [3].

Several micro-components could be integrated together with the appropriate electronics package into a miniature system or instrument. Micro-systems and micro-instruments tend to be very application specific such as micro lasers and optical chemical analysers. The cost of manufacturing of micro devices has made commercialization difficult. Micro devices such as sensors and actuators have wide applications in the automotive industry as in air-bag deployment, and pressure sensors. Heart pacemakers and hearing aids are some applications in the medical field while in biotechnology applications could be in holding, moving, sorting and dissecting devices. Other applications are also found in electronic industry, and in many other technologies [2-6, 23-28, and 31].

2.2.3 Micro Manufacturing Processes

Micro manufacturing process can be defined as precision manufacture of extremely small products as small as one cubic millimetre. Products usually weigh less than 20 milligrams (0.020 g) with some even as low as 0.01 g. Products are measured in microns and have tolerances of ± 10 microns or less. Many of the products in micro-system technology are based on silicon, and most of the processing techniques used in the micro manufacture are borrowed from the microelectronic industry [6]. The application of other different materials to obtain a particular micro device will however require other micro manufacturing techniques more than just the technique applied to silicon processing. Micro manufacturing technologies established over the last years for different materials include lithography, laser-beam, and electric discharge machining (EDM) and micro moulding. The application of a particular manufacturing technique is mostly influenced by many factors such as allowable tolerances and, functional requirements, as well as the volume of manufacture, and cost. Different manufacturing techniques are mostly combined to manufacture a functional product. The trend for volume manufacture has put the focus on those techniques most suitable for large scale manufacturing. The use of micro moulding technique for thermoplastic polymeric materials is increasing in micro manufacturing [2-6, 24-28 and 31].

Some processes which are employed for micro moulding of thermoplastic polymers include: blow moulding, hot embossing, and thermoforming. Injection blow moulding is the most widely used technique in the macroscopic production of polymer parts for decades. The progress made in polymer extrusion and micro injection moulding is enabling rapid growth of micro manufacturing with polymeric materials [2].

2.2.4 Micro Manufacturing Equipment for Polymeric Micro Components

Some micro-manufacturing processes such as that for micro-mechanical machining, micro EDM and micro-metal forming are often realized with large-scale equipment. However the cost of the efforts made to improve the precision of the machine structures for such task, reduces often the advantages of such strategy [1].

Micro manufacturing represents more than down-sizing of conventional processes to include also precise process, machine and tool design, stable and repeatable process at

economical cost. Three critical measures of precision positioning in equipment are control, resolution and repeatability [34]. The problems associated with machines or equipment increases with miniaturization. The clearance or the backlash between the machine parts that are negligible for conventional forming processes may have a detrimental influence on the accuracy of the produced parts [3-6 and 9].

Moulding process technology has inspired several research groups to start thermoplastic molding [2]. The appearance of the Lithographie, Galvanoformung, Abformung (LIGA) technology led to a new challenge in the thermoplastic moulding of micro structures such as the replication of components with complex structures [2]. LIGA is described in english as: Lithography, Electroplating, and Molding.

Currently, the micro injection moulding process offers several advantages in terms of mass manufacturability, variety of materials and accurate replication of micro-scaled features, and it is being used commercially for producing some types of devices. A number of limitations, however, need to be overcome before the wide-scale fabrication of micro components can be realized by micro injection moulding. In particular, the nature of end-shape processes puts limitations on the allowed geometrical designs to ensure smooth demouldability. Moreover, the study and optimization of the process parameters, especially for high aspect ratios features, are essential for producing parts with acceptable quality. The variables, that affect the quality, can be classified into four categories: mould and component design, performance of moulding machine, material, and processing conditions [35].

The aspect ratio, achievable in replicating micro features is one of the most important characteristic of the micro fabrication processes and it constitutes a constraint in applying micro injection moulding [36].

Machines and tooling to manufacture small parts are not just smaller versions of their conventional equipment [3-6, 37]. However, moulding tools used in micro manufacturing generally consist of a micro-structured mould-insert and the tool. This separation is unknown in macroscopic moulding technology. It is due to the completely different requirements to be met by the micro part and by the tool [2]. Proper venting usually has to include precision venting in the mould-insert as well as possibly removing air prior to entering the mould-insert [37]. Venting is usually achieved with small bores in the mould-insert or very small venting slits machined into the mould parting planes. Vacuum assisted forming is a possible aid in venting and shrinkage control. It ensures closer contact with the mould walls, and more rapid cooling [38].

The main problem regarding the tools lies in their manufacturing, especially very small contours in the mould-insert with the required close tolerances and adequate surface quality are difficult to make. However, new manufacturing methods have been developed in order to overcome these difficulties. The development of adequate measuring technology, suited to measure the smallest contours of tools and parts, respectively, is also another challenge [3].

The handling of material and parts is another challenge in micro manufacturing, since the surfaces where they can be gripped are very small and the part weight is low compared with adhesion forces; as a result, the parts do not separate from a gripper by themselves. Additionally, they have to be placed with tolerances of a few microns into a die. The requirement made on machine control is extremely high. Minimal speed of a few microns per second and position control with an accuracy of a few microns even at high forces are necessary. The development and use of small machines could lead to a more economic production [2, 3].

The limitations in micro injection moulding and lack of suitable volume manufacturing process and equipment for hollow parts made from polymeric materials make micro blow moulding manufacturing technology an open research issue. Against this background, this research work therefore addressed the above mentioned challenges in the development of fundamentals for process and tools design to enable large scale manufacture of polymeric hollow micro parts by blow moulding process.

2.2.5 Polymeric Materials for Micro Manufacturing

Material selections in manufacturing are primarily based on the functional requirements of the part [38]. The material behaviour changes with miniaturization, caused by size effects that occur when a process is scaled down from conventional size to the micro-scale. The flow stress, the anisotropy, friction, forming force, the formability and the forming limit of materials are influenced by these size effects, which has to be considered when designing a micro forming process and choosing the material [3, 9, 39 and 40].

Polymers show properties that differ from those of silicon, glass, and metals. Thermal expansion, creep, diffusion, and chemical properties mostly differentiate polymer from these materials. The large thermal expansion of polymers has to be considered when micro parts are to be designed from polymers [2, 3].

Micro moulding of thermoplastic polymers is one of the most promising micro manufacturing techniques for non-electronic micro devices. Manufacturing costs of moulded micro parts are hardly affected by the complexity of the design. The cost of the raw material in most cases is negligibly low, since only small material quantities are required for micro parts. Moreover, thermoplastic materials are a very large material class, which enable wide application of polymeric materials [2, 3].

It should be emphasized that size effects concerning the material and the process have to be considered during the process and equipment design as well as the effect of the applicability of finite element (FE) based analyses [3, 41].

2.2.6 Design Considerations for Micro Manufacturing

Design consideration refers to items involving manufacturing factors without which the part or product cannot be made profitably [38]. Consequently, the design and

development of a new product, a new shape, remains a challenging task for the engineer since several technological and economic requirements must be met [42]. Design considerations are raw material cost, availability of technology for volume production, costs of manufacturing and tooling, recyclability, familiarity with materials already in use, and acceptability in the marketplace. Conformance to standards and codes may also be considered in design [38, 43].

Precision is a major requirement in micro manufacturing, which demands validation to ensure micro manufacturing process performance and micro part quality. The availability of methods, tools and equipment for measurement and test the manufacturing process performance as well as products is a very important consideration in micro manufacturing. Size of components and essential accuracy of the measuring equipment represent some physical obstacles in validation. Validation tools enable designer to set requirements on what can be verified by means of measurement and testing methods, tools and equipment [44].

Operators of machines take steps that will ensure their own safety. All process equipment and tools should have safety devices and procedures to operate and meet safety requirements. Machines for micro manufacturing must be designed, constructed, and used in a manner to prevent hurt, injury, or loss. They are to comply with tighter safety standard [34].

2.2.7 Development Issues in Micro Manufacturing

Most development issues in micro manufacturing have been discussed from Sections 1.2.3 to 1.2.6 above. Despite the challenges in micro manufacturing reviewed above and especially with regards to the application of polymeric material, significant progress in new manufacturing methods for tools is encouraging [3-6, 9, 29-34 and 40].

There have been also significant progresses made in the process control and automation in micro manufacturing. Currently standard microprocessor-controlled machines with closed-loop functions have proved to be suitable for micro-manufacturing. Microprocessor-controlled machines usually give fast and accurate response to operator commands [45].

Nevertheless, some general issues still apply to all sectors in the micro manufacturing, such as how to quickly deploy new technologies and management methods to improve manufacturing capability, efficiency and quality [1].

2.3 Micro Blow Moulding

2.3.1 Introduction

Conventional blow forming has evolved from the ancient art of glass blowing and it is used to advantage with polymeric materials specifically because these materials can be engineered to provide a variety of properties [2]. The automated blow moulding process

as it is known today has seen rapid development during the last century, while at the same time the range of applications and diversity of materials has considerably increased [46]. Also the demand for hollow products with geometric complexity and increased functionality is growing [3-6, 9, 29-34].

In the conventional manufacture of polymeric hollow macro and micro products three main blow moulding techniques can be distinguished: injection blow moulding, extrusion blow moulding and injection stretch blow moulding. Injection stretch blow moulding is the most popular blow molding processes technique used to make thin-walled polyethylene terephthalate (PET) hollow products such as PET bottles and containers compared to other blow molding techniques [47-50]. Conventional Injection stretch blow moulding process have been extensively studied and developed in the last decade [47]. Schmidt et al. in [47] studied the viscoelastic simulation of PET stretch blow moulding process. In [48] investigation of kinematics of stretch blow moulding of PET carried-out. The study in [49] and other studies on stretch blow moulding show the significance and impact of stretch blow moulding process in manufacture of hollow polymeric components.

Thermoplastics such as PET are most widely used material for injection stretch blow moulding. PET is polyester with very low permeability and is strengthened in the injection stretch blow moulding process. At the proper temperature, the preform will be proportionately stretched and oriented. The orientation-induced crystallinity strongly improves the mechanical properties of the formed part [47-51]. The ideal orientation temperature after reheat for injection blow moulding process is 90°C to 120°C. Other thermoplastic applied include High-density polyethylene (HDPE), PA 6, PC and Polypropylene (PP).

2.3.2 Process Design Considerations in Micro Blow Moulding

The comparison of micro forming processes with the conventional shows that some parameters such as the microstructure remain constant when scaling down the dimensions. Beside the challenges that are also known in the field of conventional forming, like tool design, wear and appropriate treatment of the material, problems appear in micro forming that are strongly coupled with miniaturization itself [40]. In the manufacture of macro parts however, manufacturing methods and strategies in micro-manufacturing may be different. Micro manufacturing uses largely non-traditional manufacturing methods, scale-down or appropriately modified traditional methods to adequately address design challenges in micro manufacturing [39]. Dimensional accuracy of the finished part quantifies the manufacturing process and is influenced by the quality of polymeric preform or extruded tube, the accuracy of the mould used, and the process controls as well as behaviour of the polymeric material. These influences have tighter tolerances in the micro processes and parts compared to the conventional processes and macro parts.

Also an important subject concerning the design and manufacture of the moulding tools in micro blow moulding process consist in the determination of a suitable mould parting line and measures for mould-insert venting. Suitable knowledge concerning the tool manufacture in the micro dimensions is of importance to achieve the aimed accuracy of the formed parts. That concerns in particular the design measures for mould-insert venting to avoid air locked between the formed component and mould-insert walls. These issues were addressed in this work to enable manufacture of accurate formed micro part.

In injection stretch blow moulding of macro hollow parts, a tube shaped preform is heated above the glass transition temperature T_g and transferred inside a mould. The preform is stretched longitudinally using stretch rod and blown with air pressure [47] to enable multidirectional stretching or orientation of the preform and ensure part with excellent mechanical and barrier properties part [47-50]. Beside the stretching function, the stretch rod is also part of the process sealing system. The difficulty to insert the stretching rod into polymer micro tubes with an initial internal diameter $d_{i0} \leq 1000 \mu m$ at elevated temperatures will possibly introduce significant imprecision in the blow moulding. In addition the sealing system strategy in the conventional process is unsuitable for micro manufacturing application.

In scaling down conventional blow moulding processes for volume production in micro manufacturing involved concerns not only the reliable handling of the micro tubes and forming tool design, but also a suitable thermal management, The necessary modifications in thermal management as well as the factors that have to be taken into account concerning part removal are caused by so called size effects. These resulted from the increased ratio of the micro tube surface area to its volume A/V . The ratio A/V is relevant for all effects which are dominated by surface effects, in particular concerning heating or cooling, friction and adhesion [39]. For a thin walled micro tube the outer surface area can be determined roughly by Equation 3:

$$A \approx d_m \pi l \quad (3)$$

where d_m is the mean micro tube diameter and l the micro tube length, and the volume is given by Equation 4:

$$V \approx d_m \pi s_0 l \quad (4)$$

where s_0 is the micro tube wall thickness. Hence, for a micro tube with $s_0 \ll d_m$ the surface area to volume ratio can be written as in Equation 5 [39]:

$$\frac{A}{V} \approx s_0^{-1} \quad (5)$$

This means that the importance of size effects will increase with the factor $1/s_0$, when decreasing the part size.

Blow moulding of polymer are carried-out at elevated temperatures in conventional blow forming of polymeric macro parts as well as in micro manufacturing. In conventional processes, this heat energy is either already provided by the extrusion process which delivers the extruded tubes or reheated polymeric tube preforms in temperature chambers and transferred to the mould. A comparable strategy, where the micro tube is provided to the process as a preheated part, was considered not to be feasible for micro tubes. The effect of scaling a thermal system can readily be determined by analysing the basic heat transfer relationships. The thermal energy storage capability for an object is determined by Equation 6 [52, 53]:

$$mc_p\Delta T = \rho Vc_p\Delta T \propto \Gamma^3 \quad (6)$$

where Γ is the scale factor and m is the mass. ρ represents density and ΔT is change in temperature, while c_p is the specific heat capacity.

The mass m of an object is directly proportional to the object volume V as defined in Equation 6. Since the micro tube size is reduced by 1000, thus $\Gamma = 10^{-3}$, the volume and mass are reduced by 10^{-9} [52]. The correlation in Equation 6 indicates that thin walled polymeric micro tubes would be characterized by low heat capacity. A local heating strategy presented in Chapter 5 was employed in this study for the thermal management in micro blow moulding and was a major consideration in the definition of the process concept and configuration in the micro blow moulding process.

2.3.3 Forming Equipment in Micro Blow Moulding

Performance of conventional and micro blow forming equipment has significant influence on the accuracy of parts manufactured. Improvements made over many decades in conventional equipment have significantly increased their performance [6] as well as in micro manufacturing [3-6, 9]. Standard equipment in blow moulding usually consists of blow moulding machine and tools (mould, and blowing rod). Despite the progresses made in the micro blow moulding, many challenges still remain as discussed above.

Design issues for the conventional as well as micro blow moulding equipment and the blow moulding process are interrelated and influenced largely by the behaviour of polymeric materials. Polymers have high thermal expansion coefficients, and significant shrinkage occurs during cooling of the polymers in the mould. Some thermoplastics undergo volumetric contractions of around 10 %. Contraction of crystalline polymers tends to be greater than for amorphous polymers. Higher shrinkage occurs with thicker walls and with higher molecular weight polymers [38] associated with macro parts.

Shrinkage is a major issue with regards to demoulding in conventional and micro moulding processes and require adequate mould and tools design.

3. Process Concepts for the Forming of Polymeric Micro-Tubes

3.1 Introduction

Design concepts presented in this Chapter in forming of polymeric micro tubes addressed the challenges reviewed on micro manufacturing and micro blow moulding technologies. These challenges include thermal management in the process design, mould and tool design for the blow forming equipment. Most significant in the equipment design was the requirement for a suitable sealing and axial stretching strategy to replace the stretch rod in the conventional process. Process control challenges were also addressed to enhance manufacturing capability, efficiency, reduced process cycle time as well as process and part quality. Other process, equipment and control design challenges associated with the scaling down of conventional blow moulding process due to size-effect were also addressed in this Chapter.

To obtain short cycle times for high-volume production, an appropriate design for the forming tools and the thermal management as provided in this work ensured that the heat energy to heat up the next micro tube to be formed was provided within a comparatively short time.

3.2 Process Concept in the Forming of Polymeric Micro-Tubes

In Figure 7 the principle of a micro blow forming process was illustrated, which was developed against the background to transfer blow forming technology to high volume production of polymeric micro components. In this Figure, the polymeric micro tube is positioned between the two moulds halves. These mould halves embed mould-insert for the part shape or geometry. In this position, the micro tube is already sealed, connected with one end to an air pressure supply. The tool elements, which seal the micro tube ends were designed in a way that an axial tensile force F_z was superimposed with the application of the internal pressure p_i .

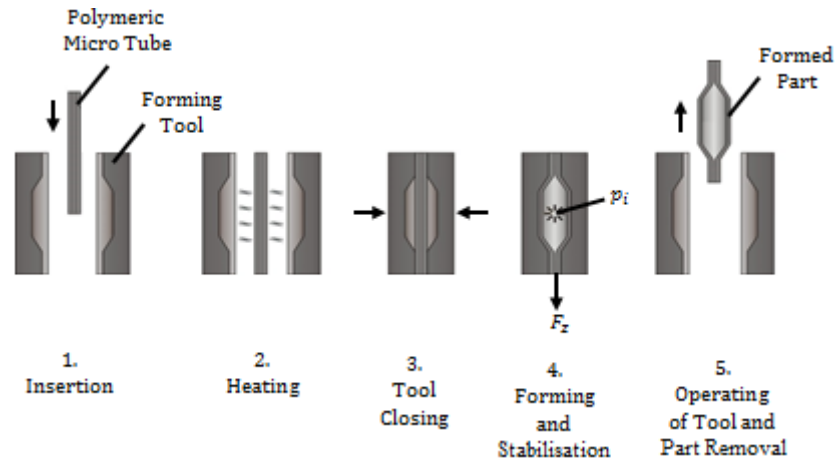


Figure 7 Process configuration of the micro blow forming process

The forming process was started at tools-close, superimposed tensile force F_z and controlled application of the forming loads p_i to expand the micro-tube, until it gets completely in contact with the surrounding mould-insert. The internal pressure was increased to maximum pressure p_{imax} to calibrate the formed micro part in case of closed mould halves forming process. The temperature of the mould-insert was kept constant during the process. Shortly before the end of the forming process, while applying maximum pressure p_{imax} , the mould-insert temperature was reduced through rapid cooling to stabilize the formed part shape as well as to reduce its excessive shrinkage before ejection.

In comparison to conventional blow forming process design, the tool elements were heated with embedded heat cartridges to enable local heating. In accordance to investigations into thermoforming of micro polymeric bulk parts presented by [128], a suitable forming temperature is about 20 up to 30 °C above the glass transition temperature T_g of the formed polymeric material.

Due to the small mass of thin walled polymeric micro tubes, local heating was imperative to maintain stable thermal working condition in the mould-insert cavity and also avoid cold shock by insert at mould-insert/micro tube interface. Cold shock could cause local stiffening of the micro tube due to the thin wall and/or other instabilities associated with inhomogeneity in temperature distribution. In the micro blow moulding process localised heating was provided by the heated mould halves system as depicted in Figure 28. Localised heating ensured constant and uniform heat distribution for the forming process thereby preventing instability or imprecision in the process, which enabled better accuracy of the formed micro part. Local heating strategy required that the formed component be cooled down at the end of the process for better micro part dimensional quality. For the case that the formed part stayed longer time in the heated mould-insert with temperature not rapidly reduced to room temperature after the forming process, local overheating or carburisation of the formed micro part could occur. Rapid cooling (quenching) was applied to address local overheating at the end of

the forming process and stabilization of the formed part. The rapid cooling process was achieved by manual application of cooling-spray direct on the mould-system and the voltage reduction for the heating cartridge power supply from the operating voltage to 0 V.

Furthermore, the strategy for local heating of the micro tubes also addressed the challenge of the increase in ratio of the micro tube surface to its volume A/V reviewed. Micro tubes dissipate stored heat energy without heat source faster as macro tubes.

Forming Process Control

To investigate the process parameters required for the blow moulding of polymeric micro tubular parts, free forming process configuration illustrated in Figure 8 was implemented.

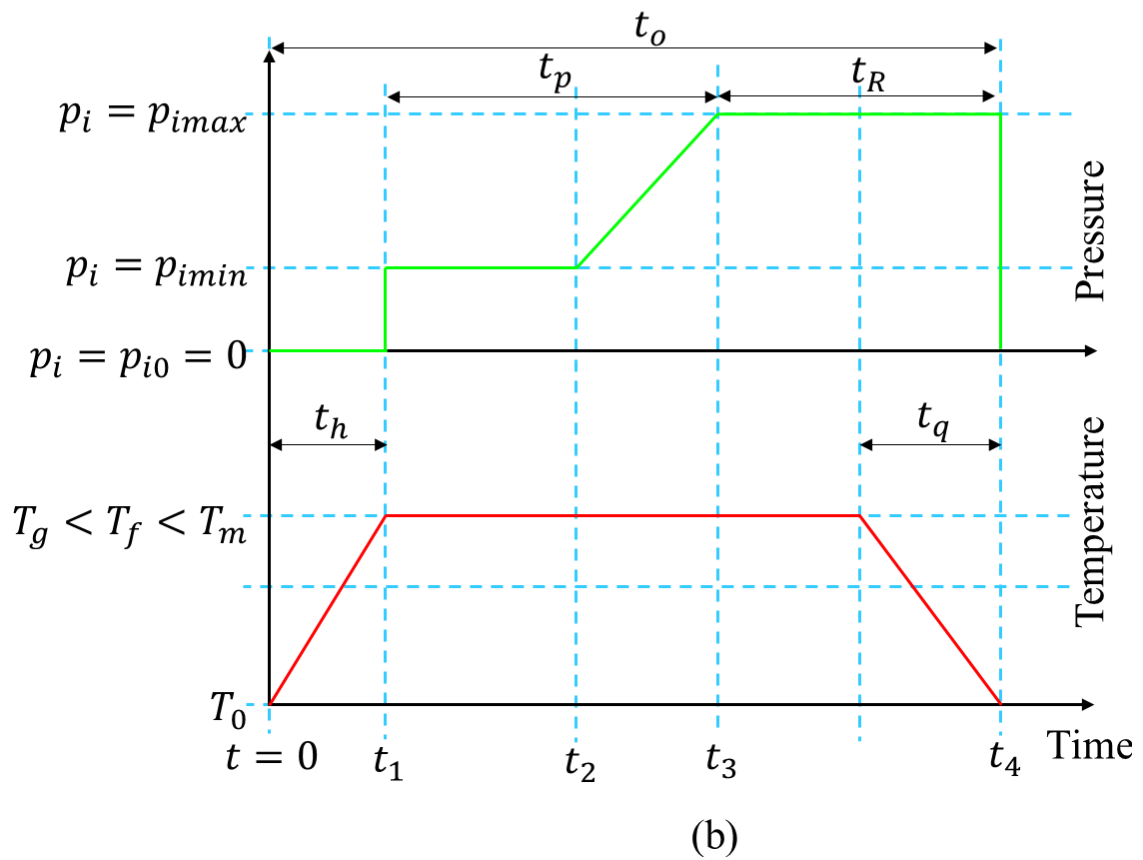
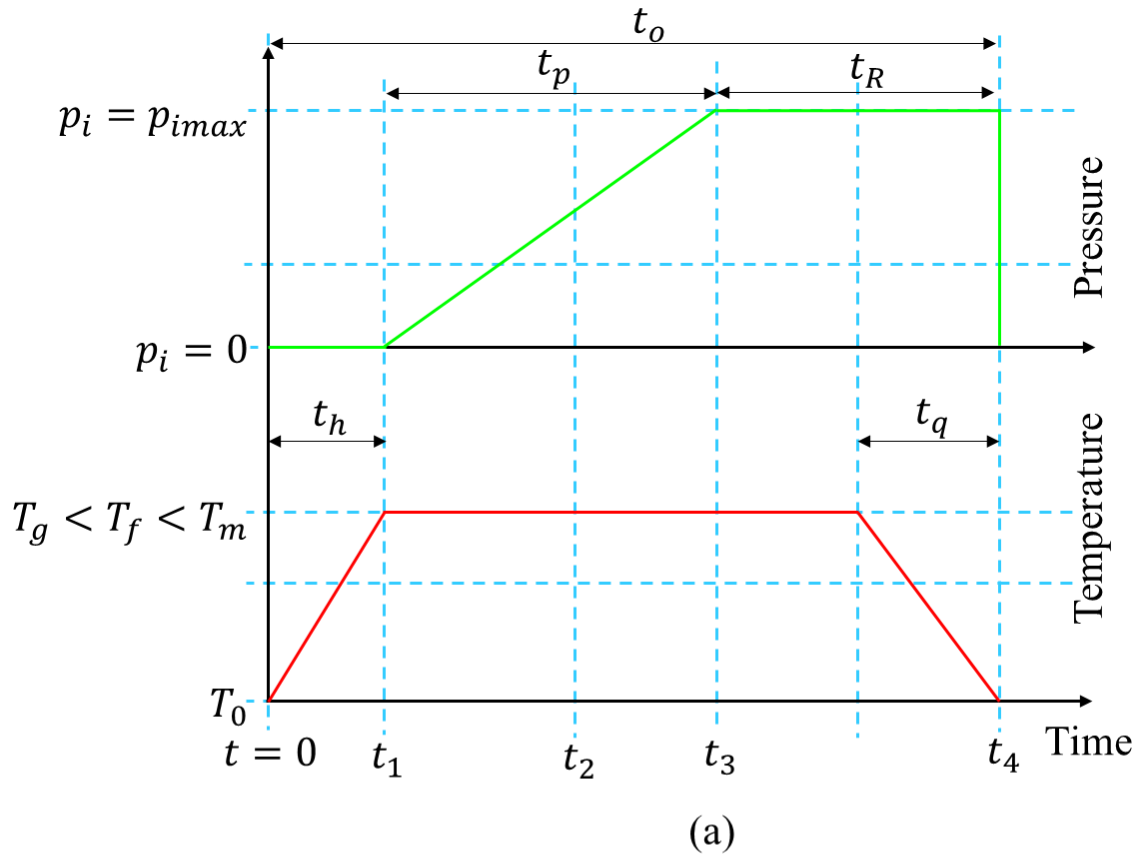


Figure 8 Process Control Configurations to form Polymeric Micro-Tubes: (a) Concept 1 and (b) Concept 2

The concepts in Figure 8 (a) and (b) illustrated that pressurization started in t_h , which is the heating time required to attain a working temperature T_f for the test polymeric micro tube. Boyce et al. in [129] suggested an ideal working temperature T_f of between 10 and 20 °C above the polymer material glass transition temperature T_g to process most polymeric materials. The reviewed T_g for PET listed in the material properties in Chapter 4 was defined at 60-84 °C. Also in Chapter 5, the glass transition temperature T_g for PET micro-tubes determined in the DMA experiments was in the range of 72.3 to 84 °C, which was independent of the micro-tube dimensions tested. Based on the DMA results and the calibration results of the micro IR-radiators presented in Chapter 6 the working temperature T_f for PET micro-tubes in this study was determined at 93 °C.

In Figure 8, p_{i0} , p_{imin} and p_{imax} represents internal pressure at different process stages. T_0 is the room temperature at the beginning of the blowing process, T_f represents the working temperature and T_g is the polymeric micro tube glass transition temperature. T_m is the melting temperature of the micro tube been tested. The time t_0 is defined as the total process time and made up of the following time segments: the heating time t_h , pressurization time t_p , relaxation time t_R and the quenching time t_q . The relaxation time t_R spanned the quenching time t_q . The quenching time represents the time from when the power supply to the IR-emitters are switched off and still pressurized up to the end of the process as defined in the control program. At the end of error-free or not error-free process as well as emergency shut-down, the process control provides that the internal pressure p_i as well as the working temperature T_f equals the initial values respectively. The initial internal pressure is defined as p_{i0} , which is equal to zero. The initial working temperature is the room temperature T_0 .

The different control profile achievable with the process control configuration in Figure 8 enabled the study of the strain rate $\dot{\epsilon}$ effects in the free-forming process of polymeric micro tubes. The strain rate $\dot{\epsilon}$ in this work is a function of internal pressure p_i , working temperature T_f , tensile force F_z , and micro tube material properties in the investigations conducted.

For a systematic study of the effects of strain rate, process configuration in Figure 8 was developed into a control program. The program algorithm was written in LabVIEW programming environment. Figure 9 shows the user interface of the customized software developed in the study.

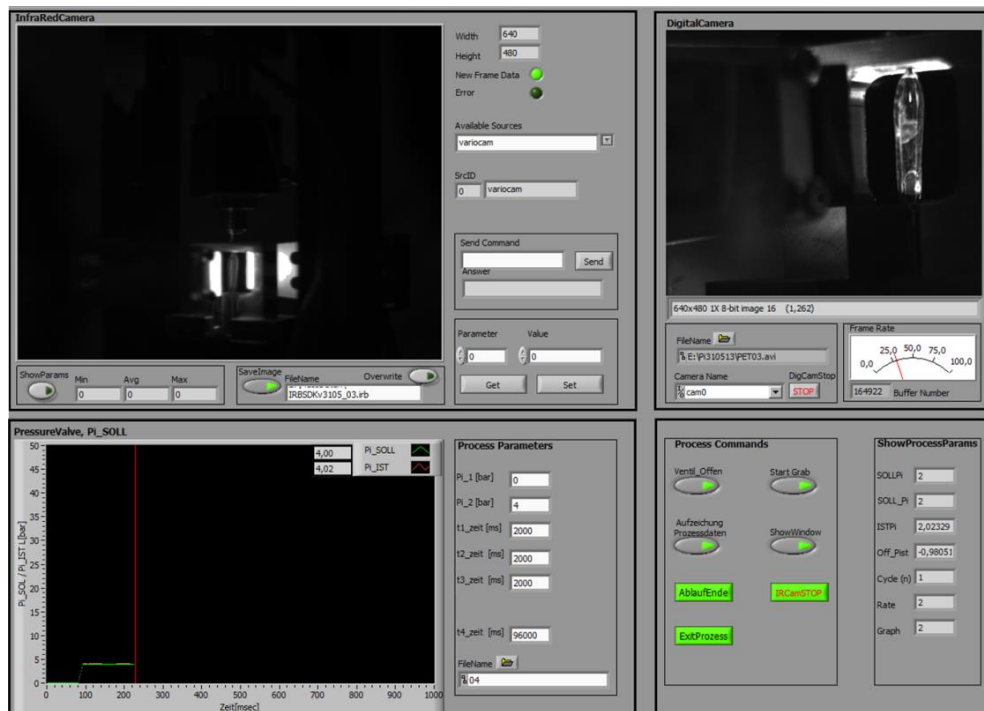


Figure 9 User Interface or Front Panel of the LabVIEW Software implementation of the Free-Blow Forming Configuration

An open-loop control concept was adopted in the process control design to systematically study the influence of the internal pressure p_i on the forming behaviour of the polymeric micro tubes at applied constant F_z and the working temperature T_f . The influence was controlled through a defined adjustable ratio p_{imax}/t_p .

Data acquisition and process control were achieved via appropriate hardware interface. The National Instruments (NI) multifunction data acquisition board (DAQ) model PCI-6221 with 37-Pins provided a cost effective solution to synchronize the multiple data sources and parameters due to the 37-pin D-Sub I/O connector feature. The DAQ model PCI-6221 is also characterized by the following:

- Two 16-bit analog outputs (833 kS/s)
- 10 digital I/O lines; 32-bit counters; digital triggering
- Correlated DIO (2 clocked lines, 1 MHz)
- NI-DAQmx driver software and NI LabVIEW Signal Express interactive data-logging software.

The DAQ model PCI-6221 was selected to achieve fast sampling rate with high accuracy in the process data acquisition. While digital trigger commands the Punch-Axial-Drive and Image Grabbing modules, waveform ± 10 V analog signal was provided to the piezo proportional pressure regulator valve in the Pressurization module to

precisely control the pressurization process. The modules are illustrated in Chapter 10 below. Real time data output of the process parameters were acquired via the FireWire (IEEE 1394) interface for the Image Grabbing module, while communication link with Pressurization and Punch-Axial-Drive modules was achieved through Peripheral Component Interconnect (PCI-Bus).

4. Theories of Polymer Forming

4.1 Introduction

Any material body deforms when it is subjected to external loads. The deformation is called elastic if it is reversible and time independent, that is, if the deformation vanishes instantaneously as soon as forces are removed. Brittle material such as glass, concrete, or rock under low hydrostatic pressure can only have elastic deformation before it fails under ultimate load. On the other hand, metals, polymers and rocks under high confining pressure can undergo substantial plastic deformation before failure and therefore are known as ductile materials [54].

At a microscopic level, deformation in polymers involves stretching and rotating of molecular bonds. Deformation mechanism in polymers can be distinguished as brittle, ductile with or without necking, and elastomeric. Factors such as strain rate and temperature affect the shape of the stress-strain curves much more significant than in ceramics and metals. This is due to viscoelastic behavior of polymers in which the stress-strain behavior is dependent on time. Temperature and strain rate have opposite effects. Increasing the strain rate or decreasing the temperature will lead to higher stress levels, but lower values of strain.

Most linear, and semi-crystalline polymers superficially similar to metals, can show the phenomena of yielding and necking [55].

The viscoelastic and viscoplastic responses of polymers have been given significant attention in the past decade [56-70]. This may be explained by the need to develop constitutive equations for polymeric materials applied to engineering problems as well as adequate description of the complex mechanical behavior of polymers not adequately predicted by conventional stress-strain relations. Hence a number of the investigations were focused on two major goals; one is the knowledge of the material properties at use condition, and the other is the knowledge of the material behavior at forming conditions.

Time dependent plastic deformation is usually denoted as viscoplasticity or creep. Plastic or irreversible deformation allows forming parts or semi-finished parts in manufacturing processes such as rolling, deep drawing, forging and blow forming [21].

Due to the focus in this work on the manufacture of polymeric components applying blow forming processes, large and inelastic polymer behaviors are here most significant. Hence, the following aspects of polymer behaviour such as viscoelasticity, viscoplastic, yield and plastic flow, and rubber elasticity are most favorable to this work.

4.2 Deformation Behaviour of Thermoplastic Polymers

Polymer behaviour at high temperatures could be comparable to ductile materials and generally, the response of a typical polymer is strongly dependent on temperature, strain history, and loading rate.

Polymers have various regimens of mechanical behavior, referred to as: glassy, viscoelastic, and rubbery. The various regimens can be identified for a particular polymer by applying a sinusoidal variation of shear stress to the solid and measuring the resulting shear strain amplitude. A typical result is illustrated in Figure 10 which depicts the apparent shear modulus as a function of temperature [71]. Shear modulus is defined as the ratio of the maximum amplitudes of stress and strain during a cycle.

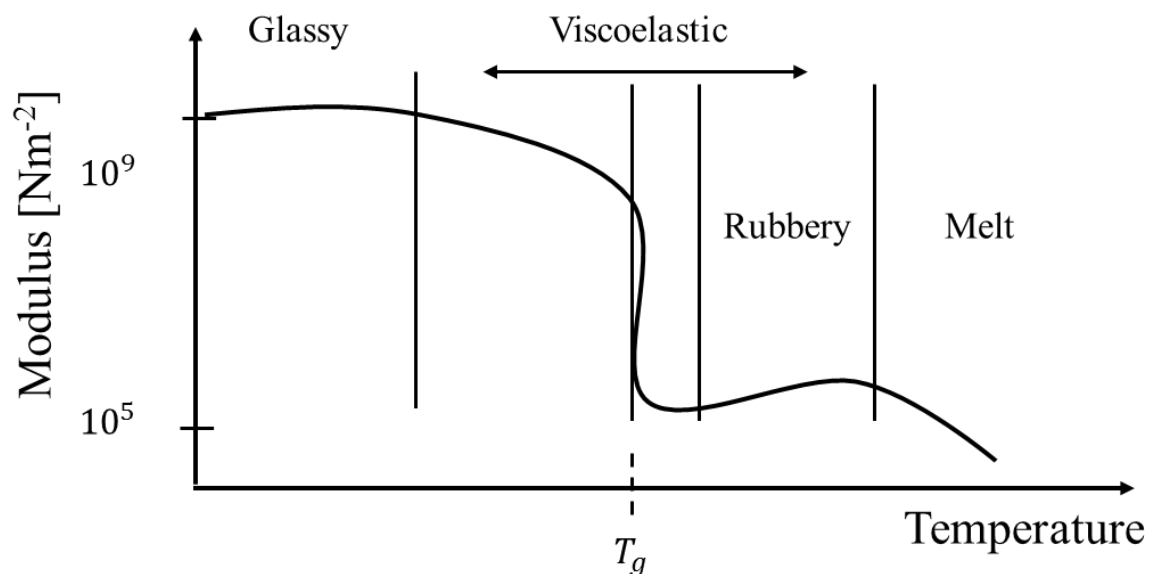


Figure 10 E-modulus versus Temperature for a model polymer. T_g is the glass transition temperature [13, 71]

At a temperature known as the glass transition temperature T_g , a polymeric material undergoes a dramatic change in mechanical response. Below this temperature, it behaves like a glass showing a stiff response. Near the glass transition temperature, the stress depends strongly on the strain rate. At the glass transition temperature, there is an abrupt drop in modulus. Above this temperature, there is a regime in which the polymer shows rubbery behavior: the response is elastic, the stress does not depend strongly on strain rate or strain history, and the modulus increases with temperature. Most polymers display these trends, however the regime maybe different for some polymers due to their molecular structures [13, 71].

In deformation analysis, rheological models are an effective tool for understanding and representing the mechanical properties of a material by combining simple elements such as springs and dashpots [14]. Figure 11 illustrates the general idea: in each case, the

force applied to the spring-damper system represents acting stress σ , whereas the extension represents shear strain ε [58].

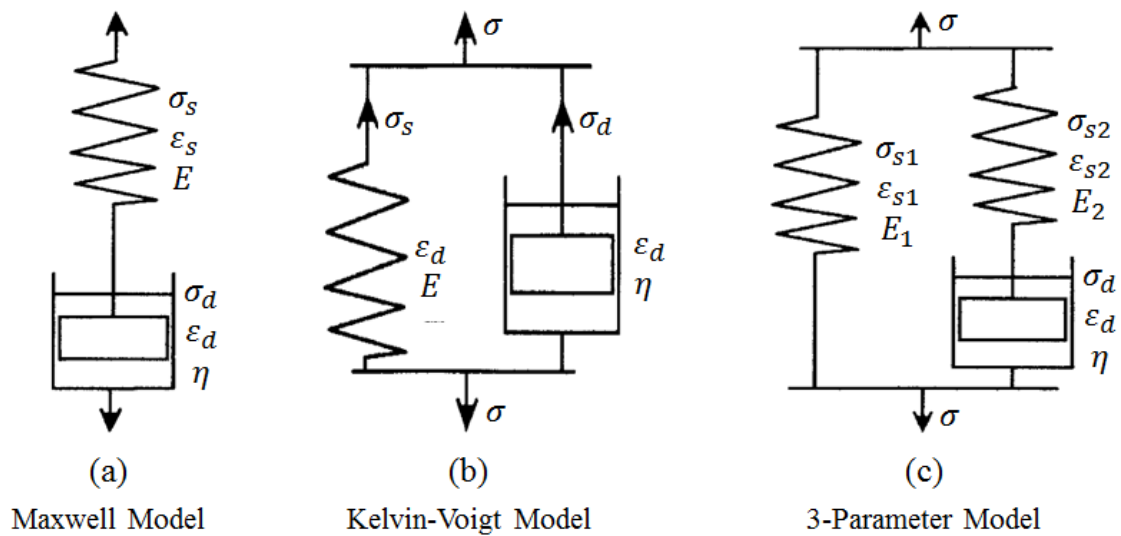


Figure 11 Spring-damper representations of polymer behaviour: (a) Maxwell model (b) Kelvin-Voigt model and (c) 3-Parameter linear solid model [15]

where E , E_1 and E_2 are E - modulus of spring, σ is applied stress, σ_s , σ_{s1} and σ_{s2} are stresses in the spring, σ_d represents stress in damper. ε_s , ε_{s1} and ε_{s2} are strains in the spring, ε_s , ε_{s1} and ε_d represents strains in damper and η is the damper viscosity.

Maxwell model depicted in Figure 11 (a) consists of a spring and damper in series and describes stress-relaxation in polymers. Under constant stress, the spring remains at constant length, but the damper is displaced at a constant rate and not useful to describe creep [15, 71 and 72].

The Kelvin-Voigt model in contrast consists of a spring and damper in parallel, as shown schematically in Figure 11 (b) and frequently used to describe creep in polymers. If a fixed stress is suddenly applied, the damper cannot be displaced instantaneously, so that the spring does not change in length and carries none of the stress [15, 71 and 72].

With an appropriate choice of E_1 and E_2 , the three-parameter model in Figure 11 (c) can describe both types of behavior [71]. The models described in Figure 8 are useful in developing mathematical relations between stress and strain in viscoelastic polymers and in giving insight to their response to creep, relaxation and other types of loading [72].

The stress-strain behavior of typical thermoplastic polymers such as PET at temperatures above the glass transition temperature is observed to exhibit four basic features depicted in Figure 12. The stress-strain curve exhibits a relatively stiff initial response corresponding to the initial slope h_e , and progress to flow σ_f , then a steady increase in the stress σ with strain ε . The hardening slope h_f depicted in Figure 12

controls the increase. The final stage is an abrupt increase in stress with strain at very large strains and referred to as a steep hardening region. Each of these features is found to depend on the actual strain, temperature, and strain state [58]. Large and inelastic stress-strain behavior above the polymeric glass temperature as shown in Figure 12 for polymers defines the manufacture of polymeric components in blow molding process.

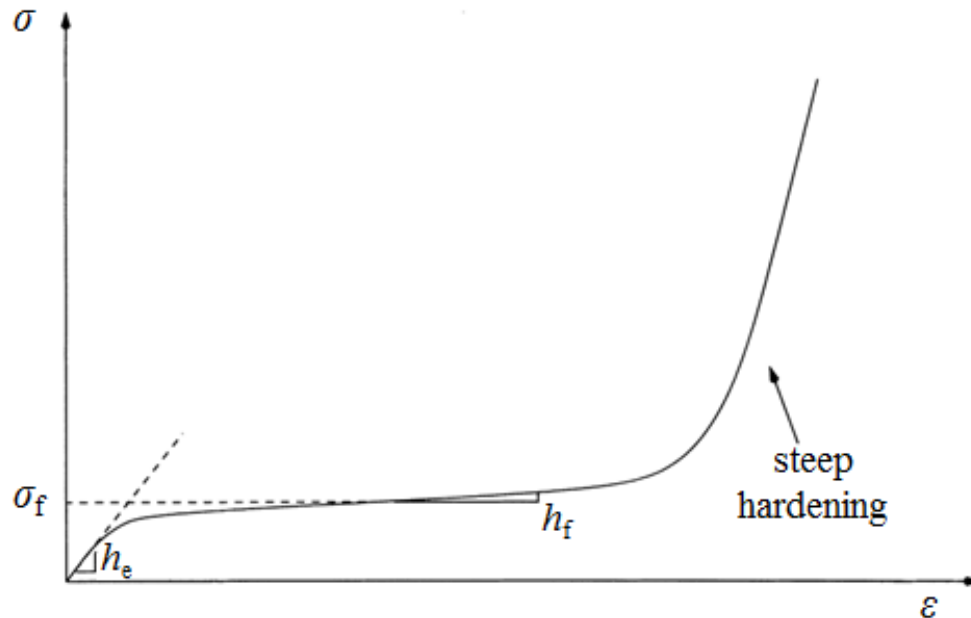


Figure 12 Basic features of the stress-strain behaviour of PET [58]

From the discussions on spring and dashpot models in Figure 11 (a) and (b) and the large strain behaviour of PET in Figure 12, modified spring-dashpot models are needed to better represent polymer behaviours applicable to larger deformations in the polymer processing as in blow forming process.

Many modified schematic-spring-damper-models to represent the stress-strain behavior of polymers have been proposed. Haward and Thackray in [73] provided the basic rheological constitutive theories for amorphous polymers [58, 74].

Tervoort et al. in [70] developed the compressible Leonov model, a three dimensional constitutive equation which combines the non-linear viscoelastic behavior of an Eyring dashpot with the strain hardening behaviour of a neo-Hookean spring. In [75] Govaert et al. extended this model by incorporating intrinsic strain softening, following the work of Hasan et al. [67]. The model is capable of describing the intrinsic deformation behavior, including rate and temperature dependent yield, strain softening and strain hardening, of glassy polymers like polystyrene, polycarbonate and polymethylmethacrylate under various loading conditions [56-70, 76].

Boyce et al. in [66] developed a three-dimensional material behavior model based on the macromolecular structure of polymers and the micro-mechanism of plastic flow which encompasses large, inelastic deformation behavior expected in the manufacture

of polymeric components. Such behavior is known to exhibit strain rate, temperature, and pressure dependent yield, as well as true strain softening and hardening after yield. In [58] Llane et al. improved on the model in [73] and interpreted the polymer behaviors as a response to overcome two basic resistances to deformation namely: an intermolecular barrier depicted in Figure 13, to deformation and was further augmented by the occurrence of strain-induced crystallization.

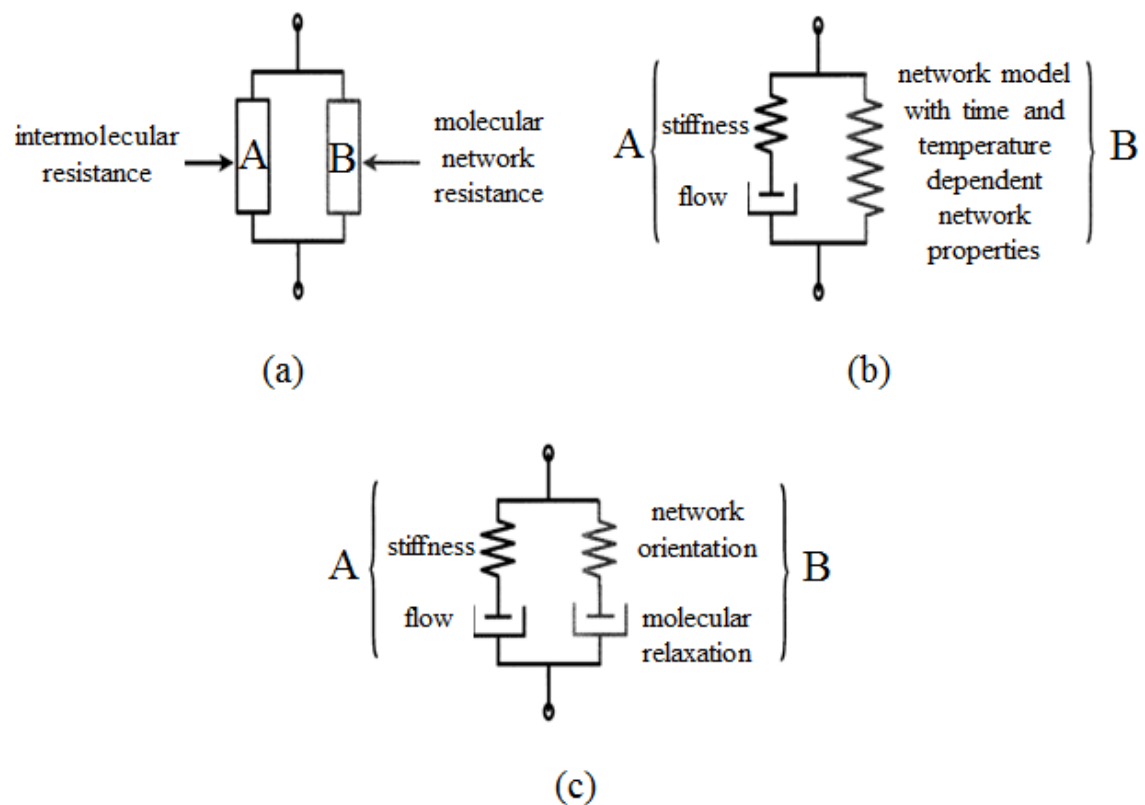


Figure 13 (a) Schematic representation of the breakdown of the total resistance into an intermolecular resistance occurring in parallel with a network resistance, (b) Elastic-viscoplastic representation of the intermolecular resistance acting in parallel with a time and temperature dependent network, and (c) The network resistance is modelled as a network orientation process and a molecular relaxation process acting together to accommodate deformation [58]

The evolving anisotropic resistance was attributed to molecular orientation. The first resistance results in the initially stiff response as well as the rate and temperature dependence of initial flow. This increase in resistance is assumed due to the strain-induced crystallization. The second resistance that produced the anisotropic strain hardening with stiffening effect behavior was taken to result from molecular alignment.

For the measurement of finite deformation, the second order deformation gradient tensor, \mathbf{F} is of particular importance [77] A key characteristic of finite deformation is the presence of rigid body motion. A consequence of this is that some arbitrary vector

within the continuum of a deforming body can be described either in terms of its position in space or relative to its initial material position. These are referred to as Eulerian and Lagrangian descriptions respectively. The deformation gradient describes the final spatial configuration of such a vector with respect to its initial material configuration as shown in Figure 14. The deformation gradient is evidently associated with strain in both Lagrangian and Eulerian space, hence its importance to continuum mechanics. [78].

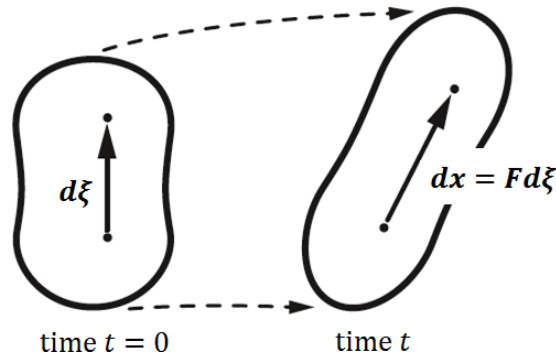


Figure 14 Deformation of a material line element with length $d\xi$ into a spatial line element with length dx [12]

$d\xi$ in Figure 14 is the vector between two adjacent points for the undeformed material at time t_i and This vector (coordinate system) remains fixed in space during the deformation and neither the size, orientation, or origin changes.

The second vector (coordinate system) is dx also depicted in Figure 14 moves and deforms together with the material and not orthogonal after the deformation.

The transformation from one system to the other can be done by a position-dependent matrix, the deformation gradient $F(\xi)$ for the vectors connecting two points: $d\xi$ and dx in the two coordinate systems and can be represented by Equation 7 [12, 77]:

$$dx_i = F_{ij}(\xi)d\xi_j \quad (7)$$

The position-dependence of the deformation gradient is given by Equation 8 [12, 77]:

$$F_{ij}(\xi) = \frac{\partial x_i(\xi, t)}{\partial \xi_j} \quad (8)$$

The constitutive model in [58] is based on the analog representation of the breakdown of the overall deformation resistance into an intermolecular resistance (resistance A) acting in parallel with a network resistance (resistance B) depicted in Fig. 10 (a). The

model first recognizes that the deformation gradient acting on each resistance is equal to the imposed deformation gradient, \mathbf{F} , which can be represented by Equation 9 [58]:

$$\mathbf{F}_A = \mathbf{F}_B = \mathbf{F} \quad (9)$$

The deformation of a sufficiently small volume element can be characterized by the deformation gradient and the Jacobian determinant \mathbf{J} as in Equation 10. According to Equation 9, \mathbf{J} is same for both parts of the model as represented in Equation 10 [79]:

$$\mathbf{J}_A = \mathbf{J}_B = \mathbf{J} = \det \mathbf{F} \quad (10)$$

The deformation must satisfy $\mathbf{J} = 1$ to prevent volume change [79].

The deformation gradient \mathbf{F} contains not only information about the deformation, but also about rigid body rotations of the material. These, however, do not contribute to the deformation itself, and the two contributions thus have to be separated. This can be done by considering the deformation gradient as a composition of a deformation \mathbf{U} , called the right stretch tensor or sometimes, material stretch tensor and a subsequent rotation \mathbf{R} . These two are multiplied using the tensor product and given in Equation 11 [12, 77]:

$$\mathbf{F} = \mathbf{R}\mathbf{U} \quad (11)$$

The right stretch tensor \mathbf{U} expresses stretch and the eigenvalues of the stretch tensor are called the principal stretches $\lambda_i, i = 1, 2, 3$. The principal stretches in \mathbf{U} represent the ratio between the deformed length l_i and the undeformed length l_0 of a material line element in the principal directions of \mathbf{U} , $\lambda_i = l_i/l_0$. The right stretch tensor \mathbf{U} can be derived from \mathbf{F} according to Equation 12 [80]:

$$\mathbf{U}^2 = \mathbf{F}^T \mathbf{F} \quad (12)$$

Although the deformation is described by \mathbf{U} , other measures of strain such as The Cauchy-Green strain tensor \mathbf{C} can be useful. The Cauchy-Green strain tensor \mathbf{C} is defined in Equation 13 [182]:

$$\mathbf{C} = \frac{1}{2}(\mathbf{U}^2 - \mathbf{1}) = \frac{1}{2}(\lambda_i^2 - 1) = \frac{1}{2}(\mathbf{F}^T \mathbf{F} - \mathbf{1}) \quad (13)$$

where λ_i is the stretch vector.

Cauchy-Green strain tensor vanishes in an undeformed system: $\mathbf{C} = 0$. For small deformations, it converges to the strain tensor ε . However any deformation, large or small, homogeneous or non-uniform, can be characterized by Cauchy-Green strain tensor. Since Part A and B are connected in parallel in Figure 10, the Cauchy stress tensor for the material using the models is obtained by addition of the σ_{ij} in Parts A and B as in Equation 14, [79]:

$$\sigma_{ij} = \sigma_{ijA} + \sigma_{ijB} \quad (14)$$

Cauchy stress σ_{ij} which is the actual load (force) per unit area acting on an actual deformed solid, quantifies (physical measure) the internal force. Other definitions of stress often appear in constitutive equations. The stress at a point in the solid depends only on the change in shape of an infinitesimal volume element surrounding the point. It must therefore be a function of the deformation gradient or a strain measure that is derived from it [71].

4.3 Yield Criteria

Main assumptions in classical plasticity theory to simplify analyses of yield behaviour of solids include: that the material is isotropic and homogeneous; yielding is not influenced by the hydrostatic component of the stress state; tensile and compressive yield strengths are equal; and deformation proceeds under constant volume. Although these assumptions are reasonable where ductile metals are involved, their accuracy diminishes when polymers are the solids under consideration [12, 81 and 82].

One of the problems in adopting a simple approach of this nature is that the whole stress-strain curve is in general different for different stress fields. In the case of tensile tests, a neck is usually formed and the yield point defined as the stress at maximum observed load. In compression tests however, a load drop is often not observed and the yield point is then defined as the point of intersection of two tangent lines on the load-elongation curve depicted in Figure 15 [81].

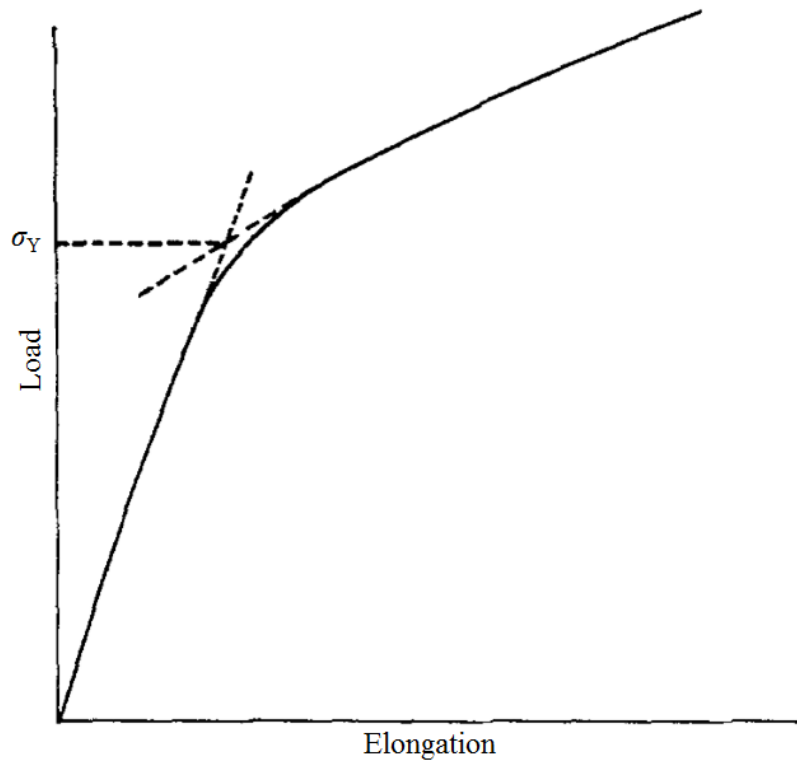


Figure 15 Definition of the yield point as the point of intersection of two tangent lines on the load-elongation curve. σ_Y is the yield stress of a thermoplastic polymer [81]

Present interest in the yield behavior started with the recognized in classical concepts of plasticity on the relevance in forming [20]. Yield criteria such as Tresca and von Mises referred to as failure theories in some literatures, are within the last decade been expanded to test their applicability in the yield behaviour of various polymers [82].

Polymers in general show all different types of behavior depending on the exact conditions of test, quite irrespective of their chemical nature and physical structure. Thus explanations of yield behavior which involve, for example, cleavage of crystallites or lamellar slip or amorphous mobility are only relevant to specific cases. As in the case of linear viscoelastic behavior or rubber elasticity an understanding of the relevant phenomenological features is helpful to decide on suitable measurable quantities and then provide a molecular interpretation of the subsequent constitutive relations [20]. The most general form of a yield criterion in Equation 15 is a postulated mathematical expression of the states of stress that will cause yielding [54]:

$$F(\sigma_1, \sigma_2, \sigma_3, \tau_{23}, \tau_{31}, \tau_{13}) = Y \quad (15)$$

For isotropic materials, since the principal stresses describe the stress state σ_{ij} completely, excepting only its orientation, Equation 15 can be rewritten as in Equation 16 using principal stresses to define the yield [54]:

$$F(\sigma_1, \sigma_2, \sigma_3) = Y \quad (16)$$

The Tresca criterion postulates that yielding depends on the largest shear stress in the body. With the convention $\sigma_1 \geq \sigma_2 \geq \sigma_3$ that can then be expressed as $\sigma_1 - \sigma_3 = Y$. The constant Y can be found by considering a tension test. In this case $\sigma_3 = 0$ and $\sigma_1 = \sigma_{YT}$, which is the yield strength at yielding, hence $\sigma_1 = \sigma_{YT}$ [65, 69]. The determination of plastic flow of multiaxial stress state in a material requires a yield criterion [81].

To be completely general, a yield criterion has to be valid for any stress state [55]. There are many different yield criteria; here the simplest ones are discussed for illustration. Let σ_{ij} be the stresses acting on a solid and let σ_1, σ_2 and σ_3 denote the principal values of stress. In addition, let σ_{YT} denote the yield stress of the material in uniaxial tension as defined above, then for Von Mises yield criterion [54]:

$$f(\sigma_{ij}, \bar{\epsilon}^p) = \sqrt{\frac{1}{2}[(\sigma_1 - \sigma_2)^2 + (\sigma_1 - \sigma_3)^2 + (\sigma_2 - \sigma_3)^2]} - \sigma_{YT}(\bar{\epsilon}^p) = 0 \quad (17)$$

$\bar{\epsilon}^p$ is equivalent plastic strain. Yield criteria are generally defined so that the material deforms elastically for:

$$f(\sigma_{ij}) < 0 \quad (18)$$

and plastically for:

$$f(\sigma_{ij}) = 0 \quad (19)$$

The main function of yield criteria is to predict onset of plastic deformation in a complex state of stress when the flow stress under uniaxial tension of the material is known [55]. It is useful to define an effective stress, $\bar{\sigma}$ for a yield criterion such that yielding occurs when the magnitude of $\bar{\sigma}$ reaches a critical value *as* Y in Equations 15 and 16 or yield surface as in Figure 16. From Equation 19 the von Mises criterion becomes [70]:

$$\bar{\sigma} = \sqrt{\frac{1}{2}[(\sigma_1 - \sigma_2)^2 + (\sigma_1 - \sigma_3)^2 + (\sigma_2 - \sigma_3)^2]} \quad (20)$$

For plane stress depicted in Figure 16, the effective stress, $\bar{\sigma}$ can be derived for Von Mises criteria from Equation 21 with $\sigma_3 = 0$ to give:

$$\bar{\sigma} = \sqrt{\sigma_1^2 + \sigma_2^2 - \sigma_1\sigma_2} \quad (21)$$

The effective stress, $\bar{\sigma}$ for Tresca criteria in plane stress shown also in Figure 16 is given by Equation 22 [55]:

$$\bar{\sigma} = \sigma_1 - \sigma_2 \quad (22)$$

Von Mises yield criteria is represented by the solid ellipse line, while Tresca yield criteria is the inscribed dotted regular hexagon in Figure 16 (a) and (b). Since $\sigma_3 = 0$ was assumed for Figure 16 and Equations 21 and 22, the convention that $\sigma_1 \geq \sigma_2 \geq \sigma_3$ cannot be obeyed for $\sigma_2 < 0$ [55].

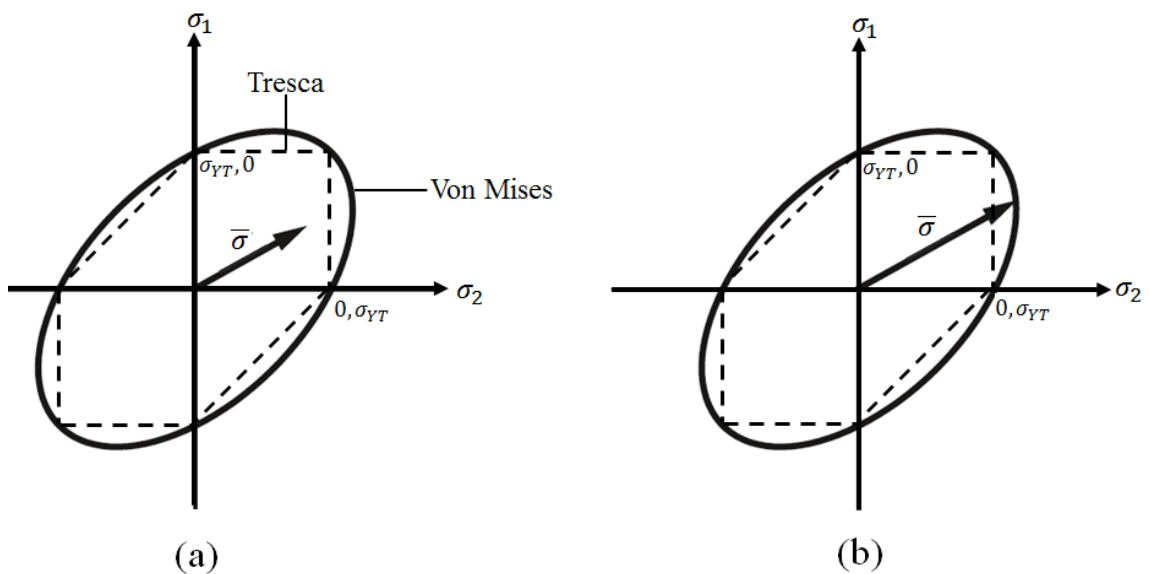


Figure 16 Yield surface for a state of plane stress. If the stress state reaches the yield surface, yielding occurs

If the state of stress $\bar{\sigma}$ falls within the cylinder shown in Figure 16 (a), the material is below yield and responds elastically. However, when the state of stress $\bar{\sigma}$ lies on the surface of the cylinder depicted in Figure 16 (b), the material yields and deforms plastically. If the plastic deformation causes the material to strain harden, the radius of the ellipse increases. The stress state cannot lie outside the yield surface; this would lead to an infinite plastic strain [12].

In Figure 16, the Tresca criterion is obviously more conservative than von Mises criterion. The criterion would predict plastic flow for the stress state $\bar{\sigma}$ before von Mises [55]. However at points 0, σ_{YT} and σ_{YT} , 0 in Figure 16, plastic flow for the stress state $\bar{\sigma}$ prediction is equal for both criteria. The precise form of the yield criteria depends however on the material considered [12].

In contrast to metals, the yield strength of polymers is different in compression and tension. Frequently, the yield strength in uniaxial compression is 20 % to 30 % larger than in uniaxial tension. To account for this, the von Mises yield criterion is augmented by terms that depend on the hydrostatic stress state [12].

There have been a number of detailed investigations of the influence of hydrostatic pressure on the yield behavior of polymers [20], due to the relationship between a yield criterion, which depends on hydrostatic pressure, and the Mohr-Coulomb yield criterion. Rabinowitz, Ward and Parry [83] determined the torsional stress-strain behaviour of isotropic PMMA under hydrostatic pressures up to 700 MPa as shown in Figure 17.

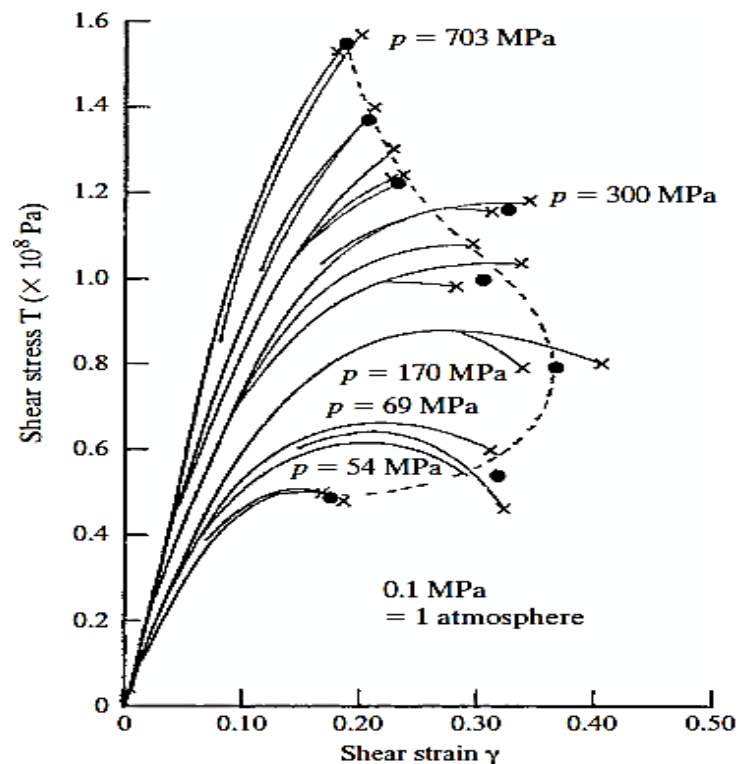


Figure 17 Shear stress versus strain curves for PMMA showing fracture envelope. The “x,, represents fracture points and black - spots “•,, show yield points [83]

The dotted curve in Figure 17 represents the envelope of the fracture points and illustrates how the strain to fracture at first increases with increase of pressure and then decreases. The yield-point is defined as the point of maximum stress on a stress-strain curve which subsequently shows a region of falling stress. The failure of samples

characterized in this way was regarded as ductile. The fracture stress is the stress at failure irrespective of whether the stress-strain curve shows a maximum. If no maximum is observed the sample was thus regarded as brittle [83].

According to Figure 17, it may be assumed that the hydrostatic component of stress affects the shear stress required to instigate yield and in the range of pressure from one atmosphere to 3.2 kbar the stress-strain curve showed a drop in true stress prior to fracture. The maximum stress was taken as the yield stress and varies linearly with hydrostatic stress [83]. The shear modulus at small strains which is given by the initial slope of the stress versus strain curves, also increases with pressure [84].

The results in Figure 17 for PMMA were represented by the linear expression in Equation 23 [83]:

$$\tau = \tau_0 + \mu p \quad (23)$$

where τ is the shear yield stress at pressure p and τ_0 is the shear yield stress at atmospheric pressure [83, 84]. Equation 23 states that the shear yield stress τ increases linearly with the hydrostatic pressure, p and defined the Mohr-Coulomb yield criterion. Most amorphous glassy polymers have been found to obey Equation 23. The dimensionless constant of proportionality μ , is referred to as the coefficient of internal friction following the usage in soil mechanics and represents the increase of shear yield stress with hydrostatic pressure. Depending on polymer the value μ is between about 0.1 and 0.25 [84]. Values of μ for crystalline polymers tend however to lower value [83, 84].

Pressure dependent yield criterion will be more satisfactory than the Mohr-Coulomb criterion when a representation is developed that includes the effects of temperature and strain rate on the yield behavior [20]. In physical terms, the hydrostatic pressure can be seen as changing the state of the polymer by compressing the polymer significantly, unlike the situation in metals where the bulk moduli are much larger about 100 GPa compared with about 5 GPa for polymers. Although the experimental evidence that exists is not unequivocal in this respect, however flow rules for the polymer subjected to hydrostatic pressure maintains that pressure has the sole effect of increasing the magnitude of the yield stresses. Recent studies of yield behavior, using a variety of multiaxial stressing experiments, can be described adequately by a generalization of Equation 23, which represents modified von Mises yield criteria [20].

Polymers are much more resistant to yielding in compressive stress states than in tension. The atomistic motions underlying slip in polymers can be viewed as requiring free volume as the molecular segments move and this free volume is diminished by compressive stresses. It is thus difficult to form solid polymers by deformation processing such as stamping and forging in the same way steel can be shaped [85].

Figure 18 depicts a pressure dependent yielding in which the yield envelop translates with respect to the conventional von Mises (no hydrostatic stress) [55].

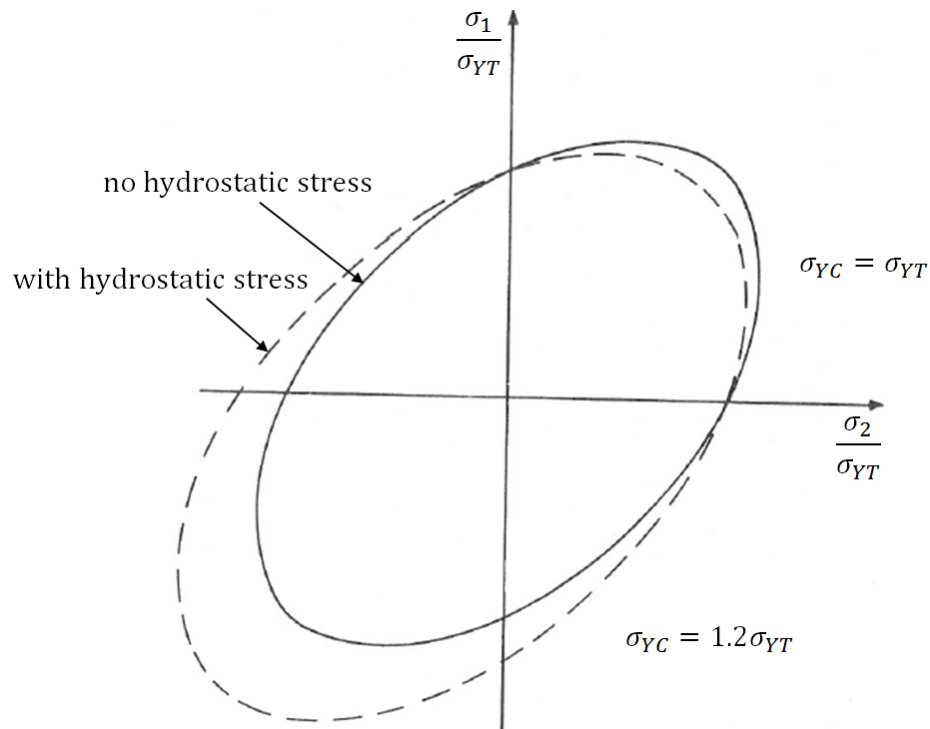


Figure 18 Von Mises yield criterion including a hydrostatic stress term: σ_{YT} tensile stress at yield and σ_{YC} compressive stress at yield

The version of modified von Mises criterion in Figure 18 accommodates the differences in tensile and compressive yield strengths and accounts for any dependence of yielding on the hydrostatic component of the applied stress state. The model can be represented for a biaxial loading by Equation 24 [82]:

$$\sigma_1^2 + \sigma_2^2 + \sigma_1\sigma_2 + (\sigma_{YC} - \sigma_{YT})(\sigma_1 + \sigma_2) = \sigma_{YC}\sigma_{YT} \quad (24)$$

The model in Equation 24 considered the actual macroscopic behaviour of polymers compared with the pressure-modified shear stress in Equation 24 [82]. The effect of this modification is to slide the von Mises ellipse to extend less into the first quadrant and more into the third quadrant as shown in Figure 18. This shows graphically that greater stresses are needed for yield in compression, and lesser stresses in tension [85].

Plastic or flow yield is generally defined as a permanent molecular rearrangement that begins at a sufficiently high state of stress. The yielding process is very material-dependent, being related directly to molecular mobility. Yield leads to a change in the shape of the sample as a whole. Other processes such as crazing also called strain whitening may as well take place when a polymer is deformed but these involve only

local deformations and are not necessary part of the general yield process. They are often the prelude to fracture [84].

Based on different processes at the molecular scale, thermoplastics show two distinct forms of inelastic deformation mechanisms under tensile loads in terms of shear band formation and craze formation, respectively. Shear bands lead to inhomogeneous orientations under an angle of about 45° with respect to the tensile direction without change in density [12, 14]. Crazing involves the formation of micro-voids and stretched chains or fibrils, which leads to density inhomogeneities and to volume change [22]. Development of Crazing is valid for forming in the range of the glass transition temperature [12]. In tensile loading as in uniaxial tension, long elongated voids are created within the material. The fibril formation depends on shear flow and free volume. A yield criterion that takes hydrostatic component $\sigma_1 + \sigma_2$ into account through craze formulation is given in Equation 25 [55, 85]:

$$\sigma_1 - \sigma_2 = a + \frac{b}{\sigma_1 + \sigma_2} \quad (25)$$

where $\sigma_1 - \sigma_2$ represents the shear, $\sigma_1 + \sigma_2$ represents the hydrostatic component, and a and b are material parameters that depend on temperature. Figure 19 illustrates the resulting combination of two separate surfaces projected on a two dimensional stress plane [22].

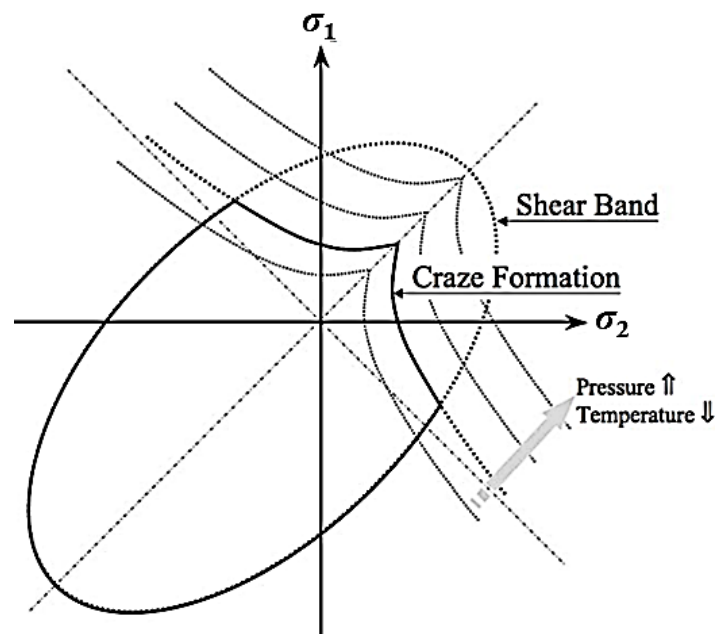


Figure 19 Schematic yield loci in thermoplastics resulting from shear band and craze formation [22]

The constants a and b in Equation 25 can be chosen to fit the curve of Figure 19 to the experimental data.

The yield loci for thermoplastics in Figure 19 resulted from shear band and craze formation. The yield locus representing craze formation is found to shift towards the first quadrant for increasing pressure and decreasing temperature, respectively [13].

Also in the Figure, in the first (tensile) quadrant of stress space, the normal stress yielding (crazing) envelop is everywhere inside the shear envelop. This implies that all combinations of tensile biaxial stress produce crazes prior to shear yielding. However, in the second and fourth quadrants different behavior is observed, due to the significant increase in stress required to propagate a craze as the pure shear condition is approached. This effect is to be expected since pure shear is a non-dilatational stress field [86]. Thus, at a particular combination of stresses, the two envelops intersect each other. It can be argued that the intersection points in the second and fourth quadrants represent a stress field induced brittle to ductile transition. This stress field can be shown to be a simple tension plus a hydrostatic pressure described by Equation 25 [87].

4.4 Plastic Forming

Yield criteria can be used to assert for any stress state whether a material yields. How the material deforms plastically is not governed by a yield criterion. The plastic deformation itself is described using flow rules [12].

According to Hill [88], the early work known as the Lévy-Mises Equation specifies the increment of total strain as in Equation 26:

$$d\varepsilon_{ij} = d\lambda\sigma'_{ij} \quad (26)$$

where $d\lambda$ is a scalar factor of proportionality and σ'_{ij} is the gradient of the yield surface and therefore normal to the yield surface. This Equation was later extended to allow for the elastic strain to give the Prandtl-Reuss in Equation 27 [89]:

$$d\varepsilon_{ij} = d\varepsilon_{ij}^e + d\varepsilon_{ij}^p \quad (27)$$

Also in the flow theory it is customary to decompose the stress tensor into two parts as in Equation 28:

$$\sigma_{ij} = p\delta_{ij} + S_{ij} \quad (28)$$

where σ_{ij} in Equation 28 is the true stress, δ_{ij} is the Kronecker's delta and S_{ij} is the true stress deviator, which is equal to the gradient of the yield surface [71] in Equation 26. The p in Equation 28 represents the hydrostatic stress or pressure given by Equation 29:

$$p = \frac{1}{3}(\sigma_1 + \sigma_2 + \sigma_3) \quad (29)$$

In Equation 29, $p\delta_{ij}$ is called the spherical or hydrostatic stress tensor [71].

The deformational response of solid polymers to applied stress and the temperature dependence of the stress-strain behavior have been extensively investigated for many varieties and types of polymers. Only in recent years, however, has attention been devoted to the pressure dependence of the mechanical properties of polymers, despite the obvious technological importance of the pressure variable in polymer processing and despite numerous literature references to the effects of pressure on other materials, such as metals and ceramics [90-92].

The yield or flow stress σ_f of both crystalline and amorphous polymers increases significantly with increase of hydrostatic pressure [90, 84] and, to a first approximation, in a linear manner. To account for the observed data, yield criteria for polymers must include in their formulation the hydrostatic component of stress. The pressure dependence of the flow stress is significant for the low-modulus polymers [90]. For metallic materials experimental evidence enabled the assumption that the hydrostatic pressure has no effect on plastic yielding. The plastic yielding is only related to the deviatoric stress tensor [54, 71].

According to Equation 27, the total strain increment $d\varepsilon$ is the sum of the elastic $d\varepsilon_{ij}^e$ and the plastic $d\varepsilon_{ij}^p$ increments. If the yield function is the Von Mises yield function, then the plastic strain increment may be written as Equation 30 [89]:

$$d\varepsilon_{ij}^p = d\lambda \sigma'_{ij} \quad (30)$$

It is also important to note that the plastic strains in a solid depend on the load history. This means that the stress-strain laws are not just simple equations relating stress to strain. Instead, plastic strain laws must either relate the strain rate in the solid to the stress and stress rate or else specify the relationship between a small increment of plastic strain $d\varepsilon_{ij}^p$ in terms of strain, stress, and stress increment $d\sigma_{ij}$. In addition, plasticity problems are almost always solved using the Finite element method. Consequently, numerical methods are used to integrate the plastic stress-strain equations [71].

Equation 30 can be written in rate form as in Equation 31 [89]:

$$d\dot{\epsilon}_{ij}^P = d\dot{\lambda}\sigma'_{ij} \quad (31)$$

Equation 31 is called the plasticity equation and $d\dot{\epsilon}_{ij}^P$ is the increment of plastic strain tensor where $d\dot{\lambda}$ is a positive scalar and characterized by plastic flow, temperature, material, strain and strain rate [89]. Plastic strains are volume preserving requiring the plastic strain rate to satisfy $\dot{\epsilon}_{ii}^P = 0$ [89].

Flow behavior of materials could be classified for two different applications namely: rate independent flow used to model deformation at low temperatures and rate dependent flow or viscoplasticity applied to models at high temperatures. There are also various different models within these two broad categories. The models generally differ in two respects namely: the yield criterion, and the strain hardening law. There is no completely general model that describes all the features that were listed above, so in any application, one will need to decide which aspect of material behavior is most important and then choose a model that accurately characterizes this behavior [71].

The five key concepts that form the basis of almost all classical theories of plastic flow in metals, polymers and other materials are as follows: The decomposition of strain into elastic and plastic parts; Yield criteria, which predict whether the solid responds elastically or plastically; Strain hardening rules, which control the way in which resistance to plastic flow increases with plastic straining. Flow rules are used to determine the stresses from a given strain rate. They do not allow calculating how the yield surface changes by hardening, which is performed by hardening laws [12, 73].

4.5 Hardening Laws

Many solid materials such as metals and polymers harden, when deform plastically. Once the criterion for plastic flow is achieved, the stress required to cause further plastic deformation increases. This stress is often a function of accumulated plastic strain, which can be deduced as integral of Equation 31 along the strain path. The integrated strain, known as the total equivalent plastic strain $\bar{\epsilon}^p$, provides a suitable measure of the plastic deformation [80].

During the plastic deformation the subsequent yield surface will expand, translate, and distort in the stress space. For some materials such as rock, concrete, and soil the stress-strain curve is lower in the plastic region, a phenomenon called strain softening. The subsequent yield surface for those materials contracts in size due to the softening phenomenon [54]. Strain hardening in polymers occur mostly at large strains and the polymer material intrinsic behaviour influences significantly the strain softening instability during large deformations in polymers [56, 58 and 84].

The following three important cases of hardening are discussed [12]:

- No hardening
- Isotropic hardening
- Kinematic hardening.

No hardening

A perfectly plastic material does not harden and the yield surface defined in Equation 32 remains unchanged during deformation. Hence, the yield criterion for no hardening is given by [12]:

$$g(\sigma_{ij}) = f(\sigma_{ij}) = 0 \quad (32)$$

g describes the modified yield surface in the current flow stress during subsequent plastic deformation and hardening. The current flow stress refers to the stress state at the material yield strength [12]. The corresponding material behaviour is illustrated in Figure 20.

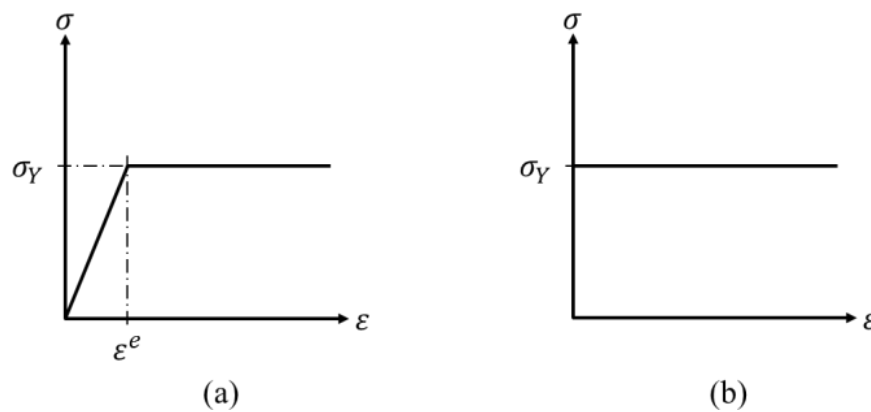


Figure 20 Illustration of No hardening in a tensile test: (a) Perfectly plastic and elastic
(b) Rigid perfectly plastic

In reality, there are no perfectly plastic materials and either strain hardening as in metals or strain softening in geological, or soil materials as well as combinations of both forms can be observed in thermoplastic polymers [12, 22]. In a tensile test, most materials start to neck immediately upon yielding because the stability criterion would be violated. If plastic deformations are large such as deep drawing and forging in metal or blow forming in polymers processes, the elastic part can be neglected and the stress-strain relationship expressed with Ludwik give in Equation 33 [89]:

$$\sigma = k_0 \epsilon^n \quad (33)$$

where k_0 is a strength coefficient and n is a strain hardening exponent usually lying between 0 and 0.5 [89].

If $n = 0$ in Equation 33, there is no hardening and the flow stress is constant at a value $\sigma = k_0$. This is called perfectly plastic behaviour illustrated in Figure 20 (b). However, with increasing hardening exponent, the hardening increases as is the case in most materials. Elastic deformations can be included in material behaviour law to describe elastic-perfectly plastic depicted in Figure 20 (a) [12].

Most polymers show weak strain hardening features at low stretch ratios, which could explain the reason polymers are characterized by necking in contrast to metals. This behaviour is related to the fact that the strain hardening of polymers is provided by the orientation of molecules against the increased concentration of dislocations in metals [87].

4.5.1 Isotropic Hardening

During isotropic hardening, the yield surface increases symmetrically around the origin as depicted in Figure 21 (a). If yielding of the material is governed by the von Mises yield criterion, the yield function for isotropic hardening is expressed as in Equation 34 [12]:

$$g(\sigma_{ij}, \bar{\varepsilon}^p) = f(\sigma_{ij}, \bar{\varepsilon}^p) = \sigma_Y(\bar{\varepsilon}^p) \quad (34)$$

Figure 21 (a) shows the plane stress development of the yield surface according to Equation 34 during isotropic hardening, while Figure 21 (b) depicts schematically the tension-compression curve with reversal stress and strain.

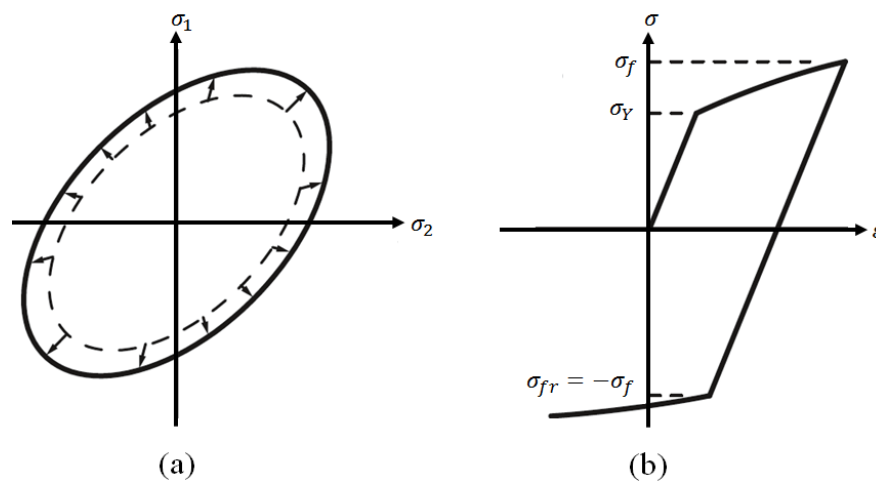


Figure 21 Isotropic hardening: (a) Evolution of the yield surface (b) Stress versus strain curve with reversed load for an isotropically hardening material [12]

When hardening begins, the flow stress in tension σ_f is equal to the yield strength σ_Y as illustrated in Figure 21 (b). The yield strength σ_Y defines the initial yield condition and represents the radius of the yield surface. When σ_Y increases, the yield surface expands in size as in Figure 21 (a) and can be a function of either one of the two quantities that are used to measure the degree of hardening: the plastic work per unit volume or the equivalent plastic strain with increment.

Figure 21 (b) represents the stress-strain diagram of a material with isotropic hardening. The material was initially deformed in a uniaxial tensile test and then subjected to uniaxial compression test, from the Figure: $\sigma_{fr} = -\sigma_f$ and $|\sigma_{fr}| = \sigma_f$ [93].

The yield stress in subsequent yielding during hardening depends on the plastic part of deformation. Several mathematical expressions in terms of plastic strain ε^p for subsequent yielding expressions have been developed namely: Ludwik in Equation 33, Swift and Voce [93]. The expression from Voce in Equation 35 gives a good fit of experimental stress-strain curves [93]:

$$\sigma_f(\bar{\varepsilon}^p) = \sigma_Y + k_0[1 - \exp(-n\varepsilon^p)] \quad (35)$$

k_0 and n are the material constants, which can be determined by fitting the above equations with the experimental curves of true stress as function of the plastic part of logarithmic strain [93].

4.5.2 Kinematic Hardening

In kinematic hardening the yield surface translates in the stress space while the shape and size of the yield surface remain constant. The yield function to describe the yield surface must then depend on the location of the surface in stress space as depicted in Figure 22 (a).

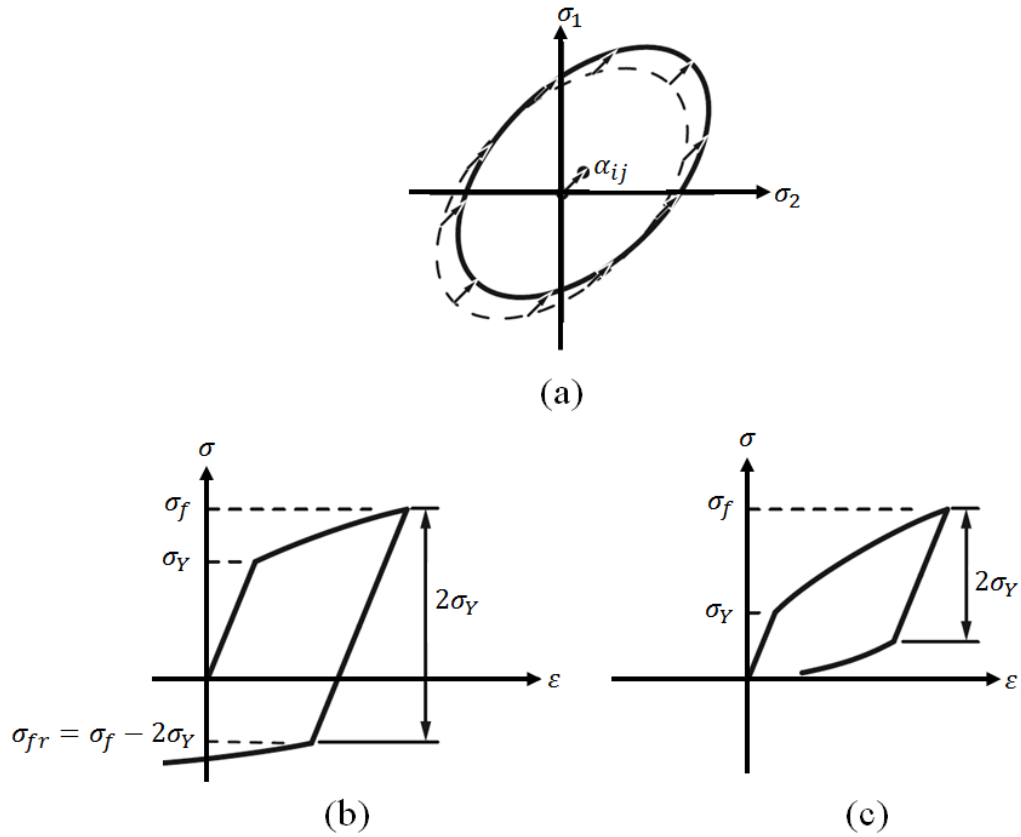


Figure 22 Kinematic hardening: (a) Shift of the yield surface caused by kinematic hardening (b) Stress-strain curve for reversed with low hardening material (c) Stress-strain curve for reversed with strong hardening material [12]

Under the applied loading and plastic deformation, the surface translates to the new location with the initial centre point translated by absolute kinematic hardening variable $|\sigma_{fr}|$. The stresses relative to the new yield surface centre in subsequent yielding during hardening can be expressed as in Equation 36 [93].

$$f(\sigma_{ij}, \alpha_{ij}) = \sqrt{\frac{3}{2} (S_{ij} - \alpha_{ij})(S_{ij} - \alpha_{ij})} - Y = 0 \quad (36)$$

α_{ij} is the kinematic hardening variable and often called a back stress. Since α_{ij} is defined in space, it has the same component as the deviatoric stress S_{ij} .

Usually, the material starts with a kinematic behavior. With increasing strain level, the kinematic behavior saturates and isotropic hardening takes place. To describe the behavior of α_{ij} as a function of the strain and strain rate level, several models are available such as the models from Armstrong and Frederick [94] and the Yoshida model in [95]. Equation 36 represents general yield condition for kinematic hardening behavior.

Isotropic and kinematic hardenings represent the easiest ways to model strain hardening in materials processing [12, 93]. Thus the maximum load, the tensile strength, and the onset of necking occur at a strain equal to the strain-hardening exponent n , assuming that strain hardening is described by Equation 35 [96].

Materials such as polymers exhibit strain hardening as well as unequal tensile and compressive yield stresses by load reversal as in compressive loading of a sample, which was initially loaded in tension. The effect resulting from unequal tensile and compressive yield stresses by load reversal is referred to as Bauschinger-effect. The Bauschinger-effect is also observed in cyclic loadings [71]. As shown in Figure 22 (b) $|\sigma_{fr}| = \sigma_f$, which illustrates that isotropic hardening law cannot predict Bauschinger-effect accurately and not suitable to model most polymer and cyclic processes.

Kinematic hardening law is illustrated in Figure 22 (b) and (c) where $|\sigma_{fr}| < \sigma_f$, which proves the ability of this hardening law to capture Bauschinger-effect and model most polymer and cyclic processes.

The effects of temperature, strain-rate, and anisotropy are also significant in the yield behaviour of polymers. The large strain deformation response of amorphous polymers results primarily from orientation of the molecular chains within the polymeric material during plastic straining. Molecular network orientation is a highly anisotropic process, thus the observed mechanical response is strongly a function of the anisotropic state of these materials [68]. Yield criteria and studies of anisotropy in oriented polymers are given in [20, 81 and 82].

4.6 Temperature and Strain Rate Dependences of Yield

Relaxation processes play an important role in the deformation of polymers. As they are thermally activated at sufficiently high temperatures, the probability of a relaxation process increases exponentially with the temperature and also with the time available for the process. The relation is expressed in Equation 37 [12, 15].

Polymer chains have to overcome an energy barrier Q of a relaxation to slide past an adjacent segment and enable the deformation. The probability P_{r0} to overcome this barrier by thermal activation can be expressed by Equation 37 [12]:

$$P_{r0} \propto \exp\left(-\frac{Q}{kT}\right) \quad (37)$$

with the temperature T and Boltzmann constant k .

Assuming that the application of the stress σ provided the activation energy to overcome the barrier, thus acts on a molecular segment of cross section A and if the width of the barrier is b_0 . The work W done by the applied stress to overcome the barrier is represented in Equation 38 [12, 15]:

$$W \approx \sigma A b_0 \quad (38)$$

The probability to overcome the barrier is thus given by Equation 39 [12, 15]:

$$P_{r1} \propto \exp\left(-\frac{Q - \sigma A b_0}{kT}\right) \quad (39)$$

The total probability P_{r1} to overcome the barrier is the difference of Equation 37 and 39. Assuming that the total probability P_{r1} is directly related to the rate of change of strain, Equation 39 can be written as in Equation 40 [12, 15]:

$$\dot{\varepsilon} \propto \dot{\varepsilon}_0 \exp\left(-\frac{Q}{kT}\right) 2 \sinh\left(\frac{\sigma A b_0}{kT}\right) \quad (40)$$

$\dot{\varepsilon}_0$ is assumed a constant in Equation 40 and represents damper elements connected in series in the four-parameter model discussed in Section 4.2 [12, 15].

Equation 40 can be used to study time dependence of the elastic and plastic behaviour as well as for strain rate-temperature. For small stresses, the approximation $\sinh x \approx x$ in this Equation can be used. The strain rate becomes thus proportional to the applied stress [12, 15]. In this case, the behaviour is linear and viscous. As stresses are small, the deformation is not plastic, but elastic, for there is a restoring force corresponding to the spring element depicted in Section 4.2, whereas Equation 40 describes the damper element of the Kelvin-Voigt model also discussed in Section 4.2. The behaviour is thus linear viscoelastic. At larger stresses, deviations from linearity occur, although the behaviour is still viscoelastic [12].

Polymers deform mostly by creep at relevant temperatures such as elevated temperature in blow forming process. In contrast to the viscoelastic deformation, there is no restoring force in viscoplasticity. To describe the time-dependence of plastic deformation, Equation 40 is thus used to describe the damper element connected in series in the four-parameter model shown in Section 4.2.

For large stresses, the approximation $2 \sinh x \approx \exp x$ applied to Equation 40 can be used to formulate Equation 41 [12, 14 and 15]:

$$\frac{\sigma}{T} = \frac{k}{A b_0} \left(\frac{Q}{kT} + \ln \frac{\dot{\varepsilon}}{\dot{\varepsilon}_0} \right) \quad (41)$$

$\dot{\epsilon}_0$ is a constant in Equation 41. In the case of tensile test at yield, substituting $\sigma = \sigma_{YT}$ and since $\dot{\epsilon}_0 = C$ a constant, Equation 41 is rearranged to give Equation 42:

$$\frac{\sigma_{YT}}{T} = \frac{k}{Ab_0} \left(\frac{Q}{kT} + \ln \frac{\dot{\epsilon}}{C} \right) \quad (42)$$

Thus, Equation 42 shows a linear relationship between σ_{YT}/T and $\ln \dot{\epsilon}$ for a tensile test [20]. A plot of the ratio of yield stress to temperature σ_{YT}/T as a function of the logarithm of strain rate $\ln \dot{\epsilon}$ for polymer materials show that points at constant temperature T , fall onto a common line to represent a form of Eyring plot. The Eyring plot for polycarbonate PC is depicted in Figure 23 to illustrate the relationship.

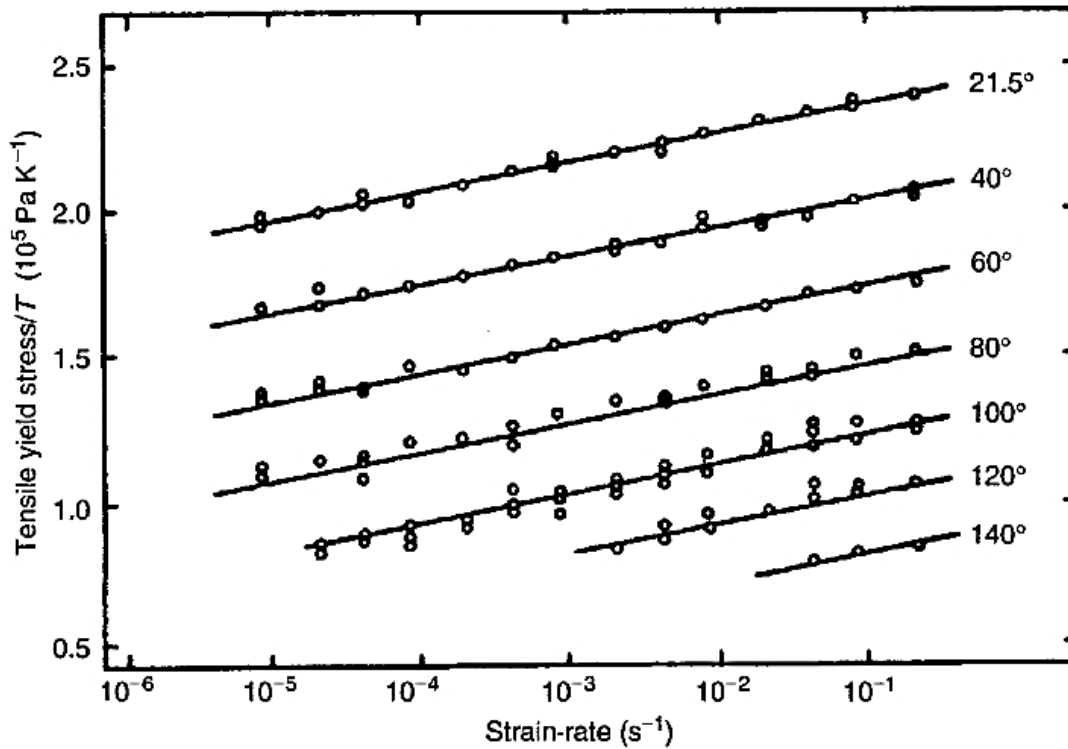


Figure 23 The measured ratio of yield stress to temperature as a function of the logarithm of strain rate for polycarbonate PC in a tensile test. “ \circ ” represents measured data and the set of parallel straight lines are calculated from Equation 42 [15]

Figure 23 illustrates that yield stresses for polycarbonate polymer material at low temperatures and high strain rates increase more rapidly [12, 15 and 20]. Accordingly temperature and strain rate have opposite effects. Increasing the strain rate or decreasing the temperature will lead to higher stress levels with small strain value [12, 15 and 54]. The influence of strain rate and temperature on the tensile properties of elastomers and amorphous polymers has been studied extensively [12, 15, 20 and 60].

4.7 Instability

Most material properties and dimensions usually considered to be uniform in analyses are actually inhomogeneous. Furthermore, the cross-sectional diameter or thickness may vary from one place to another. There may also be variations in grain size in case of metals or molecular weight distribution for polymeric materials [71, 96]. The effect of material inhomogeneities can cause materials deforming plastically not to deform homogeneously. The strains in certain local regions increase more rapidly than it does in the sample as a whole. In a limiting case plastic strain may occur only in certain local regions [97].

In the following sections the characteristics of the various types of strain inhomogeneity that have been observed in polymers are described. The inhomogeneities are not exclusive to polymers and have a close parallel to plastic deformation in metals. The arguments below about the geometry of the deformation are based on the assumption that plastic flow is occurring at constant volume. [97].

Inhomogeneous deformation occurs because homogeneous deformation has become unstable. There are two possible reasons for this instability, one geometrical and one structural, and they can both occur at once [97]. The emphasis in this work is on instability associated with the geometry polymeric micro tube.

4.7.1 Necking

The most well established phenomenon associated with plastic instability in polymer is that of necking and the basic theory is generally attributed to Considère.

An example of a geometrical instability is the formation of a neck in a sample tested in uniaxial tension. If part of the sample should happen to be slightly thinner than the rest then the stress there will be slightly higher. This will concentrate further deformation at that point and increase the local stress further unless the rate at which the material strain-hardens is sufficient to suppress the instability. The critical rate of strain hardening is given by the construction from Considère in Figure 24 [15, 97].

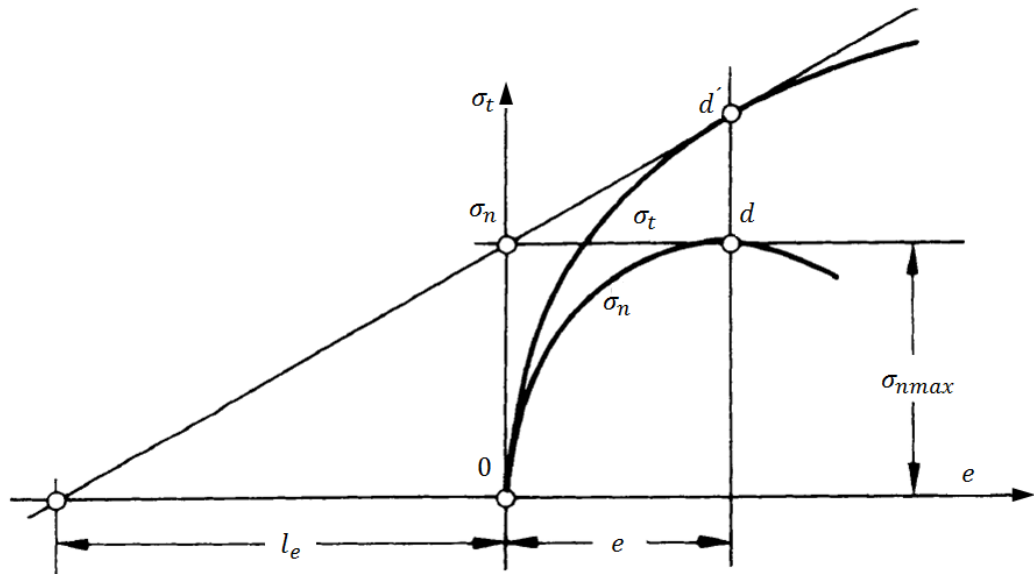


Figure 24 Construction by Considère. The point d , which is a maximum on the engineering stress curve, σ_n , is also a tangent from the point $l_e = 0$ on the true stress curve [97]

Let the true tensile stress on a sample of initial cross sectional area A_0 and initial length l_0 be σ_t . If the length and area are l_e and A respectively, then expression for constant volume can be written as in Equation 43:

$$\frac{A}{A_0} = \frac{1}{1 + e} \quad (43)$$

where e is the nominal strain. The nominal stress σ_n is given by Equation 44:

$$\sigma_n = \frac{\sigma_t}{(1 + e)} \quad (44)$$

Equation 44 has a maximum or minimum value when as in Equation 45:

$$\frac{d\sigma_n}{de} = 0 \quad (45)$$

Equation 46 gives the maximum point σ_{nmax} as:

$$\frac{d\sigma_t}{de} = \frac{\sigma_t}{(1 + e)} \quad (46)$$

Equation 46 [16, 86] shows that maxima or minima will occur in the nominal stress at points where lines drawn from the point $e = l_e$ on the strain axis are tangential to the true stress versus strain curve. Figure 24 illustrates that the maximum of σ_n and the tangent to the true stress-strain curve occur at the same elongation e points d and d' . This construction is called the Considère construction [15, 97]. When the material has properties that can be described as in Figure 24 and by Equation 46, then any further increase in elongation e beyond point d leads to fall in stress σ_n .

4.7.2 Strain Softening

Strain softening is another reason for instability of material after the yielding point as depicted in Figure 25.

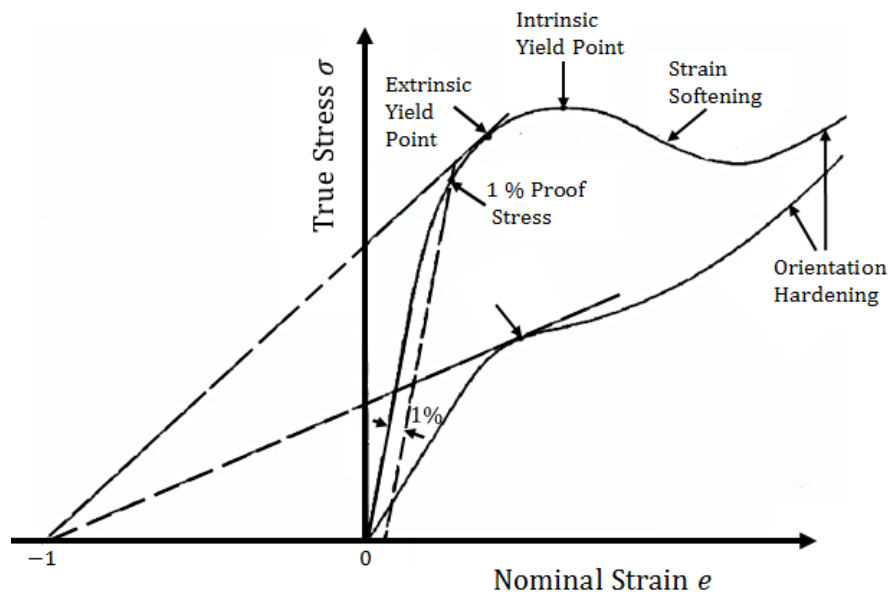


Figure 25 Schematic true stress versus nominal strain curves for amorphous glassy polymers

A tangent to the curve through the point on the abscissa, nominal strain $e = -1$ is the Considère construction and defines the extrinsic yield point of a sample tested in tension [84].

If locally the strain should happen to be slightly higher than elsewhere due higher stress concentration then the material will be softer locally and it will therefore deform to higher strain than elsewhere and become softer still. This process can only be stopped by the eventual orientation hardening of the material. Once the deformation becomes unstable the rate at which any inhomogeneity develops is limited by the strain-rate sensitivity of the flow stress. If this is small then a small local increase in stress or a small degree of local softening will cause a large increase in the local strain rate and the inhomogeneity will develop rapidly. If it is large then the local inhomogeneity will develop slowly [84, 97].

The only strain inhomogeneity that is geometrically possible to form with negligible restraint in any direction from the surrounding material is a symmetrically necked region in a sample tested in tension.

5. Dynamic Mechanical Analysis (DMA)

5.1 Introduction

Polymers are viscoelastic materials, whose mechanical behavior exhibits viscous and elastic characteristics. Of the different methods for viscoelastic property characterization, dynamic mechanical techniques are the most popular, since they are readily adapted for studies of both polymeric elastic and viscous properties. They are often referred to collectively as dynamic mechanical analysis (DMA) [98]. The term viscoelastic means the combination of viscous and elastic properties such as in stress relaxation, creep and dynamic mechanical behaviour. The behaviours can occur in tensile and in shear deformation as well as in volume retardation [99].

Dynamic mechanical analysis involves imposing sinusoidal (cyclic) strain on a sample in a temperature controlled chamber and measuring the resulting stress response, or equivalently, imposing a sinusoidal stress on a sample and measuring the resultant strain response. In most commercial DMA instruments strain is the controlled input, while the resulting stress is measured. DMA is used also to study molecular relaxation processes in polymers as well as to determine inherent mechanical or flow properties as a function of time and temperature [98].

Viscoelastic transitions or relaxations in amorphous polymers include T_g and several secondary transitions resulting from relaxation processes that are observed at temperatures below T_g . In semi-crystalline polymers there is often an additional secondary relaxation between the melting temperature T_m and the glass transition temperature T_g . These relaxations are of continuing scientific interest and engineering importance. They are intimately associated with the stiffness of engineering thermoplastics, impact toughness, diffusion rates of low molecular weight vapors and liquids, and the effectiveness of plasticization, among others. There are three significant points of interest in relation to characterizing relaxation processes namely: determining in what phase they originate, describing the molecular processes underlying them, and relating relaxation behavior to engineering properties and practical applications [98].

Three main classes of factors, which influence DMA experiments include: Instrumental, test frequency and material characteristics factors.

In a DMA experiment at a constant frequency, sometimes referred to as isochronal experiments on amorphous polymers, the highest temperature relaxation domain is the glass transition. The relaxation domains are associated with the amorphous phase. For semi-crystalline polymers, the relaxation domains are in the temperature domain between T_m and liquid nitrogen temperature of $-196\text{ }^\circ\text{C}$, [98] at least three relaxation processes domains are often found namely: sub-glass transition temperature T_β , glass

transition temperature T_g and the melting temperature T_m . They occur in the listed order [100]. The glass transition temperature is within this temperature domain and this is different from the case of amorphous polymers [98]. DMA experiments may be conducted in an isochronal manner by varying the temperature at a fixed frequency, or in an isothermal manner by varying the frequency at a fixed temperature [101].

The various relaxations are influenced by polymer structure, morphology, and environmental factors. For example, the intensity, temperature position, and temperature range of the glass transition in semi-crystalline polymers depends on the degree of crystallinity and morphology of the polymer. These will also vary depending on the processing history of the material [98].

The glass transition temperature T_g is important from a practical perspective. For many polymers it determines the highest use temperature, while at the same time it defines the lowest possible processing temperature [102].

The polymeric material properties listed in Table 1 below were collected from polymeric bulk materials of the polymeric micro tubes used in this study. Hence, there is a need to investigate the glass transition temperature T_g of the micro tubes.

5.2 Determining Glass Transition Temperature T_g of Polymeric Micro-Tubes Using DMA

The technique of DMA involves the measurements of strain and stress in the dynamic analysis of a sample at elevated temperature to evaluate the storage modulus E' and the loss modulus E'' . The storage modulus E' , and the loss modulus E'' are defined as in Equations 47 and 48:

$$E' = \frac{\sigma}{\varepsilon_0} \cos \delta \quad (47)$$

and

$$E'' = \frac{\sigma}{\varepsilon_0} \sin \delta \quad (48)$$

where E' is the storage modulus, E'' is the loss modulus and δ is the phase difference δ of the input and the response of strain or stress been measured.

Mathematically these moduli are out of phase (phase difference) by the angle δ , the ratio of the moduli is defined as Tan δ or loss tangent and given in Equation 49:

$$\text{Tan } \delta = \frac{E''}{E'} \quad (49)$$

The numerical values of $\text{Tan } \delta$, storage modulus E' and loss modulus E'' vary with temperature and reach a maximum at T_g , after which it rapidly falls, making the position of the maximum distinct.

The glass transition T_g is identified from dynamic mechanical data because of the sharp decrease in storage modulus E' (or shear storage modulus G'), and the corresponding loss dispersion in E'' (shear loss G'') or $\text{Tan } \delta$ also called Δ that occur at T_g [103]. When the mode of deformation is shear: the shear storage modulus, (G'), shear loss modulus (G''), and $\text{Tan } \delta = G''/G'$ are used.

For the determination of T_g from DMA data, the maximum storage modulus E' or maximum $\text{Tan } \delta$ can be selected. The values are different and the maximum loss modulus is often used because the T_g value obtained from the maximum $\text{Tan } \delta$ is several degrees higher than that the maximum of E'' . The $\text{Tan } \delta$ value corresponds more closely to the transition midpoint or inflection point of the decreasing curve of E' on a logarithm plot. For polymers that have unusually broad glass transitions such as cross-linked and semi-crystalline, maximal $\text{Tan } \delta$ occurs at a much greater glass transition interval [98].

From molecular and practical or forming processes, the working temperature T_f of many thermoplastic polymers can be defined as the softening point. The onset of the softening point is related to the initiation of segmental molecular motions and loosening of the polymer structure associated with T_g . It is clear that at the transition midpoint or inflection point at maximum $\text{Tan } \delta$, the softening point already has been exceeded. In this region substantial molecular relaxation involving increased segmental motions of the polymer chains occurs. Thus the temperature at maximum $\text{Tan } \delta$ maximum is more sensitive to parameters such as molecular weight, cross-link density and morphology [103]. Related to this is the observation that for many polymers the value of $\text{Tan } \delta$ increases by about 7 °C for each decade increase in frequency while the loss modulus maximum rises only about 3 °C [104]. The glass transition temperature T_g is a kinetic quantity, so it changes with frequency [98].

In selecting a criterion to be used for specifying T_g , the application of T_g data need to be considered; The DMA T_g data for a material can be considered, to measure material consistency of the material property, to evaluate the effects of processing or as an engineering property where the T_g value has significance as a structural property. If measurement precision is foremost, the choice of either E' or $\text{Tan } \delta$ might be taken depending on acquired data. It also should be noted that the data can be better illustrated by plotting modulus or $\text{Tan } \delta$ on a linear rather than on logarithmic scale.

Many factors influence the measurement of T_g by DMA methods. These can be grouped as: instrumental, test frequency and material characteristics factors.

- Instrumental factors

Several instrumental factors affect determination of the glass transition from DMA data, such as error in the thermocouple or thermocouple placement, temperature gradients within the sample chamber (or oven) or within the sample proper, and exceeding the compliance limitations of the machine. These factors are specific to each individual instrument. Some instruments allow the user to input software corrections to correct errors in thermocouples but fail to allow their proper electronic calibration by the user. Each instrument has a different size and shape oven, employs different heating and cooling mechanisms, and has a variety of gas flow rates. Finally, the instruments are constructed with various rigidities and offer a variety of sample clamping configurations. The modulus and the dimensions of the sample and the geometry all combine to determine whether the compliance limits of the machine have been exceeded. All of these factors are highly specific to a given instrument [105].

- Test frequency

Since the glass transition is inherently kinetic, it is strongly influenced by the rate or frequency of mechanical energy input. It has been observed that substantial molecular relaxation involving cooperative segmental motions of the polymer chains occurs in the region of T_g . The rate of this segmental motion depends on temperature, so that if the test frequency is increased, the relaxations associated with the glass transition have difficulty in keeping up with the mechanical strain input, and the polymer appears to be more rigid. The segmental motions associated with T_g can in such case only occur at a higher temperature. Thus T_g increases with frequency as illustrated in Figure 26 [105].

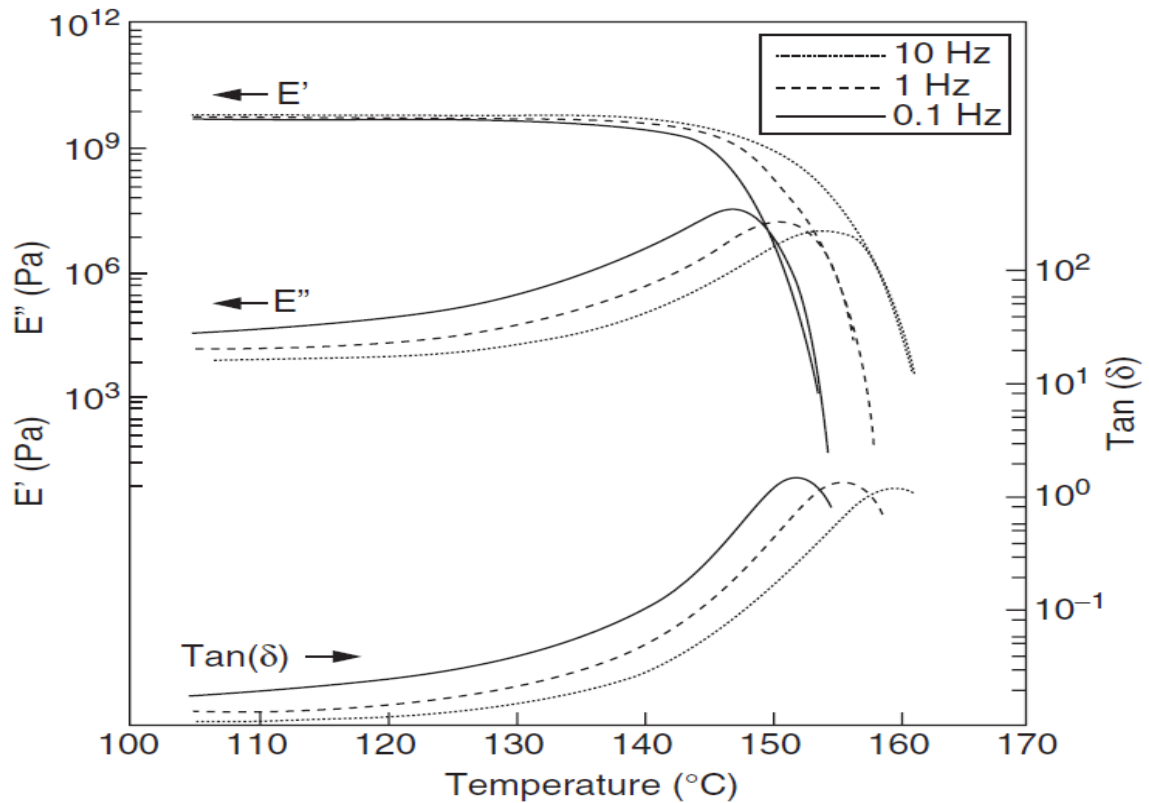


Figure 26 DMA curves for polycarbonate at several frequencies [105]

This Figure illustrates the characteristic features of the transition with increasing frequency. In the Figure, a general decrease in the intensity of E'' or $\text{Tan } \delta$, broadening at the maximum point, and a decrease in the slope of the storage modulus curve in the transition region can be observed for polycarbonate material. The secondary transitions or relaxations for polycarbonate and other aromatic chain polymers with high T_g are well separated. Their variation in T_g increases with frequency as depicted in Figure 26 [105].

- Material characteristics

In semi-crystalline polymers the fact that the amorphous and crystalline phases are intimately interconnected has a significant effect on relaxation at the glass transition, resulting in a broadening of the transition region. In polymers that develop a high degree of crystallinity, the glass transition is suppressed so that the glass transition loss dispersion appears as a relatively minor event and in some cases may be difficult to detect at all.

From a practical view, the physical and mechanical properties of highly crystalline polymers are dominated by the presence of crystallinity, and their upper use temperature limit is T_m and not T_g . Thus, the glass transition has less significance in this class of materials than it does in amorphous polymers, where T_g generally represents the maximum use temperature. It should be noted that below T_g crystalline polymers tend to be more brittle than they are above T_g . This can lead to problems due to cracking under stress during low temperature applications. For semi-crystalline polymers the ratio T_m/T_g varies between 1.5 and 2.0, with several exceptions [106, 107].

The challenge in measuring the glass transitions in crystallizable polymers involves the possible crystallization during the measurement at temperatures below T_m . Crystallizable polymers that are quickly cooled from the molten state often have poorly developed or no crystallinity. When such materials are heated above their T_g , crystallization occurs spontaneously at temperatures between T_g and T_m [98].

5.3 DMA Experiments with the Polymeric Micro Tubes

5.3.1 Materials

The review of polymeric materials was focused mainly on the macroscopic stress - strain behavior of various polymer candidates, including information regarding their percentage crystallinity, strain rate and temperature dependence as well as the glass and melt transition temperatures. A difficulty to acquire desired polymeric micro tubes in the required dimensions was also a factor in the selection of materials. Polymer micro tubes in the desired tube d_{a0}/s_0 ratio were only commercially available for PA 6. The d_{a0} represents initial outer diameter, while s_0 is the micro tube wall thickness. The most critical dimension affected by extrusion shaping process is the wall thickness as well as the thickness distribution across the shaped polymeric micro tube.

Based on material and market review, three optically clear polymer micro tubes were specified and purchased. The polymeric micro tubes are PA 6 Nylon, PET and PC. PA 6 Nylon micro tubes were commercially available and obtained as a semi-finished material from a serial product supplier, PET and PC micro tubes were obtained as prototypes from a research institute specialized on polymer fibre processing. Table 1 below shows the tube dimensions and the selected polymeric materials properties relevant to blow forming process.

Table 1 Selected Polymeric Materials Properties at room Temperature [18, 99 and 108-114]

	PA 6 Nylon	PET	PC
	Polyamide 6	Polyethylene terephthalate	Polycarbonate
Polymer class	Thermoplastic: semi-crystalline	Thermoplastic: amorphous/ semi-crystalline	Thermoplastic: amorphous
Trade Name of the Suppliers	Goodfellow Nylacast	M & G Cleartuf	M &G high viscosity, moulding and extrusion
Density ρ [kgm⁻³]	1.15x10 ³ -1.17x10 ³	1.29x10 ³ -1.39x10 ³	1.19x10 ³ -1.21x10 ³
E-Modulus E [GPa]	3.36-3.53	2.8-3	2.32-2.44
Poisson's ratio ν	0.34-0.36	0.381-0.396	0.391-0.407
Tensile stress at yield σ_{YT} [MPa]	82.1-90.5	55-60	62.7-72.4
Compressive stress at yield σ_{YC} [MPa]	112-123	50-60	69-86.2
Elongation at Break [%]	20-45	280-320	110-120
Hardness (Rockwell M)	84-92	28-30	70-75
Melting point T_m [°C]	227-238	260-280	226-322
Glass transition temperature T_g [°C]	44-56	60-84	142-158
Maximum Crystalline region [%]	65	41	0
Coefficient of Heat Transfer λ_p [Wm⁻¹ K⁻¹]	0.29	0.29	0.19-0.22
Specific Heat Capacity c_p [Jkg⁻¹ K⁻¹]	1700	1150	1200-1300
Coefficient of Thermal Expansion α_p [10⁻⁶ K⁻¹]	80	70	65-70
Water Absorption [% per 24 h]	1.30-1.90	0.10	0.10

Polyethylene terephthalate PET

PET is a thermoplastic that can be found either in an amorphous or a semi-crystalline state. Its microstructure exhibits therefore a mix of an amorphous phase and a crystalline one, with a given ratio, ranging from nearly zero to about 45 % (fully crystallized PET) [113]. Since PET properties were published by [114] many authors have studied the morphology changes of PET [46]. The Structure of PET was shown in Chapter 2.

PET like most polymers exhibit time and temperature dependent mechanical behavior as well as highly nonlinear response during loading and unloading [115]. Over the years the mechanical behavior of PET has been extensively studied [116], from early drawing experiments in [118] to modern in situ Fourier transform infrared spectroscopy (FTIR) and Wide-angle X-ray scattering (WAXS) experiments on PET films [118]. Dupaix and Boyce [116] studied stress versus strain behavior of amorphous PET and PETG (polyethylene terephthalate Glycol) over a wide range of temperatures (25-110 °C) and strain rates (0.005-1.0 s⁻¹) through conduct of uniaxial and plain strain compression experiments. PET has remained a popular research subject. However, in spite of the large amount of experimental literature on PET, many aspects of the mechanical behavior remained unexplained in particular the effects of strain induced crystallization on the stress-strain behavior [116].

The many studies on PET have however not addressed the characterization of PET micro tubes. Due to the gap in the characterization of PET micro tubes, DMA experimental tests in this chapter were designed and conducted to determine the T_g of PET micro tubes.

Polyamide 6 PA 6 Nylon

Polyamides PA encompass a group of condensation products of amines and carboxylic acids containing amide groups. The chemical structure was also depicted in Chapter 2 and can be deduced by the numeric numbers that are added to the abbreviation PA in each case. The most common representatives, marketed under the trade names Nylon PA 66 and Perlon PA 6, are fibre products that differ in the constitutions of their monomers. Besides synthetic fibres, there is a growing number of technical applications of the compact material. Most polyamides except, for instance PA 61 are semi-crystalline possessing the features of morphological hierarchy. Due to their relatively high capacity to absorb water, their mechanical properties additionally depend on the humidity. The absorption of water by the amorphous phase yields a softening effect, resulting in enhanced toughness [119].

PA 6 also called Nylon-6, is a family of thermoplastics characterized with high E-modulus for crystals along the molecular chains (165 GPa) [120] as well as strong intermolecular interactions, which result in a higher melting temperature around 220 °C [120]. Itoa et al. in [120] studied the effects of molecular weight on the drawing and drawing and in [121] the effects of the crystalline forms on the deformation behavior of

PA 6 were presented. Murthy et al. [122] investigated the influences of crystal growth, orientation of amorphous and crystalline domains on properties of PA 6 during drawing and annealing. Despite the many studies on PA 6, publications on characterization of PA6 micro tubes are presently not available. To determine the glass transition temperature T_g of PA 6 micro tubes, the characterization of the tube materials were conducted for this work with the same testing methods for PET micro tubes.

Polycarbonates PC

Glassy polymers, such as polycarbonate PC are common engineering materials that have found uses in consumer products ranging from portable computers and optical lenses, to automotive components and appliance housings due to the high ductility and low density properties. PC is also being considered for several specialized applications because it has the potential to offer significant weight savings and better protection against relevant threats [123, 124]. However, PC as an amorphous thermoplastics, exhibits brittle behavior under certain loading conditions, such as high strain rates, highly triaxial stress states, and certain temperature regimes [123].

Polycarbonates and glassy polymers have been the focus of many experimental investigations to understand their mechanical behaviors under different types of load. Boyce et al. [69] examined and compared the very different stress-strain results of polycarbonate produced from four types of mechanical testing: uniaxial compression, plane strain compression, uniaxial tension, and simple shear. Chang and Cheng [125] characterized polycarbonate near glass transition temperature. A study of the bulge-forming of PC sheet was conducted in [126]. Nanzai et al. [127] studied plastic deformation and non-Newtonian flow in glassy polycarbonates. However, most of the studies on polymeric materials behaviors focused less on polymeric micro tubes.

5.3.2 Experimental Methods

The dynamic mechanical analyses for the polymeric micro tubes were conducted with the thermal analysis equipment model Q800 from TA Instruments and depicted in Figure 27. In the experiment the mechanical properties as a function of time, temperature, and frequency were measured. Tube dimensions and experimental conditions for the multi frequency strain test are given in Table 2 below for the micro tubes.

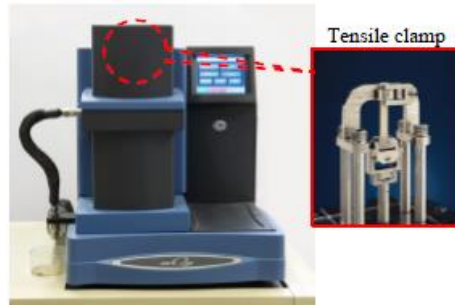


Figure 27 Thermal Analysis Equipment Model Q800 from TA Instruments

Table 2 Polymer Micro Tube Dimensions and Conditions for the DMA Experiments with Q800

Frequency [Hz]: 1.0 Temperature ramp rate [°C/min]: 3 Micro tube section length (Gauge Length) L_0 [mm]: 25					
Polymeric material	Tube material (Identifier)	Dimensions		Range of temperatures [°C]	
		d_{a0} [mm]	s_0 [mm]	Min	Max
PC	PC04	0.4	0.160	25	180
	PC134	1.34	0.170	25	180
PET	PET134	1.34	0.170	25	100
	PET1	1.02	0.125	25	100
PA 6	PA 6-134	1.34	0.170	15	80

The DMA experiments were conducted on the polymeric micro tube with the section length $L_0 = 25$ mm. The temperature was scanned from room temperature to the temperature range of the respective polymeric micro tube as given in Table 2. An operating frequency of 1.0 Hz, different pre-loads (static force), force track (auto strain), and a temperature ramp rate of 3 °C/min were used. The moduli of the micro tubes were measured as a function of temperature. The pre-load (static force) was required with tensioning clamps in order to sustain oscillation.

The Q800 model has a temperature range from -150 to 600 °C and the following modes of deformation: dual/single cantilever and 3-point bending, tension, compression and shear. The DMA unit was used in a tension mode.

5.3.3 Experimental Results and Discussion

PET Micro Tubes

For the PET tubes dimensions, strain was set at 0.04 %, pre-load was set at 0.01 N, and a 125 % force track was used to maintain sample tension. Testing results are shown in Figure 28. For these tubes, the glass transition temperature T_g was measured to be in the range of 72.3 and 83.3 °C. The storage modulus at room temperature was measured to be around 1.6 GPa.

The evolution of the storage modulus, loss modulus and Tan Delta as function of the working temperature was not affected by the micro-tube dimensions. However, the loss modulus recorded for PET1 was approximately 200 MPa and PET134 300 MPa. The peak value (maximum) of the Loss modulus was used to define T_g in this study. The same approximate maximum Tan delta was recorded for both micro-tube dimensions.

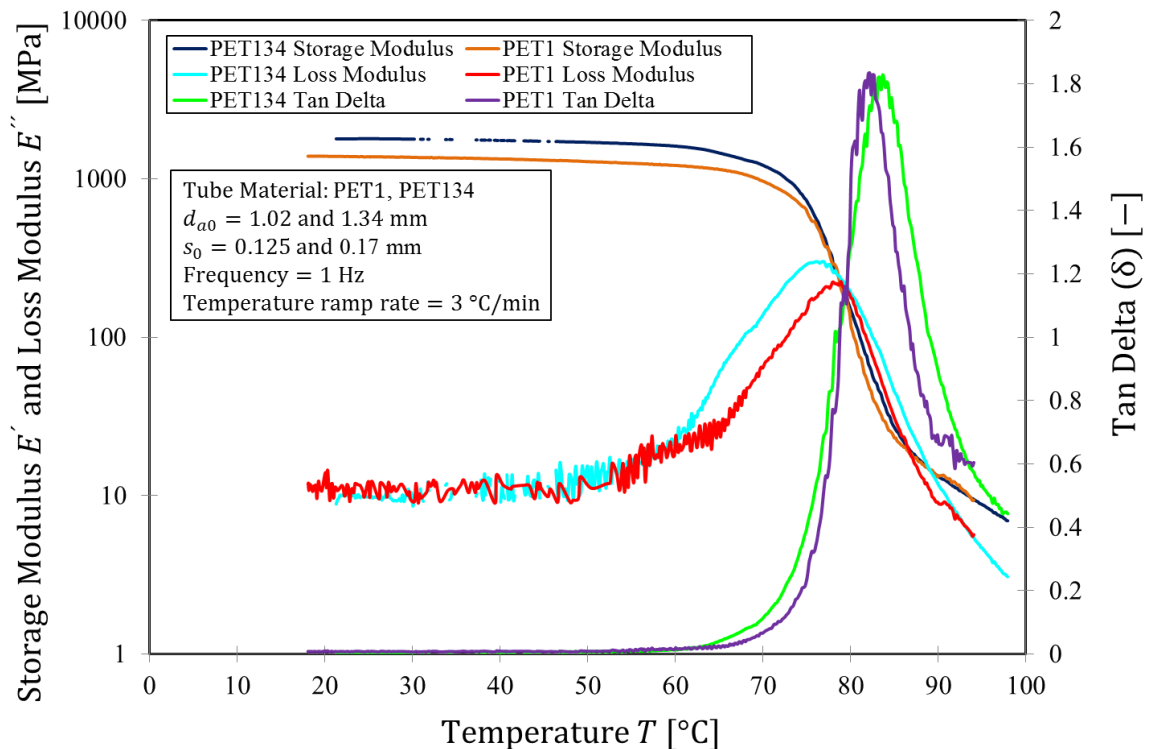


Figure 28 Evolution of Storage Modulus E' and Loss Modulus E'' and Tan δ , as a function of Temperature for the PET Tubes Materials of different Dimensions

Oscillations illustrated in the Figure by $T < 65$ °C were due to the low pre-load applied in the tests.

The Storage Modulus E' and Loss Modulus E'' were plotted on the logarithmic scale, while Tan δ is plotted on a linear scale for clearer illustration of the experimental result data.

PA 6 Micro Tubes

For PA 6 tubes, the strain was set at 0.08 %, pre-load of 0.25 N, and 115 % force track was used to maintain sample tension. The test result is shown in Figure 29. The glass transition temperature was measured to be in the range of 35 and 59 °C. The storage modulus at room temperatures was measured to be around 1.3 and 1.859 GPa.

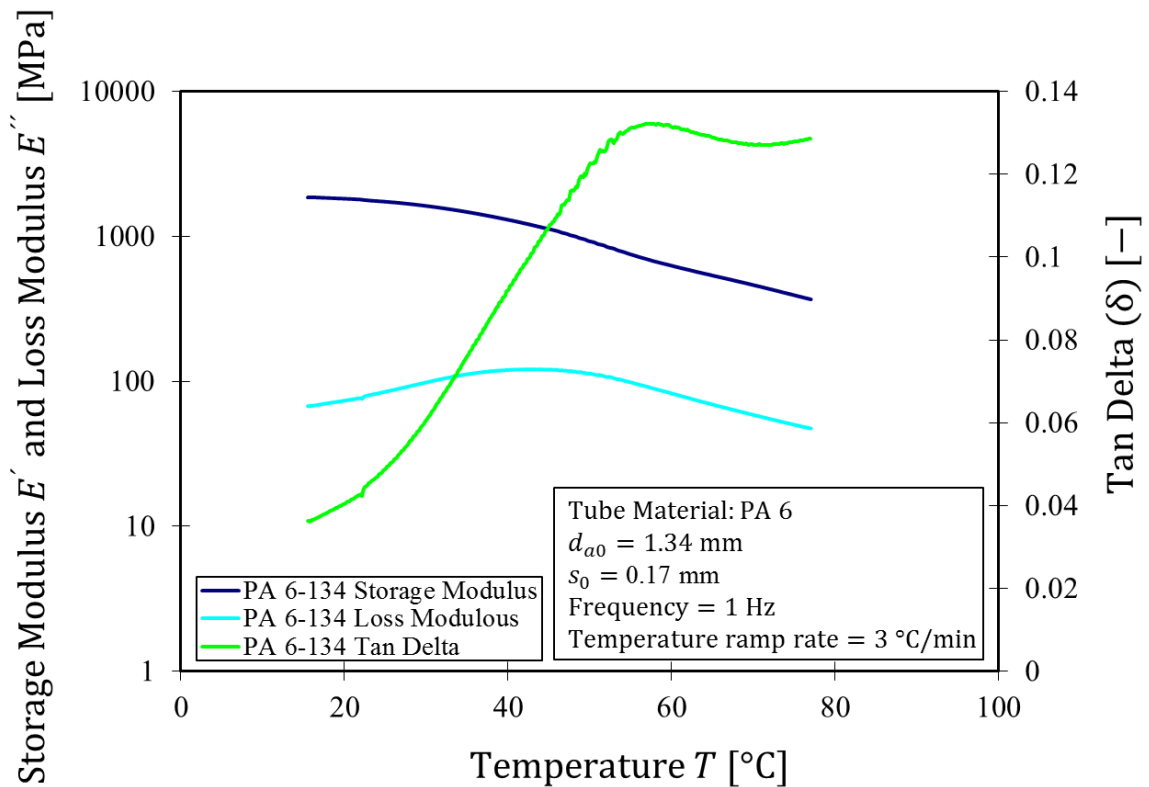


Figure 29 Evolution of Storage Modulus E' and Loss Modulus E'' and Tan δ , as a function of Temperature for the PA 6 Tubes Material

Similar to Figure 28, the Storage Modulus E' and Loss Modulus E'' were plotted on the logarithmic scale and the Tan δ plotted on a linear scale.

PC Micro Tubes

Single-Frequency, strain controlled, temperature sweep experiments were conducted on PC tubes. For the tube with $d_{a0} = 1.34$ mm, the strain was 0.04 %, and the pre-load set at 0.04 N. A 125 % force track was used to maintain sample tension. For the tube with $d_{a0} = 0.4$ mm, a strain of 0.06 %, pre-load of 0.02 N, and force track of 125 % was applied. Testing results are shown in Figure 30. For these tubes, the glass transition temperature was measured to be in the range of 141 and 169 °C. The storage modulus at 25 °C was measured to be 2.3 GPa.

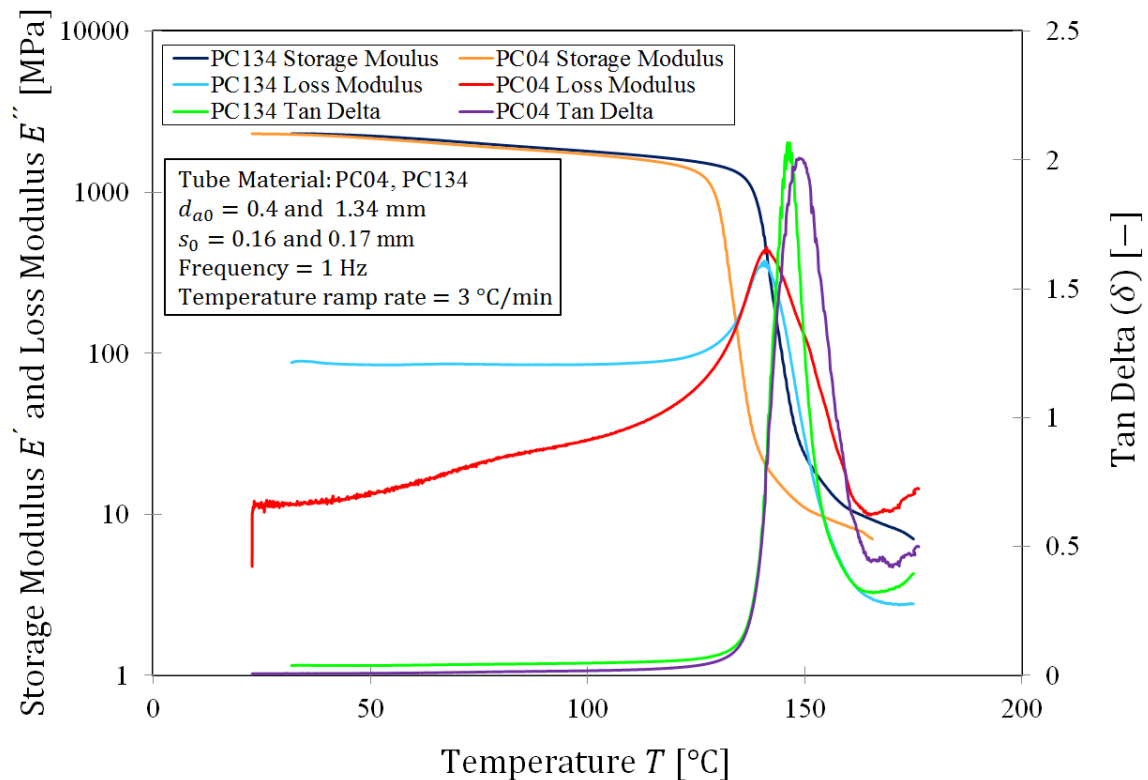


Figure 30 Evolution of Storage Modulus E' and Loss Modulus E'' and $\text{Tan } \delta$, as a function of Temperature for the PC Tubes Material

It is shown from the results that the storage modulus versus temperature curves for PC tubes of different dimensions are close to each other. Similar results were observed for the Tan Delta versus temperature curves. Therefore, evolution of storage modulus with temperature, and evolution of Tan Delta with temperature is not affected by tube dimensions for PC. PET micro tubes showed similar behaviour.

6. Free-Forming Experiments

6.1 Introduction

The free-forming experiments enabled investigations into the down-scaling of conventional blow molding process for micro manufacturing application as well as the formability limit of the polymeric micro tubes tested. The investigations presented in this Chapter were from the second stage of the investigations as described in Chapter 1.3 on the study methodology and were based on *Concept 1* of the process configuration presented in Chapter 3.

Micro IR-radiators described in the experimental device below provided the process heating source for the experiments. The heating process with the IR-radiators was calibrated prior to the free forming experiments and the results were presented in the experimental device description in Chapter 6.2. A uniform micro tube average temperature of 93 °C was achieved in 2 min span after micro IR-radiators were supplied with power for the experiments. The values of the required power supply corresponding to an approximate working temperature T_f were determined during the calibration of the IR-radiators used.

Characterization of materials mechanical behavior in the regime of about 0.1 to 1000 s⁻¹ true strain rate $\dot{\epsilon}$ are very challenging due to instrumentation limitations and the complexity of data analysis involved in dynamic loading [130, 131]. The Split Hopkinson bar is the widely used device to test materials in this regime [22]. In this study of fundamentals for the volume manufacture of polymeric hollow micro parts, polymeric micro tubes formability and manufacturing parameters were investigated using a custom designed mechanical-pneumatic device. An effective stretch ratio rate $\dot{\lambda} \leq 1000 \text{ s}^{-1}$ can be achieved with the equipment.

To measure total deformation up to 30 %, which is far beyond the measurable range of electric resistance strain gages, 3D Digital Image correlation is usually used to resolve deformation measurement and the displacement of sample instead from actuator motion. Using this technique, the stresses measured for true strain rates equal to 100 s⁻¹ or less show little or no noise compared the to load cell signals. When the true strain rates are higher than 250 s⁻¹, noises and oscillations in the stress measurements can be significantly decreased from about 250 to 50 MPa [131].

Image correlation technique applied in this study employed a 2D digital camera to capture the evolution of the micro tube deformation.

6.2 Free Forming Experiments with Polymeric Micro Tubes

6.2.1 Materials and Sample Geometry

The material selection for the experiments was mainly based on formability, functional requirements and availability as described in Chapter 4. Figure 31 depicts the PET and PA 6 micro tubes coil. The dimensions of the polymeric micro tubes investigated at this second stage of the investigations are listed in Table 3 below.

Formability investigations conducted were predominantly with PET micro tubes because of the wide application in conventional blow moulding processes and polymeric hollow parts. PC micro tube were not investigated here, because the results from the DMA experiments in Chapter 5 and the IR-radiators calibration in Chapter 6.2.2 showed that the glass transition temperature T_g of the PC tube material exceeded the maximum achievable temperature with the IR-radiators. The IR-radiators were used as the heating source in the free forming experiments.

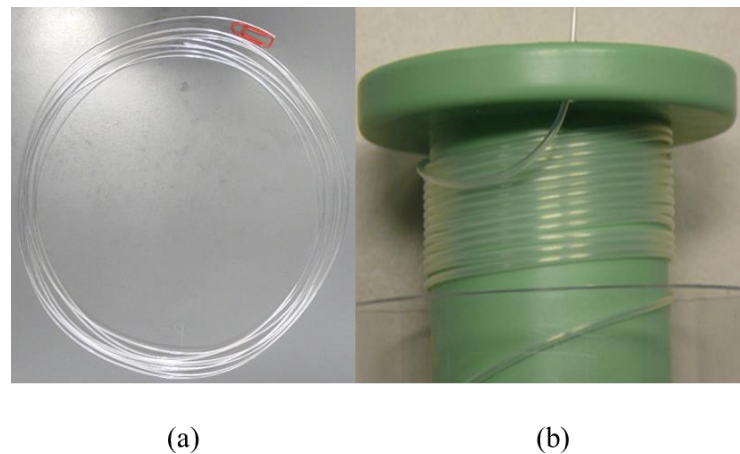


Figure 31 (a) PET Micro Tube Coil, $d_{a0} = 1.02$ mm and $s_0 = 0.125$ mm (b) PA 6 Micro Tube Coil (supply length 5 m), $d_{a0} = 1.34$ mm and $s_0 = 1$ mm

Table 3 Dimensions of the Micro Tubes Investigated in the Free Forming Experiments

Tube material (Identifier)	Polymeric material	Trade name of the suppliers	d_{a0} [mm]	d_{i0} [mm]	s_0 [mm]
PET1	PET	M&G Cleartuf	1.02	0.77	0.125
PET134	PET	M&G Cleartuf	1.34	1.00	0.17
PA 6	PA 6	Nylacast	1.34	1.00	0.17

Prior to free forming tests, micro tube length section $L_0 = 45$ mm depicted in Figure 32 was cut from the micro tube coil shown in the Figure 31, while the measuring points tagged are shown in Figure 33.

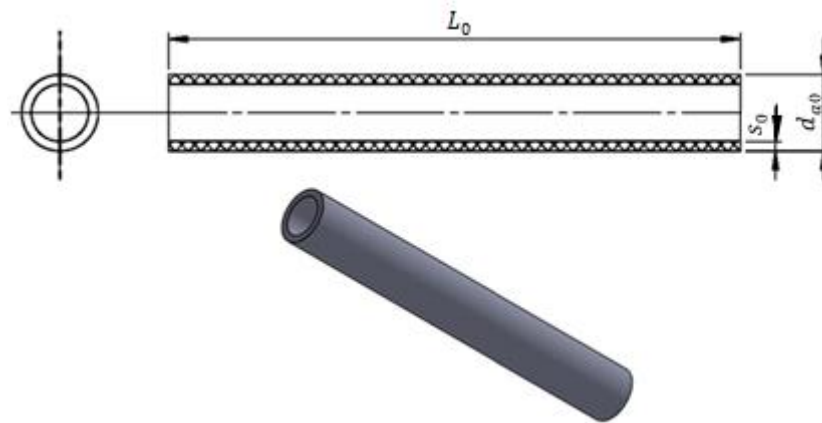


Figure 32 Schema of the Polymeric Micro Tube Cut Section

Dimensions of the outer diameter d_{a0} recorded varied from 1003.84 to 1073.24 μm as listed in Table 4. The tagged measuring points depicted in this Figure 33 were positioned near the median cross section of the cut micro tube length L_0 with initial dimensions d_{r0} in the hoop direction and d_{z0} in the axial direction.

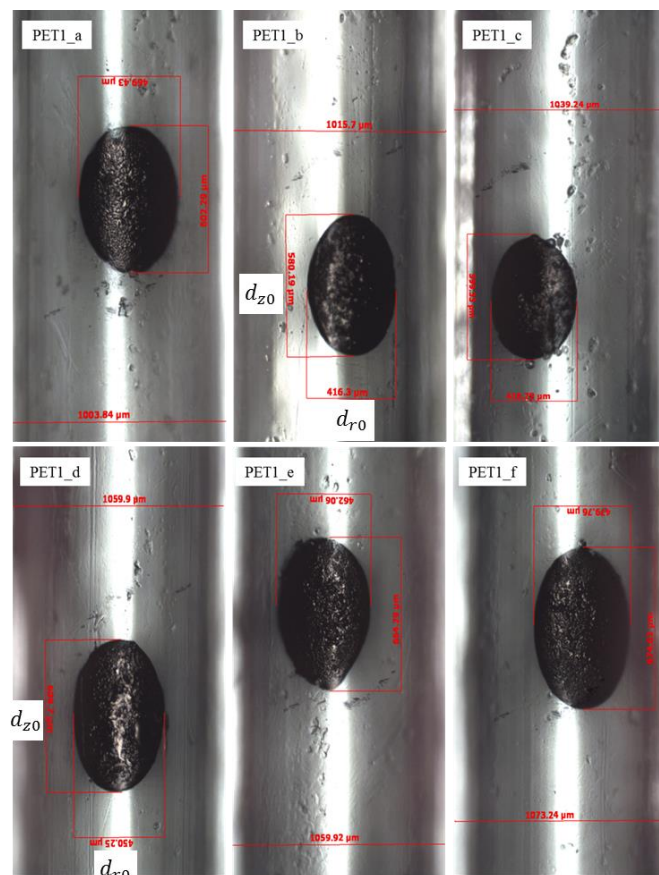


Figure 33 Material: PET Micro Tube Section with tagged measuring points, desired dimension: $d_{a0} = 1.02 \text{ mm}$ and $s_0 = 0.125 \text{ mm}$. Cut Section Length $L_0 = 45 \text{ mm}$

A homogenous deformation of the micro tube was assumed to associate the local deformation to the measuring point on the PET micro tubes outer surface. To estimate the variation in the outer diameter d_{a0} , the standard deviation was determined and presented in Table 4.

Table 4 Deviations recorded across the Coil Section of the PET Tube Material with Supplied Dimensions: $d_{a0} = 1.02$ mm and $s_0 = 0.125$ mm

Experiment Nr.	PET1_a	PET1_b	PET1_c	PET1_d	PET1_e	PET1_f
Supplied d_{a0} [μm]	1003.84	1015.7	1039.24	1059.9	1059.92	1073.24
Desired d_{a0} [μm]	1020.00					
Desired d_{i0} [μm]	770.00					
d_{a0} Standard deviation	0.03					

The estimated standard deviation 0.03 in the outer diameter d_{a0} of the micro tube sections for the experiments equals the deviation given by the manufacturer. However, the 0.03 standard deviation recorded is significant in micro manufacturing and influenced the conduct of the experiments. Due to the limits of the available measuring equipment, the measurement of the internal diameter d_{i0} across the length section and eventually the micro tube wall thickness s_0 distribution was not conducted.

During the experiments the IR-camera produced the real time image of the process temperature development, while the digital camera captured the real time image of the deformation development of the PET micro tube under p_i and F_z loads. 30 images were acquired per second and were used to evaluate the formability of the micro tubes.

The tagged measuring points were captured by the digital camera, which enabled optical image correlation of the micro tube deformation. The Illuminant sub-module of the Image Grabbing module provided a background in a contrasting colour and the focus of the camera was positioned to directly face the tagged measuring points depicted in Figure 33. The cameras were placed on the opposite side of the sub-module Illuminant. The acquired images were after the experiments loaded and post-processed with image processing software. The initial dimensions of the tagged measuring points and the subsequent dimensions were first calibrated in the image software. The change in dimensions after forming was then determined to quantify the formability of the micro-tube. The corresponding time when the tagged measuring point reached certain dimension was determined by analyzing the frames in images captured by the digital camera. The different shapes and sizes of the tagged measuring points did not influence the measuring results decisively.

6.2.2 Experimental Device

The experimental equipment and platform shown in Figure 34 was used in the free-forming experiments. The device concept and development were based on the reviews from Chapters 2 to 4 as well as the dynamic mechanical analyses results presented in Chapter 5.

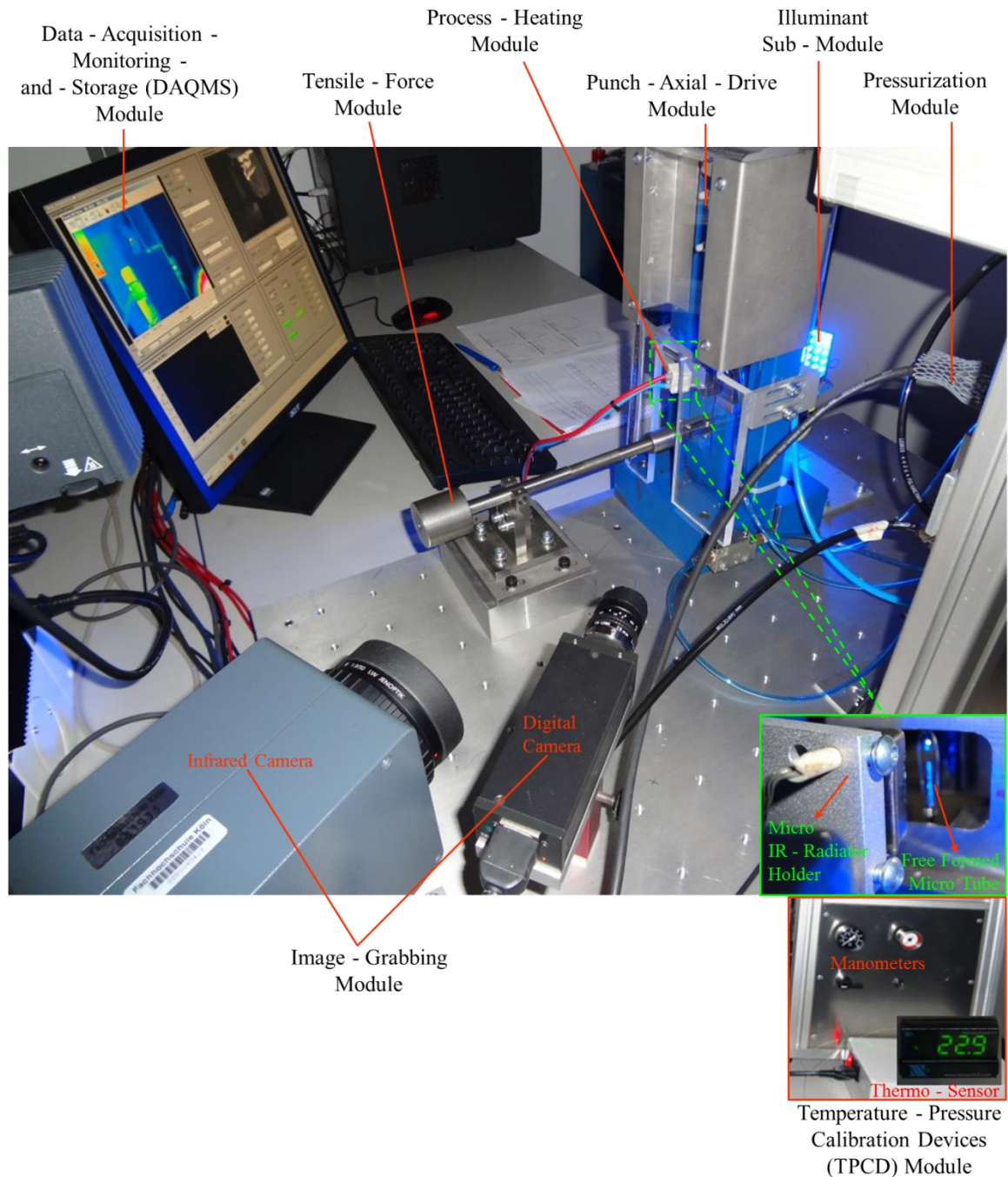


Figure 34 The Free-Forming Experimental Equipment and Platform

The equipment modules on the platform include: Pressurization and Punch-Axial-Drive modules which are directly connected to the air treatment and supply unit. The platform

consists also of Data Acquisition Monitoring and Storage (DAQMS) module. Other Modules on the Platform are: Tensile-Force, Process-Heating, Temperature-Pressure Calibration Devices (TPCD) and Image-Grabbing. The Illuminant sub-module enhances the working of the Image-Grabbing module. This modular concept employed in the design for the free forming experiment enabled a controlled process chain, easy scale-up and transfer to a functional machine system and reliable integration into a production platform. Description of the module and sub-modules are detailed follows:

Punch-Axial-Drive Module

The module regulates axial movement of the sealing punch and provided sealing force of about 200 N. The module consists of the following elements:

- 5/2-way valve, single-solenoid (Model: SYJA5000)
- Actuator (Compact-Cylinder) (model: CD55B20-10).

Both elements were purchased from SMC Pneumatics Germany. The actuator controls vertical movement as well as the stroke of the sealing and pressurization module. Limiting of the module displacement or proximity was achieved mechanically (hard-stop). This module was designed to offer flexibility for different micro tube dimensions without interface exchange.

Pressurization Module

A piezo proportional pressure valve with pressure range of 8.5 bars was employed in this module to precisely apply the forming internal pressure p_i desired. Air was the pressurization medium and regulated by the piezo proportional valve. Absolute Pressure transducers with measuring range of 0-10 bars and the HBM AE101 bridge amplifier from HBM Germany to provide bridge excitation and amplification were integrated in the pressurization module to monitor on-line the process pressure development. The module elements are:

- Piezo proportional pressure valve (Model: PRE1-U02)
- Absolute pressure transducer (Model: P3IC/P3ICP)
- Amplifier for the Pressure transducer (Model: Industrial amplifier AE101).

The Piezo proportional pressure valve was purchased from AirCOM pneumatic Germany and the pressure transducer from HBM Deutschland also in Germany.

Filtered compressed air supplied at maximum supply pressure $p_{is} = 10$ bar to the piezo proportional pressure valve in accordance with the design specifications. Figure 35 depicts the schema of the process pressurization diagram.

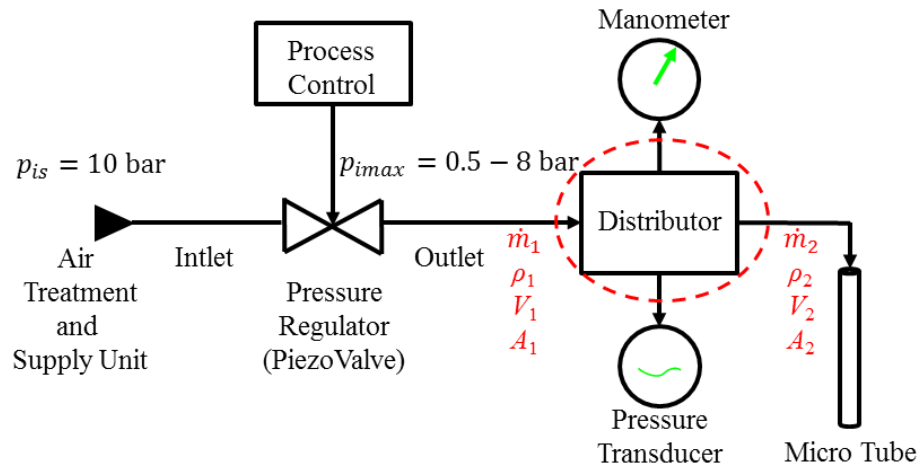


Figure 35 Schematic of the Connections for the Process Pressurization Module

p_{is} shown in Figure 35 represents the supplied air of 10 bar from the air treatment and supply unit, which is connected to the inlet nozzle of the pressure regulator. The p_{imax} is the regulated and controlled process air to the Pressurization module at pressure regulator outlet nozzle. The pressure valve (regulator) is a piezo-operated 3-port/2-way proportional pressure regulator with internal pressure sensor and closed loop description.

For the PRE1-U08 model, a maximum flow rate of 350 lmin^{-1} is achievable by $p_{is} = 10$ bar at the usage maximum internal pressure $p_{imax} \leq 6$ bar. A single steady flow stream was assumed between the pressure regulator and the micro tube as expressed in Equation 50:

$$\dot{m}_1 = \dot{m}_2 \quad (50)$$

Although the volume flow rates into and out of a steady-flow device may be different for compressible flow as in the experiments carried-out here due change in density of air [132]. Since the ratio between the pressures supply of 10 bar and the applied $p_{imax} \leq 6$ bar is greater than 1.9 then it is reasonable to assume a choked flow, which ensured constant flow [133]. Argument of constant flow could also be supported due to the micro tube dimension, closed-system condition and the absolute small distance between the micro tube and the pressure regulator. Hence, equilibrium balance of the volume flow rate around the distributor depicted in Figure 35 could be represented by Equation 51:

$$\rho_1 V_1 A_1 = \rho_2 V_2 A_2 \quad (51)$$

ρ in the Equation represents air density at room temperature and A is taken as the cross sectional area of the air supply nozzle exit base.

Process-Heating Module

This module provided adequate heating required for the micro blow forming process. The module consists of two micro infrared heaters from Elstein-Werk M. Steinmetz GmbH & Co. KG Germany and depicted in Figure 36.

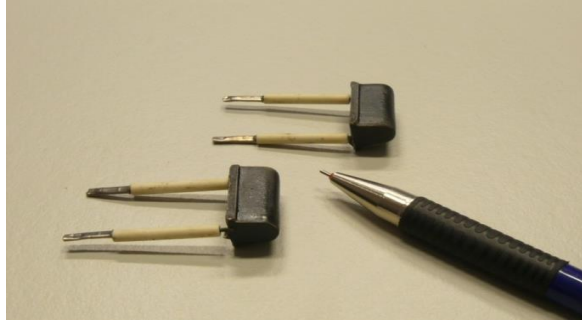


Figure 36 Micro Infrared (IR) Heaters. Model MSH/20

The Elstein micro heaters of the model type MSH/20 are ceramic infrared radiators in small design with heating surface dimensions of 20 x 10 x 9 in mm. They reach operating temperatures up to 860 °C and surface rating of 100 kWm⁻². The MSH/20 micro heaters require 55 W and 12 V power supply to generate wavelength range of 2-10 microns (μm). Two laboratory power supplies ensure power supply to the IR-radiators. The IR-radiators were mounted one on each side of the micro tube to achieve heating of the micro tube and positioned at an absolute distance of 15 mm to the centre-line of the undeformed micro tube to avoid carburization of the tube before and during the expansion process.

Tensile-Force Module

The two basic functions of this module are: to compensate tube elongation due to heating and avoid the sagging of the tube in the case of mould-insert forming. In addition, the superimposed tensile force contributed to the multiaxial orientation of the formed part. The module consists of the following elements:

- Positioner
- End-Effector.

The positioner is a mechanical cantilever beam made from high yield strength steel material. The End-Effector is a pinch gripper made from the same material as the positioner to prevent thermal stress and improve positional accuracy. The test equipment design allowed for the linear and swivel displacement of the positioner and the End-Effector. The displacement mechanism of the positioner ensured the micro tube remained in vertical position for the forming period and also sealed the Lower-End of the micro tube.

The Lower-End of the tube is driven by F_z provided by this module, while the Upper-End is sealed by the Punch-Axial-Drive module. The tensile force F_z provided superimposed axial loading of the micro tube. The system mechanism concept ensured that at time $t = 0$, the effective load on the micro tube was $\sum F_z = 0$ and only maintained the micro tube cut section length L_0 .

The End-Effector functions to firmly grip, seals and pulls the Lower-End section of the tube thereby stretching and imposing axial orientation during a forming cycle. The Pressurization module provided the Upper-End section with pressurized air.

Image-Grabbing Module

The Image-Grabbing module consists of the following elements:

- Infrared Camera
- Digital Camera
- Sub-Module namely: Illuminant.

The hardware for the Image-Grabbing was fixed on the experimental platform. Given the number of hardware options available, the selection of components depends on the efficiency and functional requirements of the particular application.

To monitor and measure the process temperature development, a thermographic system of the model type VarioCAM HiRes 780/30 mm (v2.3) from InfraTec GmbH Germany was employed. The system captures long wave infrared spectral range of 7.5 to 14 μm and 25 images per second at the specified 50/60 Hz image acquisition rate. A resolution 640 x 480 or 384 x 288 pixels is achievable with this camera system. The centre-line of the Tube Section distance to IR-camera was 460 mm.

In order to resolve deformation measurement of the polymeric micro tube, a 2D Digital camera for a simplified application and at reduced cost was used. For this study a SONY XCD-SX910v3.06F model digital camera was integrated in the Image-Grabbing module. The digital camera is characterized with a resolution of 640 x 480 and 1 x 8-Bit Image. 30 images were captured at the camera specified 30 Hz image acquisition rate on the application platform. Attached to the objective of the digital camera was a filter of the model FB470-10 from Thorlabs GmbH, Germany. The filter is an $\text{Ø}25.4$ mm Bandpass Filter, characterized with $\text{CWL}=470 \pm 2$ nm, $\text{FWHM}=10 \pm 2$ nm transmission features. While CWL represents the central wavelength, FWHM is the full width at half maximum as illustrated in Figure 37.

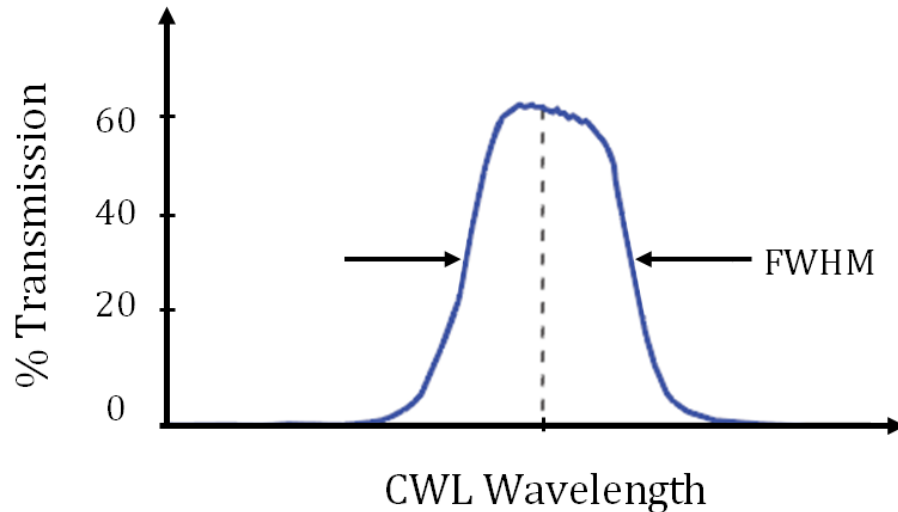


Figure 37 Typical Transmission Characteristics of Filters from Thorlabs GmbH, Germany

Typically, a filter or combination of filters is used to attenuate the light intensity or to block or pass specific spectral wavelengths in the recorded image. They are often used in machine vision, parts inspection, and research applications. Usually, linear image processing filters are characterized in terms of their frequency responses, specifically by their spectrum shaping properties. The centre-line of the Tube Section distance to Digital Camera was 320 mm.

Illuminant Sub-Module

The Illumination sub-module was the illumination source for the Image-Grabbing module and consists of emitting diodes and a slab of Plexiglas as shown in Figure 38. The Light Emitting diodes (LEDs) were the light source of the sub-module. Non-laser LEDs such as emitting diodes provide a cheaper and more compact option because of their small size. They can provide light at various wavelengths with low power consumption and low heat generation. Lasers can also be used as light sources, but they are expensive and are commonly employed only for specialized techniques such as confocal fluorescence microscopy and optical trapping [134].

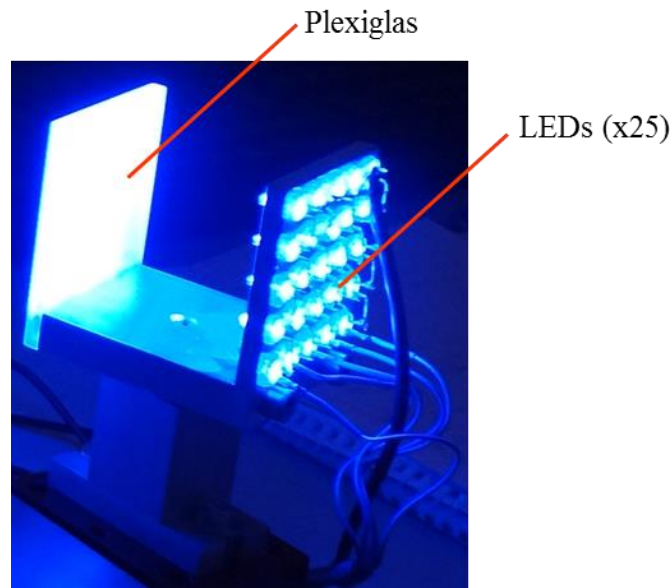


Figure 38 Image Grabbing Sub-Module: Illustration of the Elements of the Illuminant

The 25-LED, 5 mm blue array of model LED 5-3500 BL was used for the sub-module. The LEDs were mounted and distributed on a 300 cm² aluminum block.

The blue light from the illuminant had a wavelength of 420-490 nm as such passed through the FB470-10 filter model attached to the digital camera. The LED 5-3500 BL model used in this study is characterized with a wavelength of 468 nm, luminous intensity of 1700-2600 mcd, a 30° angle of radiation and an operating voltage of 2 to 3.6 V.

The Plexiglas enabled transmission of the wavelength ranges as those of blue LEDs, disperse and direct the light on the micro tube. The combination of these properties makes it possible to employ modern LED technology with maximum efficiency.

The objective of the LEDs and Plexiglas was to improve the visibility, perceptibility and detectability of the micro tube in the experiments. These enabled cleaning the image from various types of noise, enhancing the contrast among adjacent regions or features, simplifying the image via selective smoothing or elimination of features at certain scales, and retaining only features at certain desirable scales. Image enhancement is usually followed by or is done simultaneously with detection of features such as edges, peaks, and other geometric features, which is of paramount importance in low-level vision [135].

Temperature Pressure Calibration Devices (TPCD) Module

The TPCD module consists of the following elements:

- Manometer
- Thermo Sensor Element.

Manometer (Pressure gauge) with limit indicator and pressure range of 0 to 10 bar was used to monitor and calibrate the elements of pressurization module. The manometer is of the model G36-10-01-L from SMC Pneumatics Germany and has precision indication of $\pm 3\%$ in full gauge span.

Prior to the free forming experiments, standard calibration procedure was conducted on the Process-Heating module with the Thermo Sensor Element to determine the absolute distance between the micro IR-radiators and the clamped micro tube relationship with achievable temperature with the IR-radiators. Infrared camera was also employed in the calibration experiments as shown in Figure 39 to assess the temperature distribution in the calibration process.

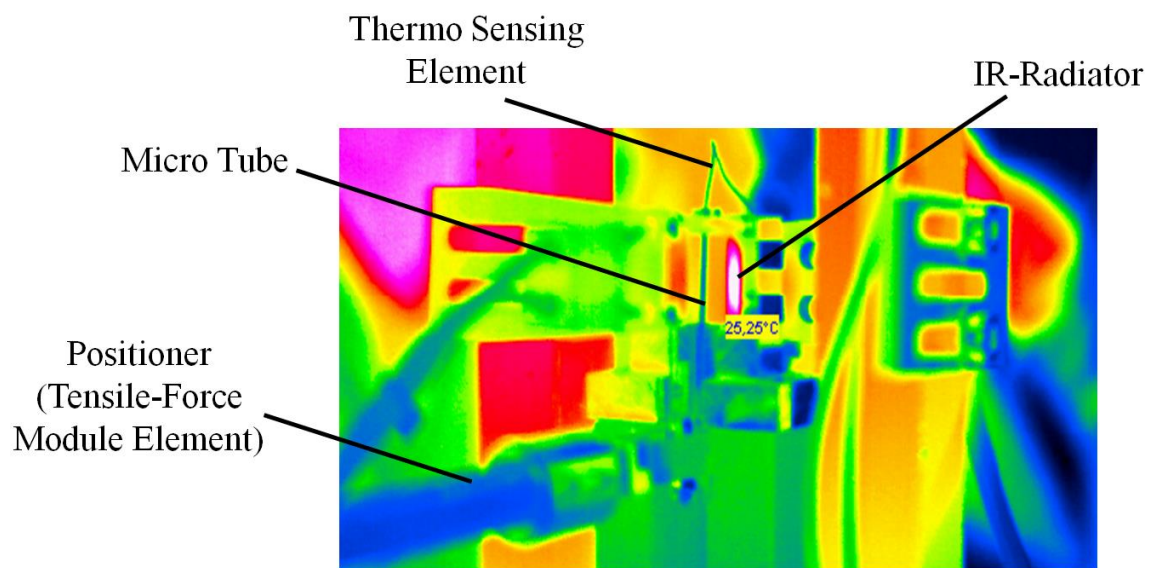


Figure 39 IR-Radiators Calibration: Thermal Image of Temperature Distribution with IR-Camera and Thermo Sensing Element at the Centre-Line of a clamped Micro Tube

Calibrations were also conducted on the surface of the micro tubes as depicted in Figure 40 to investigate the temperature distribution.

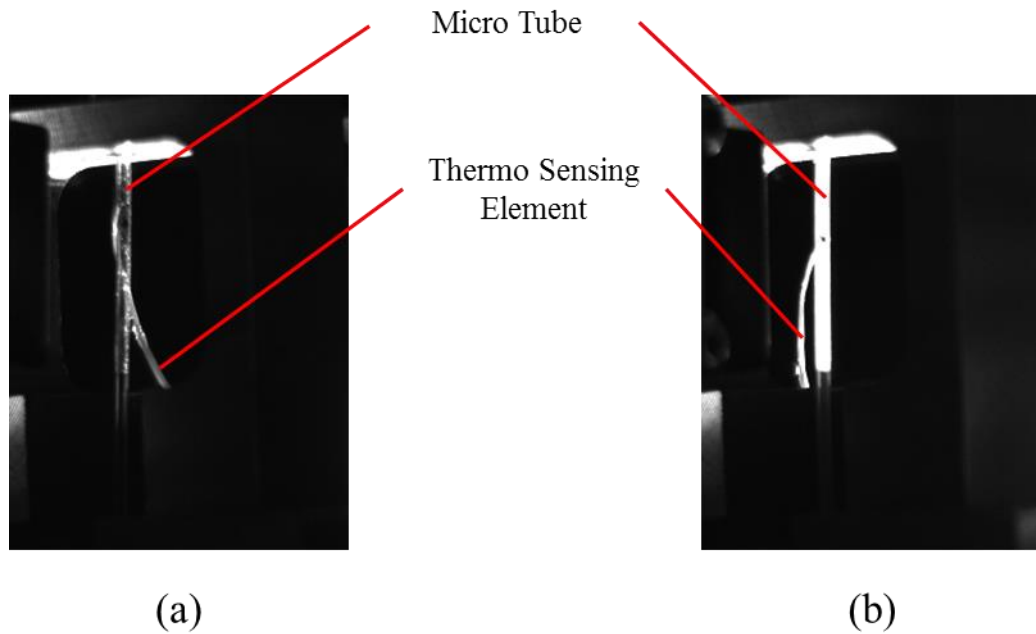


Figure 40 IR-Radiators Calibration: Temperature Sensing of the Micro Tube Surface with Thermo Sensing Element; (a) PET Micro Tube (b) PA 6 Micro Tube

The Parameters investigated were: voltage and current of the micro IR-radiators, temperature at the centre-line of a clamped micro tube, the absolute distance between the centre-line of the clamped micro tube and the surface of the micro IR-radiators as illustrated in Figure 41 below. The parameters were systematically varied in an experimental plan. Temperature readings at the centre-line and the surface of the micro tubes were observed to be of equal value in the time range from 0.5 to 1 ms after the IR-radiators were switched-on. The investigations were conducted at 15 mm absolute distance between the clamped micro tube and the IR-radiators on each side.

Results of the investigations for PET micro tubes with the dimensions: outer diameter d_{a0} 1.34 and 1.02 mm, wall thickness s_0 0.170 and 0.125 mm are given in Table 5.

Table 5 Calibration results of the Micro IR-Radiators

Tube materials. PET1, PET134 and PA 6 Dimensions [mm]: d_{a0} 1.34-1.02 and s_0 0.170-0.125 Tube section length L_0 [mm]: 45 Absolute distance [mm]: 15 Current [Amp]: 6.81 Power (AC) [V]: 10 Room temperature T_0 [°C]: 20 Applied maximum internal pressure p_{imax} [bar]: 1-6 Increase interval of the maximum internal pressure p_{imax} [bar]: 0.5		
Experiment Nr.	Time [s]	Average (mean) temperature at the centre-line of the micro tube with standard deviation of 3 % [°C]
02	240	98
05	600	95.5

The micro IR-radiator holders were designed to enable variation and adjustment of the absolute distance between the micro IR-radiators and the centre-line of the clamped micro tube for different micro tubes dimensions. The absolute distance between the micro IR-radiators and the micro tubes differ for different polymers and dimensions.

The temperature controller used in this study was an i32/iS32 Series model from OMEGA Engineering, Inc. dba Newport Electronics USA. The model has a simplified on/off control to offer unparalleled flexibility in process temperature measurement using Pt100 thermocouple. The i32/1S32 model Thermo Sensor was operated as stand-alone.

Through the systematic calibration to determine the working temperature T_f and absolute distance correlation, the results from the i32/1S32 model proved to be repeatable and reliable. The IR-camera readings were applied to monitor the evenness of the working temperature T_f distribution.

The average temperature of 93 °C recorded in the calibration of IR-radiators was above the glass transition temperature T_g of 72.3-83.3 °C observed for the PET micro tubes and 35-59 °C for PA 6 micro tubes as presented in Chapter 5. Thus the IR-radiators model MSH/20 from Elstein-Werk M. Steinmetz GmbH & Co. KG Germany were used as the heat source for the free-forming experiments described below.

6.2.3 Experimental Method and Plan

Figure 42 illustrates the experimental method to investigate the formability of the micro tubes. The free-forming process configuration accounts for the polymeric material behaviour and design considerations in the micro manufacturing applications discussed in Chapter 2.

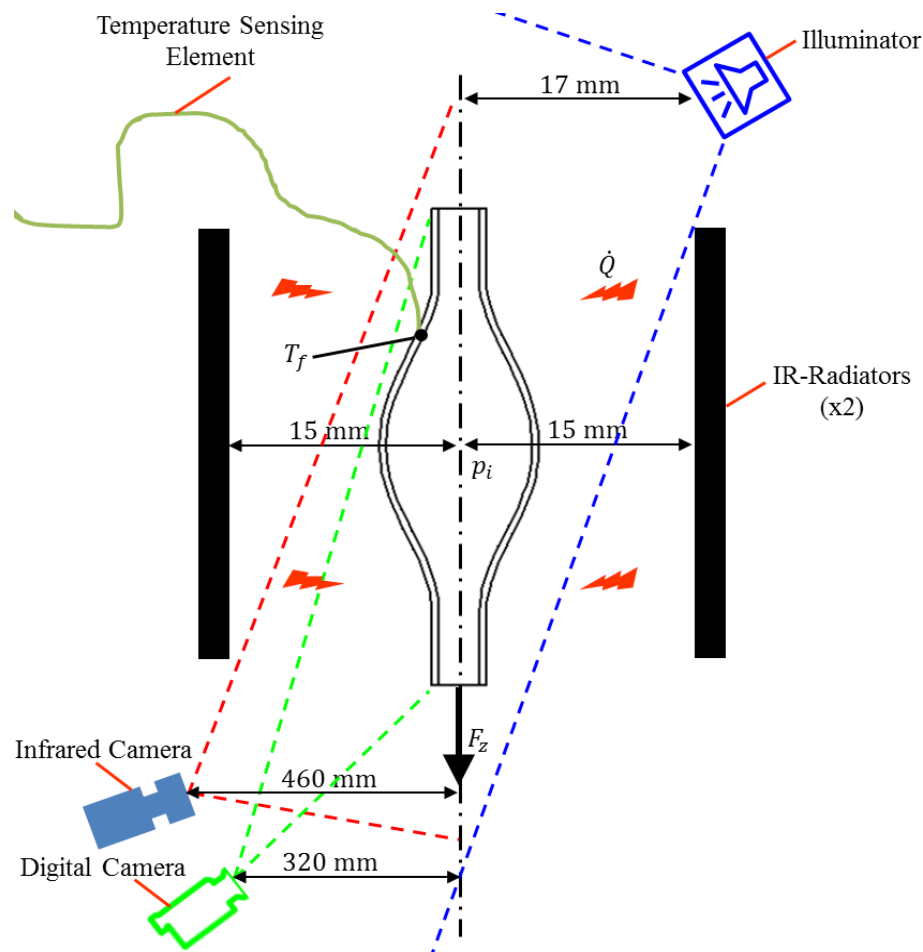


Figure 41 Schema of the Experimental Method for the Free Forming of the Micro Tubes

In Figure 41, \dot{Q} represents heating rate of the micro tube by the IR-radiators heat source. The tensile force F_z shown in Figure 41 was determined in the initial stage of the study at different internal pressures p_i . The suitability for the free blowing of the polymeric micro tubes was also investigated. This approach enabled the variation and investigations of the blow forming rate and the interrelation with F_z in the experiments conducted.

For the systematic study of the effects of the strain rate at the working loads of internal pressure p_i and the tensile force F_z as well as the working temperature T_f , an experimental plan was developed for the process cycle time and listed in Table 6. The applied initial internal pressure p_i was 1 bar and increased at 0.5 bar interval. Visible deformation was not observed for internal pressure p_i below 1 bar. Maximum internal pressures p_{imax} from 1 to 6 bar were applied to the different Process Controls namely: Prog_01 and Prog_02 listed in Table 6 respectively. This enabled the study of different strain rate effects in the formability investigations. The tensile force F_z , and the working temperature T_f , were not varied in the different experiments conducted.

Table 6 Experimental Plan to Investigate Formability of the Micro Tubes

Tube materials: PET1, PET134 and PA 6				
Dimensions [mm]: d_{a0} 1.02-1.34 and s_0 0.125-0.170				
Tube section length L_0 [mm]: 45				
Applied internal pressures p_i [bar]: 1-6				
Working temperature T_f [°C]: 93 (3 % standard deviation)				
Tensile force F_z [N]: 0.12				
Sealing force F_s [N]: 200				
Process	t_1	t_2	t_3	t_4
Control	[ms]	[ms]	[ms]	[ms]
Prog_01	1	1	1	120000
Prog_02	2000	2000	2000	96000

To quantify the formability of the micro tubes in the experiments, the evaluated values of d_{at} , d_{rt} and d_{zt} were used. The values were acquired through the digital image correlation technique applied in the experiments. The definitions of the values are illustrated in Figure 42.

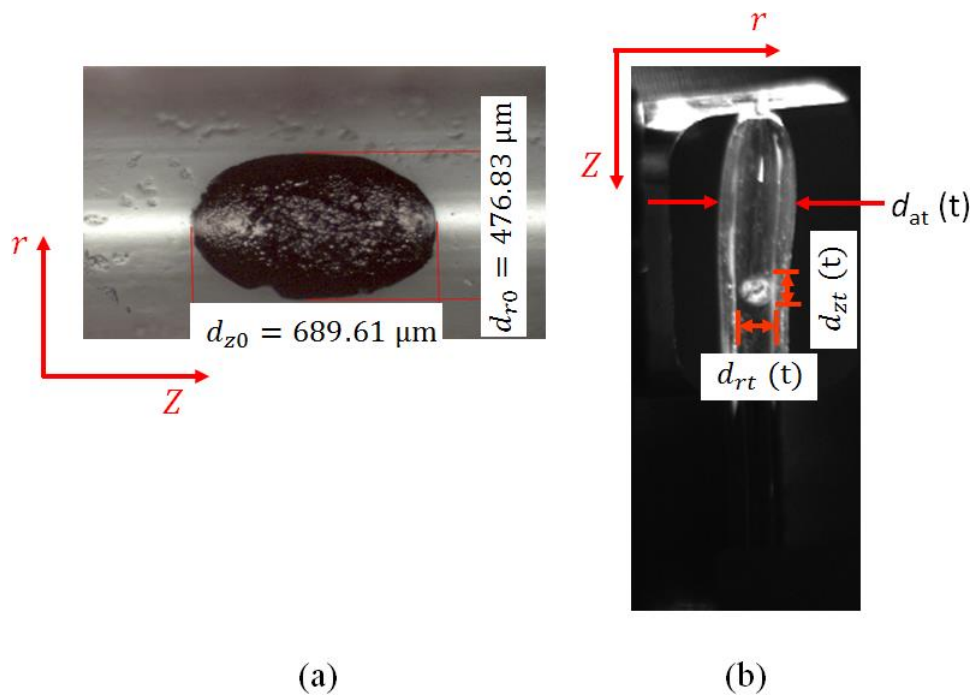


Figure 42 Digital Image Correlation Technique in the Free Forming Experiments: (a) Initial Dimensions of the Tagged Measuring Point; d_{r0} Dimension in the Hoop Direction and d_{z0} Dimension in the Axial Direction (b) Dimensions at Time t

In Figure 42 (b), d_{at} represents the instantaneous outer diameter at time t . The d_{rt} represents the instantaneous value of the measuring point in the r -direction or radial (hoop) direction at time t , while d_{zt} is the instantaneous value of the measuring point in the Z -direction or axial direction at time t .

In the evaluation and processing of the recorded values, the d_{at} value proved to be most reliable and was used to define the stretch ratio λ at time t as in Equation 52:

$$\lambda(t) = \frac{d_{at}(t)}{d_{a0}} \quad (52)$$

Using d_{at} in Equation 52 to evaluate $\lambda(t)$ also limited the restrictions, which are currently associated with the optical measuring methods [136].

Applying Equation 52, the in-plane logarithmic strain fields as true strain relations [137] at time t can be estimated using the relations:

$$\varepsilon(t) = \ln(\lambda(t)) \quad (53)$$

Differentiating both sides of Equation 53 with respect to time t , gives the true strain rate for the free forming experiments at time t as in Equation 54:

$$\dot{\varepsilon}(t) = \frac{\dot{\lambda}(t)}{\lambda(t)} \quad (54)$$

where $\dot{\lambda}(t)$ is the stretch ratio rate at time t and defined by Equation 55 as:

$$\dot{\lambda}(t) = \frac{d\lambda(t)}{dt} \quad (55)$$

6.3 Results and Discussion

The results and discussions presented focused mainly on the PET1 micro tubes because the deviation in the dimensions of the PET micro tube semi-finished prototype were within the standard deviation limit given by the supplier. The standard deviation was also validated in Chapter 6.2.1 above. The deviation in the PET134 micro tubes dimensions observed were above the 0.03 standard deviation for the PET1 micro tubes. Standard deviation of 0.03 is significant in micro manufacturing and influenced the conduct and the results of the experiments. The experiments with PET134 micro tube materials were however used to investigate size effects in the formability of PET micro tubes. The experiments with PA 6 micro tube materials enabled the comparison of formability for the different polymeric micro tube. There was no deviation in the dimensions of the PA 6 micro tubes investigated.

Experiment: $p_{imax} = 1$ bar and Process Control Prog_01. Tube Material: PET1

The free forming experiment result shown in Figure 43 was collected for PET1 material tubes with dimensions: $d_{a0} = 1.02$ mm, $s_0 = 0.125$ mm, $L_0 = 45$ mm and at the working temperature T_f of 93 °C. A maximum internal pressure $p_{imax} = 1$ bar was applied and tensile force F_z was set at 0.12 N, in the experiment. The process control Prog_01 was applied.

Figure 43 illustrates the development of the stretch ratio λ and the applied maximum internal pressure p_i as functions of the forming time t . The superimposed tensile force F_z illustrated in the free forming experiment schema above was constant at 0.12 N in the experiments.

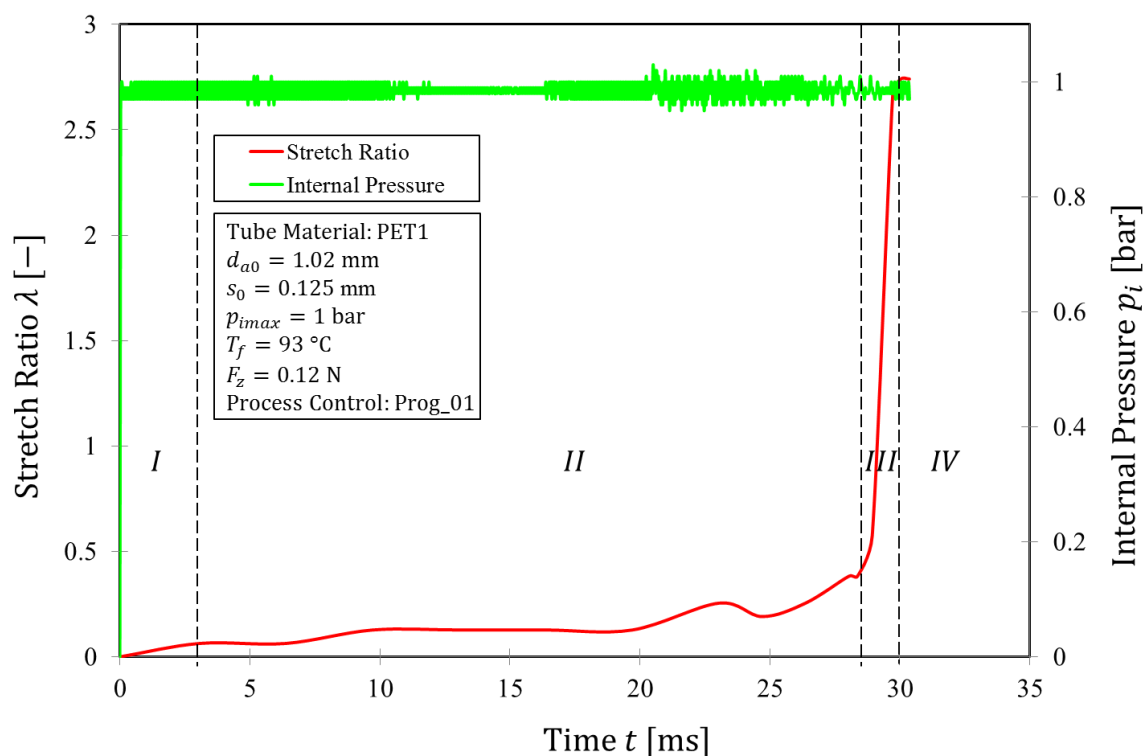
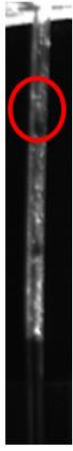
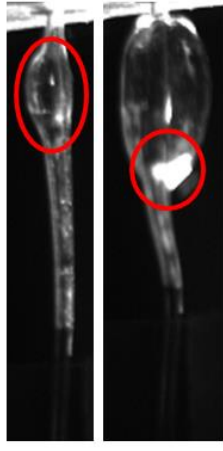
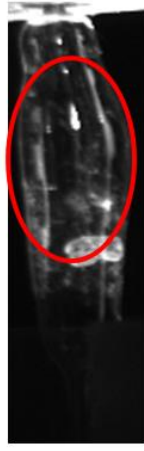
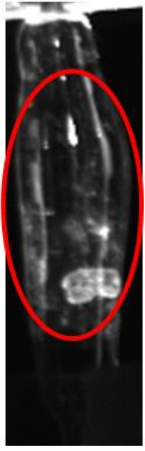


Figure 43 Stretch Ratio λ and the Maximum Internal Pressure p_{imax} versus Time t development for PET1 Tube Material: $p_{imax} = 1$ bar, Process Control Prog_01

In Figure 43, the relationships among the stretch ratio λ , internal pressure p_i and time t curve measured at the working temperature T_f of 93 °C can be divided into four Zones I-IV.

Collected in Table 7 below are images, instabilities and the failure mode associated with the Zones during the *in situ* deformation of the PET1 tube material illustrated in Figure 43 above.

Table 7 Zones illustrated in Figure 43 with associated Images, Instabilities and Failure Mode

Tube materials: PET1 Dimensions [mm]: d_{a0} 1.02 and s_0 0.125 Applied maximum internal pressure p_i [bar]: 1 Process Control: Prog_01 Working Temperature T_f [°C]: 93 (standard deviation 3 %) Tensile force F_z [N]: 0.12 Sealing force F_s [N]: 200				
Zones	I	II	III	IV
Images				
Instabilities	Necking	Strain softening Necking	Strain Softening	Strain Softening
Failure Mode				Failure free

Zone I ($\lambda = 0 - 1 \%$) is a necking zone and corresponds to the onset of crystallization [57], which can be attributed to the micro tube processing history and superimposed F_z [97]. The dominant load F_z in this zone promoted more efficient tensile orientation of chains and the tensile axis alignment, which resulted in the increase of internal pressure p_i required to deform the polymer micro tube in the radial direction and explain the initial hardening which progressed in Zone II. The necking resulted from the dominant tensile load due to superimposed F_z .

Zone II ($\lambda = 1 - 4 \%$) is a region of apparently strain hardening with strain softening instability. The strain softening however was stabilized through increased orientation hardening as forming progressed [57, 78 and 84]. In this Zone, the resistance to an incremental deformation decreases as the strain in the micro tube increases into Zone III, where steep deformation occurred. Obvious in Zone II shown through the image in Table PET1, local straining occurred, which resulted in the local deformation (tube bulging) rather than homogeneous deformation.

Zone III ($\lambda = 4 - 260 \%$) shows strain softening behaviour in the forming process, where the resistance to an incremental deformation decreases as the strain in the micro

tube increases rapidly [57]. An average maximum stretch ratio λ_{max} of 2.6 was recorded in the radial (hoop) direction. Since strain softening is an intrinsic property of most polymers [57, 84], the strain softening instability might not have been avoided by any experimental method.

The final stage is Zone IV ($\lambda = 260 - 270 \%$), where the development of the crystalline phase becomes dominant but at a relatively reduced rate. In Zone IV defined in this study as the relaxation period, is the regime when the material in the micro tube is fully aligned and the deformation limit rapidly reached at approximately maximum stretch ratio λ_{max} of 2.7 for the result shown in this Figure. The relaxation period was implemented in the control process to quantify the forming limit of micro tubes at the applied p_{imax} .

Experiment: $p_{imax} = 2.5$ bar and Process Control Prog_01. Tube Material: PET1

Shown in Figure 44 are the development of stretch ratio λ_{max} and the applied maximum internal pressure p_{imax} of 2.5 bar versus the forming time t also with the process control Prog_01. All other process conditions were similar to the result presented in Figure 44.

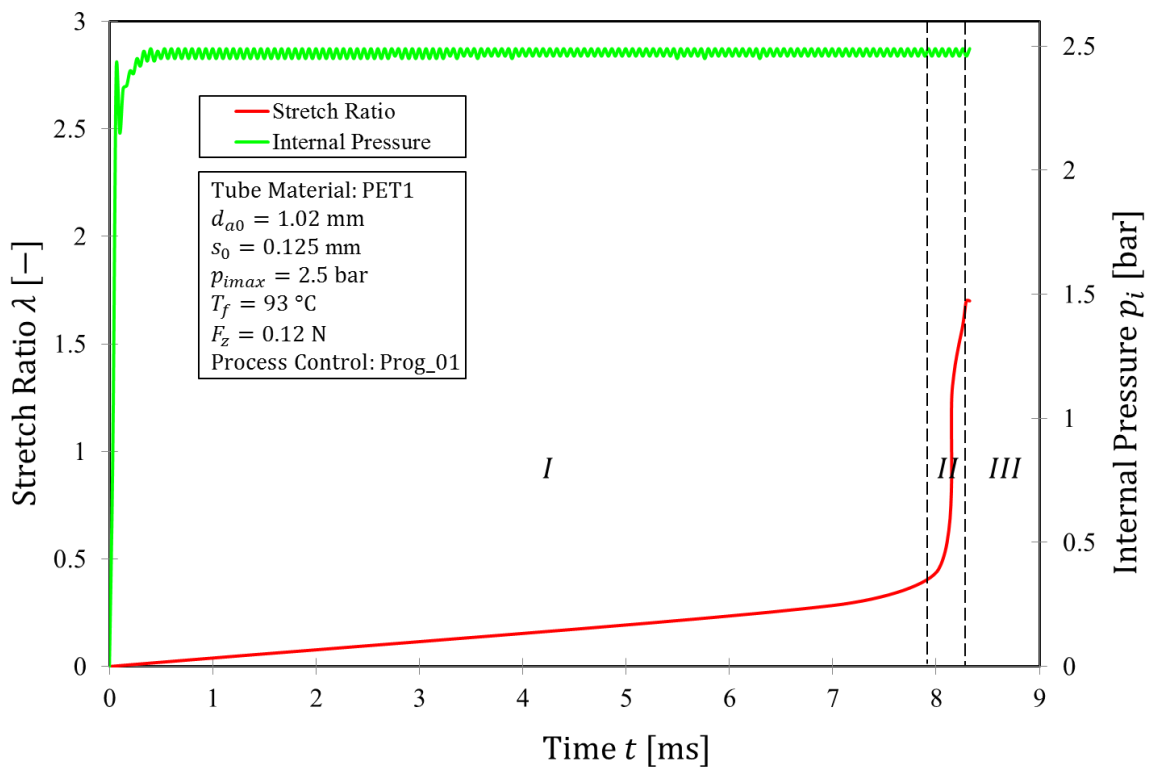
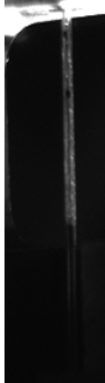
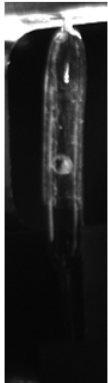
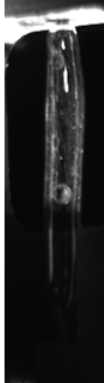


Figure 44 Stretch Ratio λ and the Maximum Internal Pressure p_{imax} versus Time t development for PET1 Tube Material: $p_{imax} = 2.5$ bar, Process Control Prog_01

Listed in Table 8 are images, instabilities and the failure mode associated with the Zones during the *in situ* deformation of the PET1 tube material as illustrated in Figure 44 above.

Table 8 Zones illustrated in Figure 44 with associated Images, Instabilities and Failure Mode

Tube materials: PET1 Dimensions [mm]: d_{a0} 1.02 and s_0 0.125 Applied maximum internal pressure p_i [bar]: 2.5 Process Control: Prog_01 Working Temperature T_f [°C]: 93 (standard deviation 3 %) Tensile force F_z [N]: 0.12 Sealing force F_s [N]: 200			
Zones	I	II	III
Images			
Instabilities	Necking free	Strain softening free Necking free	Strain Softening free
Failure Mode			Failure free

This experiment produced failure free results at the relaxation period, which corresponds to Zone III of the forming process.

Experiment: $p_{imax} = 3$ bar and Process Control Prog_01. Tube Material: PET1

Presented in Figure 45 are the development of stretch ratio λ_{max} and the applied maximum internal pressure p_i of 3 bar versus the forming time t for the process control Prog_01. This Figure is comparable with the experimental result shown in Figure 44. The experimental method here was also similar to the above results.

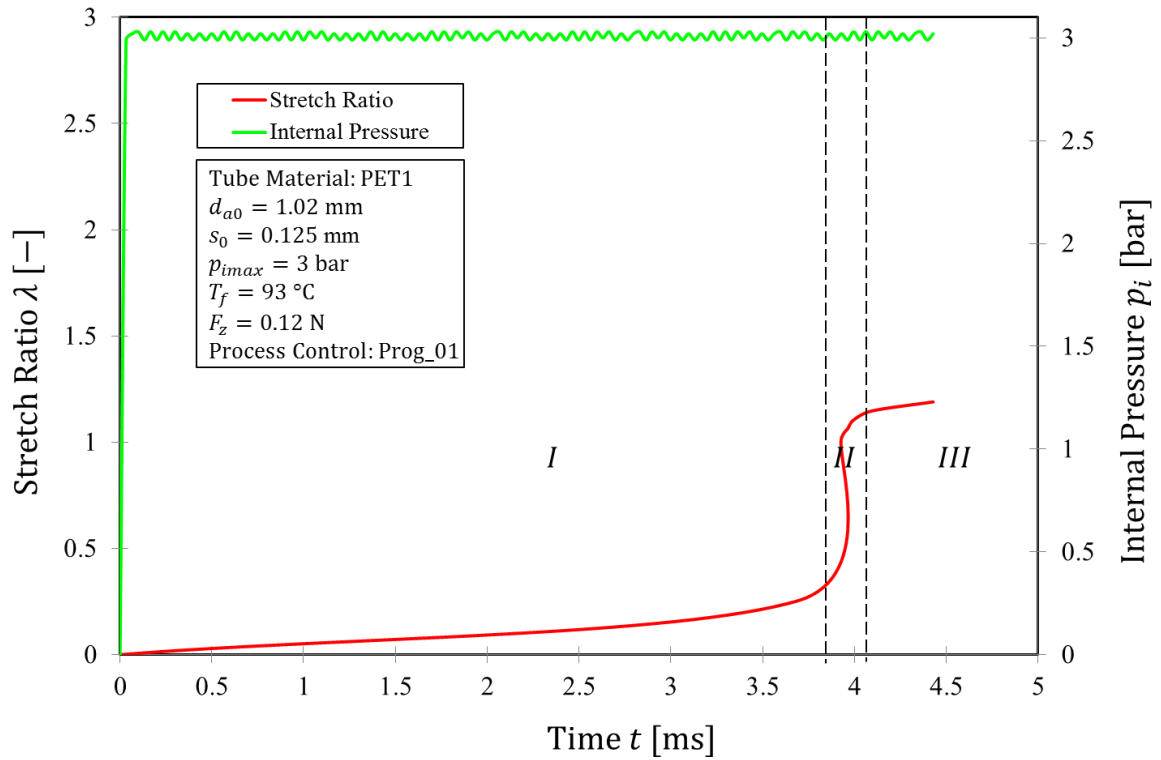
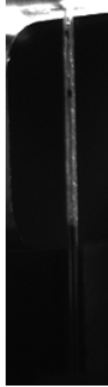
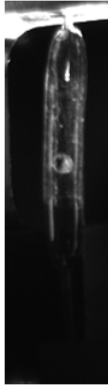
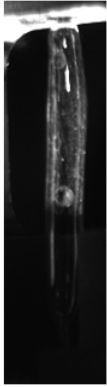


Figure 45 Stretch Ratio λ and Maximum Internal Pressure p_{imax} versus Time t development for PET1 Tube Material: $p_{imax} = 3$ bar, Process Control Prog_01

The images, instabilities and the failure mode associated with the Zones during the *in situ* deformation of the PET1 tube material as illustrated in Figure 45 above are listed in Table 9.

Table 9 Zones illustrated in Figure 45 with associated Images, Instabilities and Failure Mode

Tube materials: PET1 Dimensions [mm]: d_{a0} 1.02 and s_0 0.125 Applied maximum internal pressure p_i [bar]: 3 Process Control: Prog_01 Working Temperature T_f [°C]: 93 (standard deviation 3 %) Tensile force F_z [N]: 0.12 Sealing force F_s [N]: 200			
Zones	I	II	III
Images			
Instabilities	Necking free	Strain softening free Necking free	Strain Softening free
Failure Mode			Failure free

The results in this experiment also produced failure free formed parts at the relaxation period. The instabilities were within acceptable limit, hence qualified as instabilities free process. Necking and strain softening instabilities can be observed in Zone II of Figure 45.

Experiment: $p_{imax} = 6$ bar and Process Control Prog_02. Tube Material: PET1

Figure 46 illustrates the development of stretch ratio λ_{max} and the applied maximum internal pressure p_i of 6 bar versus the forming time t for the process control Prog_02.

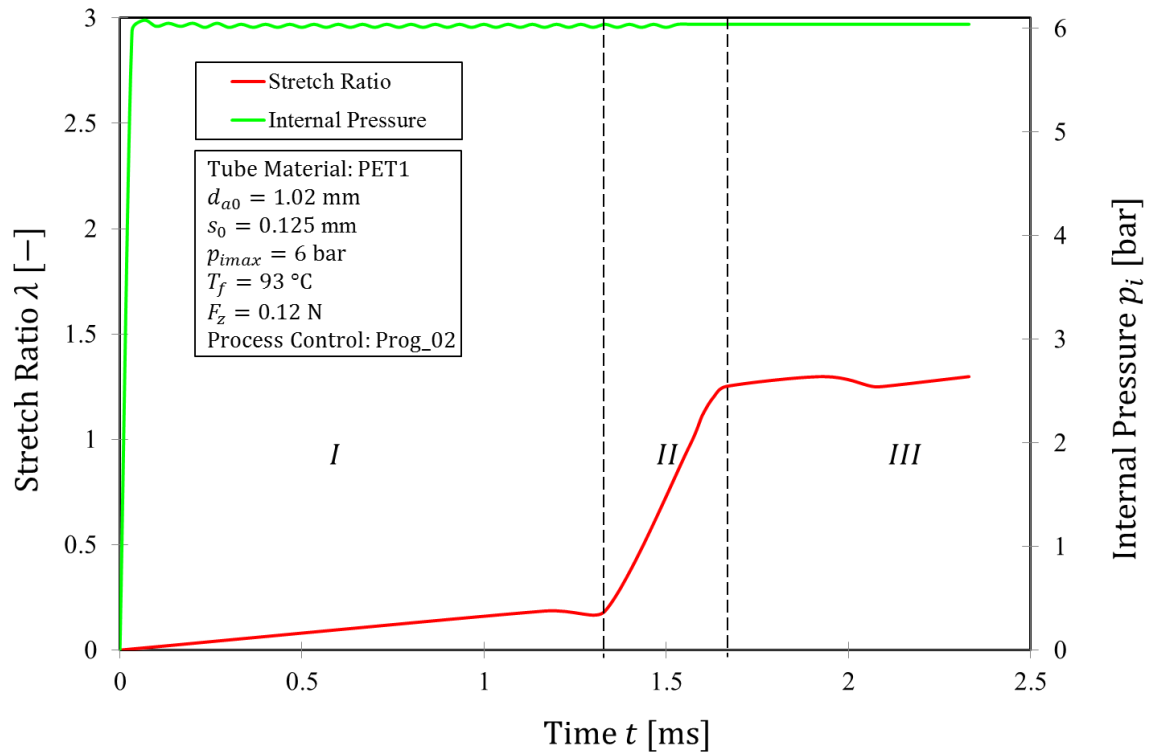
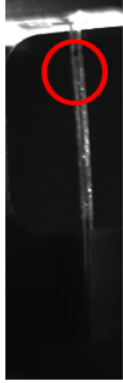
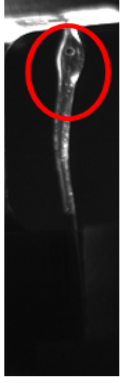
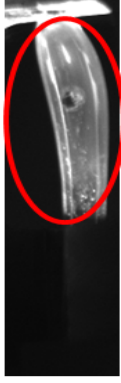


Figure 46 Stretch Ratio λ and Internal Pressure p_{imax} versus Time t development for PET1 Tube Material: $p_{imax} = 6$ bar, Process Control Prog_02

Listed in Table 10 are images, instabilities and the failure mode associated with the Zones also during the *in situ* deformation of the PET1 tube material illustrated in Figure 46.

Table 10 Zones illustrated in Figure 46 with associated Images, Instabilities and Failure Mode

Tube materials: PET1 Dimensions [mm]: d_{a0} 1.02 and s_0 0.125 Applied maximum internal pressure p_i [bar]: 6 Process Control: Prog_02 Working Temperature T_f [°C]: 93 (standard deviation 3 %) Tensile force F_z [N]: 0.12 Sealing force F_s [N]: 200			
Zones	I	II	III
Images			
Instabilities	Necking	Strain softening Necking	Strain softening
Failure Mode			Bursting

The results from this experiment were associated with instabilities as shown on the images in the different Zones in Table 10 and the curve in Figure 46. A bursting failure mode was recorded at the initiation of the relaxation period in Zone III. Bursting failure is a ductile failure mode compared to crazing failure mode. These are discussed in Chapter 6.4 below.

Results presented in Figures 44 to 46 and Tables 8 to 10 indicated that the deformation developments can be categorized into three Zones, designated as I, II and III against the four Zones observed in the experiment with maximum internal pressure $p_{imax} = 1$ bar. In Zone I of these experiments, the orientation hardening is induced by strain, where the applied internal pressure increased to the maximum internal pressure $p_{imax} = 2.5, 3$ and 6 bar respectively and remained about constant. In Zone II, crystallization is initiated marking the beginning of the strain hardening region. The initial rapid orientation hardening behaviour observed on the curves in Figures 44 to 46 prevented any possible strain softening, which appears to be given only by crystalline polymers or fibre-forming glassy polymers which crystallise on drawing as with PET materials [57, 58]. Strain softening and necking instabilities observed in Figure 46 as the deformation progress from Zone I to Zone II influenced the range of the Zone II compared to the other experimental results.

In Zone III, the deformation process is facilitated by strain induced orientation until the failure of the micro tube in the case with maximum internal pressure $p_{imax} = 6$ bar. The stretch ratio and internal pressure remain about constant in Zone III.

When crazing failure did not occur in the experiments with the tube material PET134, the experimental results with the tube material were failure free in the relaxation period for the different process controls used by applying maximum internal pressure $4 \leq p_{imax} < 4.5$ bar. The difference in the applied maximum internal pressure p_{imax} to the achieve failure free forming of the PET1 and PET134 micro tubes can be associated with the different dimensions of the micro tubes. However, other factors or combination of factors such as stresses and adiabatic heating development under the experimental conditions can equally be associated with the observation. The precise causes of the failure will be subject of further investigation.

Free-Forming Experiments: Evolution of the True Strain Rates $\dot{\epsilon}$. Tube Material: PET1

In Figure 47 the evolution of the true strain rate $\dot{\epsilon}$ as function of the stretch ratio for the free-forming of PET1 materials is shown for the different experiments.

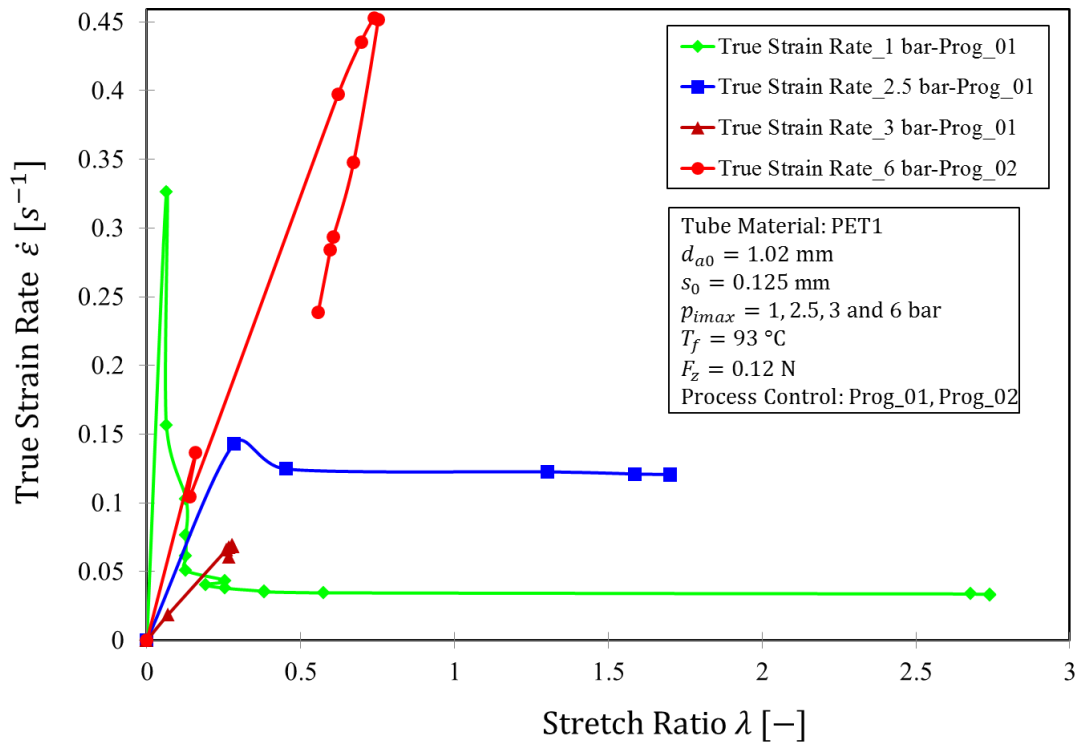


Figure 47 Comparison of the True Strain Rates $\dot{\epsilon}$ versus Stretch Ratio λ for the different Experiments

The experiment: $p_{imax} = 6$ bar and process control Prog_02 produced the highest strain rate of 0.239 s⁻¹ and minimum forming time of 2.331 ms. High strain rate $\dot{\epsilon}$ caused strong orientation hardening, which affected the achievable maximum stretch ratio λ_{max} . As expected and shown in Figure 47, experiments with the maximum true strain rates produced the least maximum stretch ratio λ_{max} .

Collected in Table 11 are the maximum stretch ratio λ_{max} , maximum strain rate $\dot{\epsilon}_{max}$ and the approximate total forming time t_o recorded in the experiments.

Table 11 Comparison of the different Experimental Results for Tube Material PET1

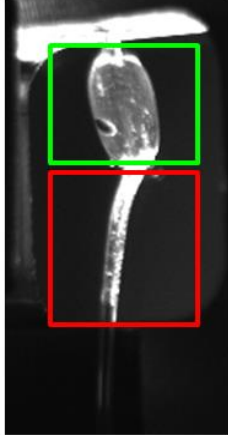

Tube materials: PET1 Dimensions [mm]: d_{a0} 1.02 and s_0 0.125 Applied internal pressures p_i [bar]: 1-6 Working Temperature T_f [°C]: 93 (standard deviation 3 %) Tensile force F_z [N]: 0.12 Sealing force F_s [N]: 200						
Experiment Nr.	Process Control	Maximum Internal Pressure p_{imax} [bar]	Approximate Total Forming Time t_o [ms]	Maximum Stretch Ratio λ_{max} [-]	Maximum True Strain Rate $\dot{\epsilon}_{max}$ [s^{-1}]	Failure Mode
01	Prog Nr_01	1	30.370	2.74	0.033	Failure free
02	Prog Nr_01	2.5	8.325	1.70	0.120	Failure free
03	Prog Nr_01	3	4.429	1.19	0.061	Failure free
04	Prog Nr_02	6	2.331	1.30	0.239	Bursting

For the achieved maximum true strain $\dot{\epsilon}_{max} = 0.239 s^{-1}$, a maximum stretch ratio λ_{max} of 1.30 was recorded in the experiment with $p_{imax} = 6$ bar and Process control: Prog_02 as against the maximum stretch ratio λ_{max} of 1.19 recorded in the experiment with lower maximum true strain $\dot{\epsilon}_{max} = 0.061 s^{-1}$ for the experiment: $p_{imax} = 3$ bar and Process control: Prog_01. This can be attributed to the different levels of necking and strain softening instabilities recorded in the experiments. The precise quantification of the influences of the instabilities will be subject of further investigations.

A linear relationship between approximate forming time t_o and true strain rate $\dot{\epsilon}_{max}$ with different experiments can be observed. Both values are critical to the manufacturing time and the properties of the manufactured parts. More experiments are also required to establish the precise relationship.

Although tensile force F_z was applied as constant in the experiments, the effect of the tensile force F_z on the formability of the micro tubes in forming method applied in this study is collected in Table 12.

Table 12 Tensile Force F_z Effects on the Formability of PET1 Tube Material at
 $p_{imax} = 4$ bar

Tube materials: PET1 Dimensions [mm]: d_{a0} 1.02 and s_0 0.125 Applied maximum internal pressure p_i [bar]: 4 Process Control: Prog_02 Working Temperature T_f [°C]: 93 (standard deviation 3 %) Sealing force F_s [N]: 200		
Tensile force F_z [N]	0.0	0.12
Images		
λ_{max}	localized	homogenous
Formability Limit	not achievable	achievable

In the experiment with $F_z = 0$, the image illustrates a localized deformation. In the case of $F_z = 0.12$ N, a homogenous deformation is observed, which propagates along the whole micro tube due the strain orientation induced by F_z . Localised deformation observed by $F_z = 0$ can be attributed to the absence of the initiation for strain orientation.

Quantifying the effects of the tensile force F_z ; for $F_z = 0.12$ N, the achievable maximum stretch ratio λ_{max} , was 1.80 compared to the achievable local maximum stretch ratio λ_{max} of 1.10 in the experiment: $F_z = 0$. These results illustrate the significant of the tensile force F_z in the blow forming of polymeric micro tubes.

6.4 Failures Classification in Free-Formed of Polymeric Micro Tubes

In Chapter 6.3 the experimental results discussions were focused on the relationship between the process configuration and their influence on the formability of polymeric micro tubes. In this Chapter the intent is to classify the failures recorded in the experiments. In the failure classification, the emphasis is on the applications to the manufacture of polymeric hollow micro components against the causes of failure and to define the causes and effects of failure.

Failures are most often related to large deformations, plastic strains in metals, and irreversible strains in polymers. They can occur during forming processes and are always associated with instabilities and the phenomenon of localization of strains and damage [138].

Several physical deformation mechanisms most often lead to polymer failure. These mechanisms involve large scale irreversible molecular changes with the most common optically visible result of crazing or shear banding [14] as well as ductile (shear) failure observed in bursting failure mode.

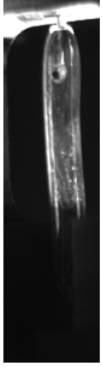
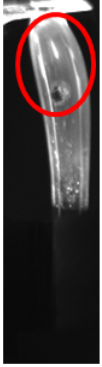

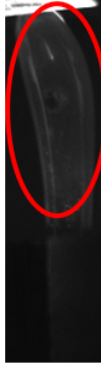
Crazes are micro cracks that occur due to the formation of micro voids at points of high stress concentration such as surface scratches or micro cracks as was the case with the PET micro tubes used in the experiments. The voiding involved in the crazing permits the material to achieve plastic strain faster. Hence, the surface scratches and micro cracks on the micro tubes observed during tube material preparation for the experiments, under the tensile load F_z favoured the initiation of crazing. These defects are points of high concentration of stresses and can cause the formation of initial micro voids [22, 84] and brittle failure. Crazes may equally well develop due to regions of elastic inhomogeneity within the material [84].

The two main failures recorded in the free forming experiments of the PET micro tubes are crazing and ductile (shear) failures.

Homogeneous Ductile Failure in PET1 Tube Material

In Table 13 is the collected ductile failure development recorded in the experiment with PET1 tube material at applied maximum internal pressure p_{imax} of 6 bar and process control Prog_02 due to strain softening instability

Table 13 Evolution of the Ductile Failure in PET1 Tube Material. Experiment: $p_{imax} = 6$ bar and Process Control Prog_02

Tube materials: PET1 Dimensions [mm]: d_{a0} 1.02 and s_0 0.125 Applied maximum internal pressure p_i [bar]: 6 Process Control: Prog_02 Working Temperature T_f [°C]: 93 (standard deviation 3 %) Tensile force F_z [N]: 0.12 Sealing force F_s [N]: 200				
Stages	I	II	III	IV
Internal Pressure p_i [bar]	6	6	6	6
Images				
Instability Development	Before Strain Softening	Strain Softening Starts	Strain Softening Increases	Ductile Failure (Bursting)

This homogeneous ductile failure in the free forming experiment was recorded with the tube material PET1: $d_{a0} = 1.02$ mm and $s_0 = 0.125$ mm.

Instabilities and failures recorded in this experiment, were observed in other experiments with PET materials for applied maximum internal pressure $p_{imax} \geq 6$ bar, irrespective of the process control implemented. Due to deviation in the micro tube wall thickness at the actual forming time, the stress will be slightly higher at the point with minimum wall thickness and further deformation will concentrate at this point. The image in Stage III shows that the deformation increased at the start point of the strain softening as the local stress increased under continued application of the maximum internal pressure p_{imax} of 6 bar. The continued increase was due to insufficient strain hardening to suppress the instability, since the micro tube has reached the formability limit. At the formability limit quantified with maximum stretch ratio λ_{max} of approximately 2.74 for the PET1 tube material, further strain induced crystallization responsible for the strain hardening behaviour was not achievable to prevent the failure in Stage IV.

Crazing Failure in PET134 Tube Material

Illustrated in Figure 48 (a) is the schematic crazing and the nucleation of a crack within a craze and 48 (b) crazing failure recorded in the experiment with tube material PET134, at applied maximum internal pressure p_{imax} of 4 bar and process control Prog_02.

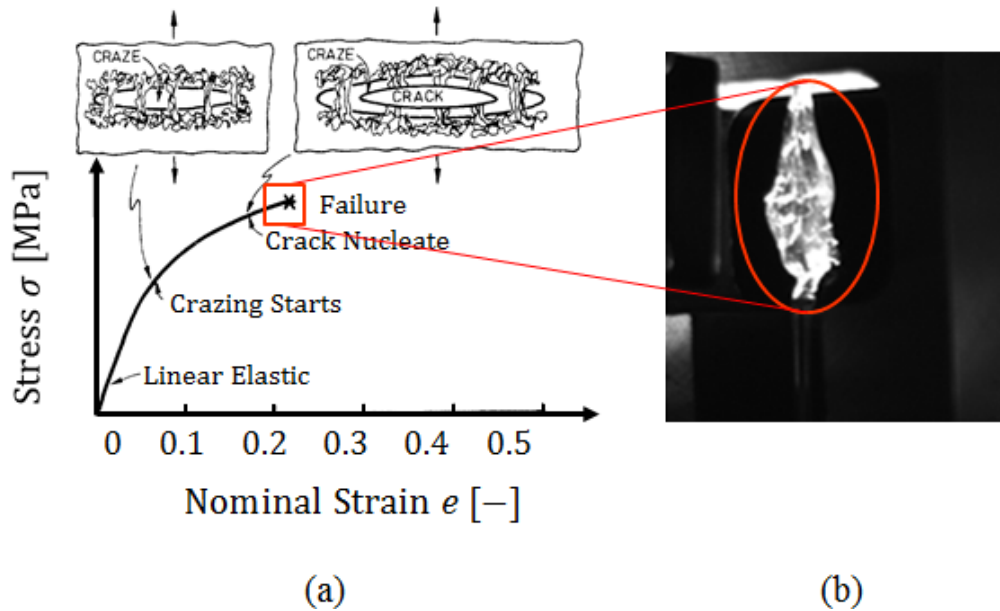


Figure 48 (a) Schematic Crazing Deformation Mechanism in Poly (methylmethacrylate) PMMA [143]. (b) Crazing Failure of PET134 Tube Material: $d_{a0} = 1.34$ mm and $s_0 = 1$ mm, $p_{imax} = 4$ bar and Process Control Prog_02

Crazes reflect light and have different refractive index. They scatter light and are readily visible even to the unaided eye as whitened planes perpendicular to the direction of stress [139]. When viewed with the light source equipped to the experimental equipment, the craze appears to have a silvery appearance much like a very fine crack as displayed in Figure 48 (b).

In the experiments conducted no crazing failure was recorded for PET1 tube materials. The crazing failure was mainly recorded for the PET134 micro tubes tested at applied maximum internal pressure $p_{imax} \geq 4$ bar. In the experiments conducted in this study, the ratio of the working temperature T_f 93 °C to the glass transition temperature T_g was approximately 1.2. The glass transition temperature T_g of PET tube material determined in the dynamic mechanical analysis (DMA) in Chapter 4 was between 72.3 and 83.3 °C and was independent of the micro tube dimensions. Hence, the free forming experiments were conducted at near $T_f > 1.2T_g$ for both PET tube materials. A stretch ratio λ of about 1.08 was recorded before the crazing failure.

Referring to the yield criteria reviewed in Chapter 4.3, the combination of tensile and biaxial stress produced crazing prior to shear yielding. Thus crazing failure in these experiments can only be related to the different PET material tube dimensions.

Localized Ductile Failure in PA 6 Tube Material

While craze deformation mechanism was recorded for the experiments with PET134 tubes and ductile failure at the micro tube forming limit for the PET1 tubes, the local failure depicted in Figure 49 for PA 6 micro tube was due to inadequate homogeneous working temperature T_f . Localised working temperature T_f attained for the PA 6 micro tube caused local softening and eventual local ductile (shear) failure under increasing stress due to the applied maximum internal pressure p_{imax} of 6 bar and the constant tensile force F_z .

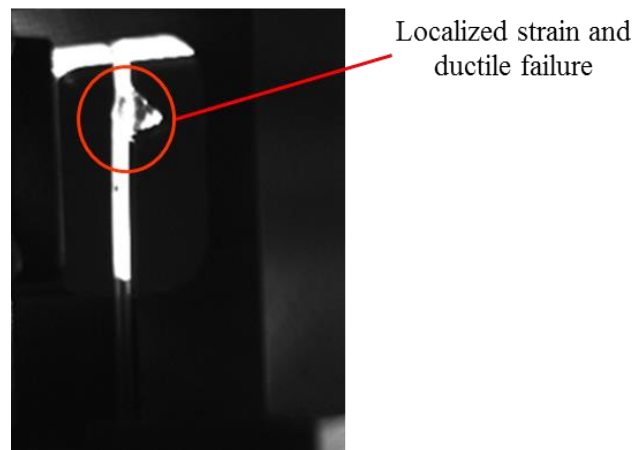


Figure 49 Local Ductile Failure in the Free Forming Experiment. Tube Material PA 6: $d_{a0} = 1.34$ mm and $s_0 = 1$ mm, $p_{imax} = 6$ bar and Process Control Prog_02

In Chapter 5 the measured glass transition temperature T_f for PA 6 tube materials in the DMA experiments was in the range from 35 to 59 °C. Glass transition temperature T_f in the range from 44 to 56 °C was collected for the PA 6 material from the literatures reviewed. These temperature ranges are below the achievable average uniform temperature of 93 °C provided by the heat source used in the experimental equipment.

The coefficient of heat transfer for PET and PA 6 are $0.29 \text{ Wm}^{-1}\text{K}^{-1}$ [9, 108-114]. The specific heat capacity c_p for the PET and the PA 6 tube materials are however different. The respective specific heat capacities c_p for the materials are: PET $1150 \text{ JKg}^{-1}\text{K}^{-1}$ and PA 6 $1700 \text{ JKg}^{-1}\text{K}^{-1}$ [99, 108-114]. Specific heat capacity c_p is the energy required to raise the temperature of a unit mass of a substance by one degree. For equal forming time t_o with PET tube material, PA 6 tube materials will require higher working temperature T_f . The appropriate working temperature T_f for the PA 6 tube material at short forming time t_o will be further investigated, since process time reduction in the manufacture of micro parts is important and one of the objectives in this research work.

While crazing failure are much associated with the material been processed, ductile failures are influenced mostly by the processing conditions as shown in the ductile failure for the PET1 materials and PA 6 tube materials. To avoid ductile or burst failure, accurate prediction of the initiation is an important factor in the design and manufacture of the blow formed parts. The prediction of ductile failure in the forming of polymer micro tubes was addressed in Chapter 8.

7. Calibration of a Constitutive Model

7.1 Introduction

In the fundamental macro mechanical theories [80], large, time dependent inelastic deformations such as viscoplastic behaviour are based on the criteria of a yield surface or yield function giving the yield condition hardening rules. The hardening rules determine the change of the yield surface during deformations and on the relation of the stresses σ_f and plastic strains ε^p relations of materials in a multiaxial deformation as described in Chapter 4. These relations are used to formulate constitutive models to quantify materials responses during plastic deformations. The flow stress σ_f characterize the formability of the material and measure stresses, which lead to the plastic flow during deformations. The σ_f depend on the previous strains ε^p of a material, actual strain rate, and finally the temperature T [80].

The aim of this chapter is therefore to develop a simple and manufacturing oriented constitutive model for blow forming of polymeric hollow parts. Since, there is no completely general model that describes all the features in a deformation process, in many application, only relevant aspect of material behaviours are represented in a constitutive model to accurately characterize the behaviour [71].

In this study, constitutive parameters of the model were determined from the experimental data, which are published in [51].

7.2 Material Flow Stress Law

Thermoplastic polymers can be modelled through several approaches, using elasto-plastic, hyperelastic, viscoelastic and viscoplastic mathematical equations [12-15, 57-79]. Over several years different constitutive models were developed as discussed in Chapter 4.

Processing Polymers at elevated temperatures can be represented by a viscoplastic constitutive equations or model. Viscoplastic behaviour has been observed in experiments with thermoplastic polymers [51]. It involves strong strain rate effect and significant strain hardening, which are temperature dependent.

Predominant constitutive models representing viscoplastic behaviour use σ_f as a basis for the estimation of forming variables such as F_z and p_i , but also local variables such as stress, strain and temperature. To represent equivalent stresses σ_f in this study, the Hensel-Spittel model was used as the basis for the constitutive model given in Equation 56 [140, 141]:

$$\sigma_f = A_f \exp(m_1 T) \varepsilon^{m_2} \exp\left(\frac{m_4}{\varepsilon}\right) (1 + \varepsilon)^{m_5 T} \exp(m_7 \varepsilon) \dot{\varepsilon}^{m_8 T} \quad (56)$$

Hensel-Spittel model enables through the regression analyses the determination of the coefficients $m_1 - m_8$. The coefficients take into account individual effects, such as, the hardening behaviour of the material during the forming process. At an elevated forming temperature, the constitutive model of metallic materials is sufficiently accurately described with the parameters $m_1 - m_4$ in Equation 57, hence the model in Equation 56 thereby reduces to [141, 142]:

$$\sigma_f = A_f \exp(m_1 T) \varepsilon^{m_2} \dot{\varepsilon}^{m_3} \exp(m_4 \varepsilon) \quad (57)$$

where A_f is a constant factor, m_1 characterises the dependence on the process temperature T , m_2 characterises the hardening behaviour of materials, m_3 characterises the dependence on the equivalent strain rate and m_4 characterise the dependence on the equivalent (effective) strain.

Equation 57 contains only five fitting parameters namely: $m_1 - m_4$ and A_f . The parameters are determined by standard optimization techniques such as linear regression used in this study. The measured physical properties and quantities: temperature T , superimposed tensile force F_z and pressure p_i , which determine the variables: ε , $\dot{\varepsilon}$ and T in Equation 57 were considered in the application of empirical mathematical equation in the Hensel-Spittel model for this fundamental research work.

7.3 Constitutive Model Parameter Identification

Constitutive models are mostly fitted to experimental measurements or data, despite efforts at theoretical solutions to constitutive models [71].

An identification of the material parameters associated with the material model in Equation 57 was conducted. In this study, a regression analysis approach was adopted to determine the material parameters from the biaxial experimental data in [51].

The biaxial experimental data used to evaluate the parameters in the linear regression analysis are given in [51]. The experimental data covered variety of the nominal strain rates: 0.2, 0.4, 0.8, 1, 2, 4, 8 and 16 s^{-1} in the temperature region from 81 to 116 °C for PET films material.

7.4 Calibrated Model

The values of the material parameters obtained from the regression analyses of the biaxial experimental data in [51] are collected in Table 14.

Table 14 Model Parameters obtained from the Regression Analyses of the Biaxial Experimental Data for PET Films in [51]

Material	Model Parameters Values				
	A_f	m_1	m_2	m_3	m_4
PET Films	1.5×10^{10}	-0.0578	0.44098	0.2747	0.00035398

Substituting the parameter values in Table 14 into Equation 57, Yield curves for the strain rates $\dot{\epsilon}$ between 0.0001 and 20 s^{-1} and strains up to 250 % at $T = 93 \text{ }^\circ\text{C}$ were developed and depicted in Figure 50.

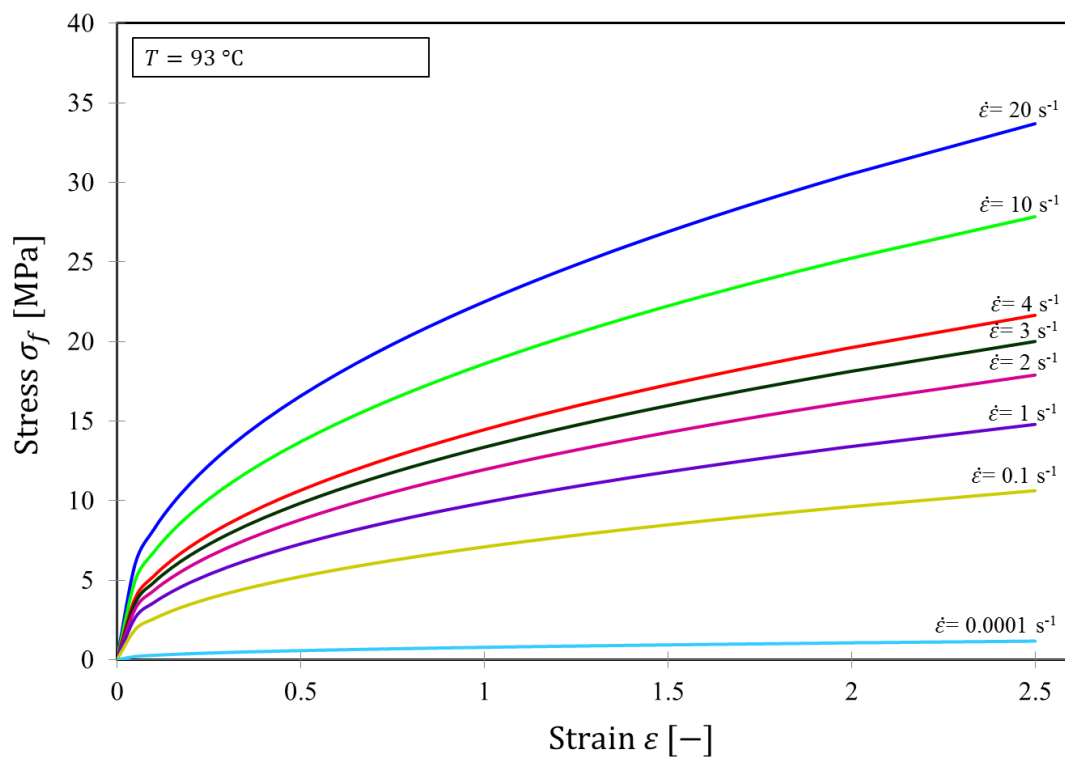


Figure 50 Yield Curves based on Equation 57 for different True Strain Rates $\dot{\epsilon}$ and at Constant $T = 93 \text{ }^\circ\text{C}$

This constitutive model was implemented into a commercial Finite Element program to predict in FE analyses, the free-forming experimental results presented in Chapters 6.

8. Prediction of Micro Tube Free Forming Process

8.1 Introduction

In order to evaluate the accuracy of the constitutive model above and its numerical implementation, FE analyses of the free forming experiments of the PET1 micro tubes were implemented in the commercially available Finite Element (FE) program ABAQUS/Explicit.

This FE program is a flexible general numerical solution procedure resource utilized to solve elastic-plastic and other nonlinear stress analysis problems under the action of loads or displacements that varies in a specific process respectively. A numerical solution procedure requires a constitutive model as in Equation 57 and Figure 51 in order to predict the induced stresses, strains and displacement under a complex state of stress [143].

The FE program has the capability of incorporating the constitutive model described above as well as user defined subroutines [143]. In the FE-analyses presented in this Chapter, the model was imputed directly into this FE program to predict the formability the of polymer micro tubes.

An important step to predict forming of polymeric micro tubes reliably consists of the evaluation of the capacity of the developed constitutive models by comparing the results of the simulations analyses using the model with the experimental results.

In this Chapter, the verification of the constitutive model developed was conducted with the free-forming experimental results described in Chapter 6.

8.2 Numerical Modelling

Axisymmetric simulations were performed using explicit integration method to save computational cost. In the axisymmetric model shown in Figure 51, a displacement controlled modelling was chosen due to better stability limit and convergence compared to force or pressure controlled. The boundary conditions were chosen to realistic represent the experiments.

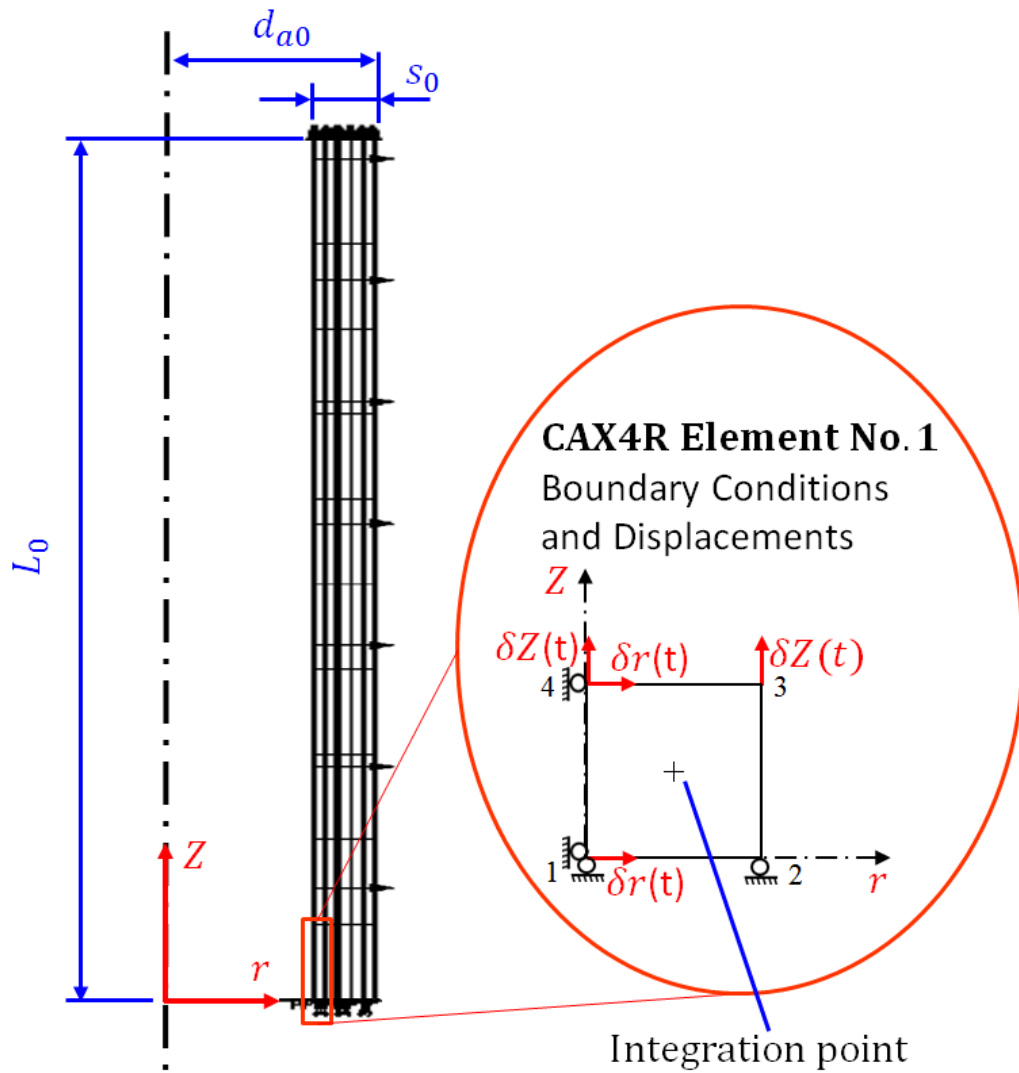


Figure 51 FE Analyses Model for the PET1 Micro Tube: $d_{a0} = 1.34$ mm and $s_0 = 1$ mm and $L_0 = 5$ mm

A Model length L_0 of 5 mm was chosen to reduce the analyses time. Analyses conducted with models between 5 and 45 mm produced the same results. The experimental tube length section L_0 was 45 mm. Listed in Table 15 are the PET material properties data required to fully define material behaviour for the explicit integration method (dynamic explicit) in the FE analyses.

Table 15 PET Material Elastic Behaviour Data for the FE Analyses. E-Module E for the range 90-100 °C [57, 99]

Tube material (Identifier)	Density ρ [Kg m ⁻³]	E-module E [MPa]	Poisson ratio ν
PET1	1370	15.3	0.39

Element Type

The element used for the analysis was CAX4R which is a 4-node bilinear axisymmetric quadrilateral, reduced integration solid element with hourglass control. For the analyses an approximate global element size of 0.0002 was used. Material response was evaluated at each integration point in each element illustrated in Figure 51 [143].

Boundary Conditions

As illustrated in Figure 51 with the inscribed Element No.1, the model boundary conditions prevented displacements in the Z – direction at the nodes 1 and 2. At the nodes 1 and 2 however, rotation and displacement in the r – direction were not prevented. The boundary conditions were used to define experimental conditions in the simulations analyses.

Loading

The model in the free forming simulations was loaded in a displacement controlled analyses. The displacement loadings in the FE-analyses was defined by the recorded experimental values of d_{at} described in Chapter 6 for the conducted experiments.

In the evaluation and processing of the recorded experimental values of d_{rt} , d_{zt} and d_{at} described in Chapter 6 to quantify the formability of the micro tubes, the d_{at} at the maximum point on the tube surface was chosen to estimate the stretch ratio λ at time t . This value provided most reliable evaluation results with the recorded image correlation technique and the physical measurement method carried-out.

Regular axisymmetric element used in the FE analyses allowed for only radial (r – direction), and axial (Z – direction) loading and has isotropic or orthotropic material properties in the principal directions. Hence, any radial displacement in such an element will induce a strain in the r – direction, which is the radial (hoop) strain and defined the stretch ratio λ used in the evaluation of the experimental results. Since the displacement must also be purely axisymmetric [143], the face corresponding to 1 and 4 was displaced in the positive radial direction as shown in Figure 51. Similarly, the face corresponding to 3 and 4 was displaced in the positive axial direction.

Solution Procedure

Solution procedure in the FE analyses applied to predict the respective experimental results are collected in Table 16.

Table 16 FE Analyses Solution Procedure for the PET1 Tube Material

Tube materials: PET1			
Dimensions [mm]: d_{a0} 1.02 and s_0 0.125			
Tensile force F_z [N]: 0.12			
Model length L_0 [mm]: 5			
Mass scale factor: 50			
Analysis procedure: Dynamic Explicit			
Free Forming Experiments	FE analyses Nr.	Number of Steps	Total Step Periods [s]
$p_{imax} = 1$ bar, Prog Nr_01	01	3	30.370
$p_{imax} = 2.5$ bar, Prog Nr_01	02	2	8.325
$p_{imax} = 3$ bar, Prog Nr_01	03	2	4.429
$p_{imax} = 6$ bar, Prog Nr_02	04	2	2.331

A mass scale factor of 50 was used for the FE analyses. The maximum displacements were limited to correspond to the experimental data. The kinetic energy was monitored to ensure that the ratio of kinetic energy to internal energy does not exceed 10 % as a measure of the analyses accuracy.

8.3 Results and Discussion

Figures 52-55 depict the FE analyses results of the free forming experiments aimed at verifying the capability of the constitutive model developed in Chapter 7 to predict the formability of polymeric micro tubes.

The stretch ratios λ in the FE analyses were evaluated from the displacement in the radial (hoop) direction, which is the r – direction as illustrated in Figure 51.

FE Analysis of the Experiment: $p_{imax} = 1$ bar and Process Control Prog_01. Tube Material: PET1

Shown in Figure 52 is the development of the stretch ratio λ versus the forming time t , in the FE analysis of the experiment conducted with maximum internal pressure $p_{imax} = 1$ bar and Process Control Prog_01 for PET1 tube materials.

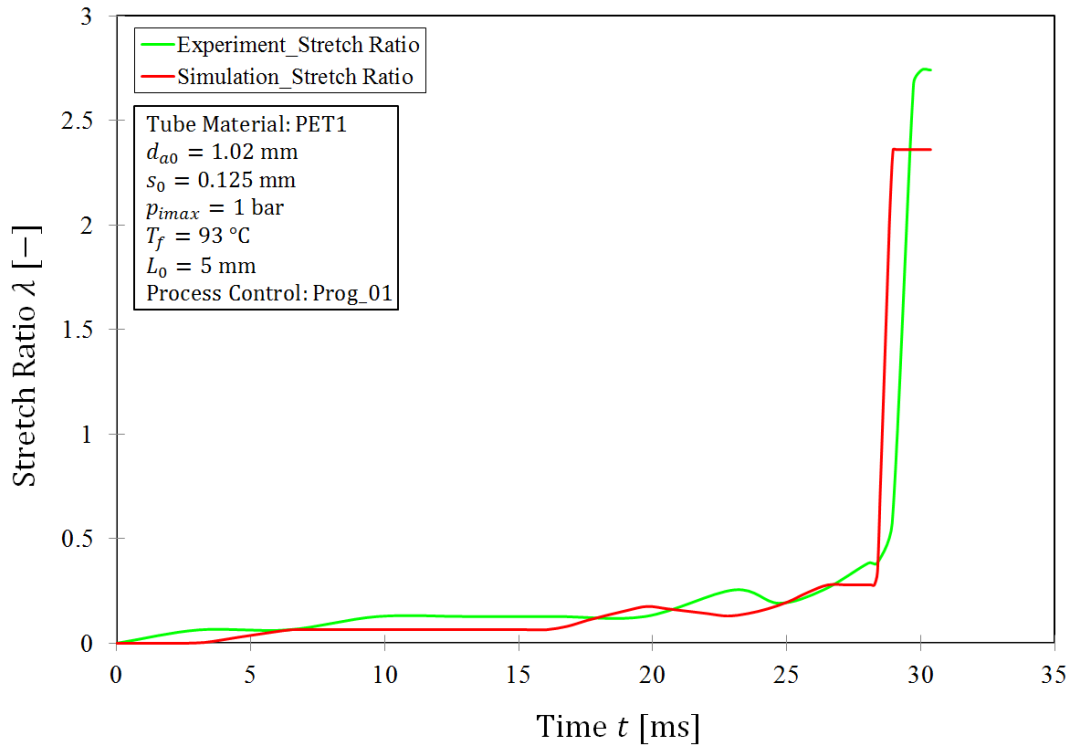


Figure 52 Stretch Ratio λ versus Time t development in the FE Analysis of the Experiment: $p_{imax} = 1$ bar and Process Control Prog_01. Tube Material: PET1

This Figure illustrates that the constitutive model performance is satisfactory. The FE analysis insensitivity to a possibly adiabatic heating in the experiment can be a factor in the small deviations in the simulated result. The model was developed to predict only the formability.

FE Analysis of the Experiment: $p_{imax} = 2.5$ bar and Process Control Prog_01. Tube Material: PET1

In Figure 53, the development of the stretch ratio λ as function of the forming time t in the FE analysis of the experiment: $p_{imax} = 2.5$ bar and Process Control Prog_01 for the PET1 tube material is shown.

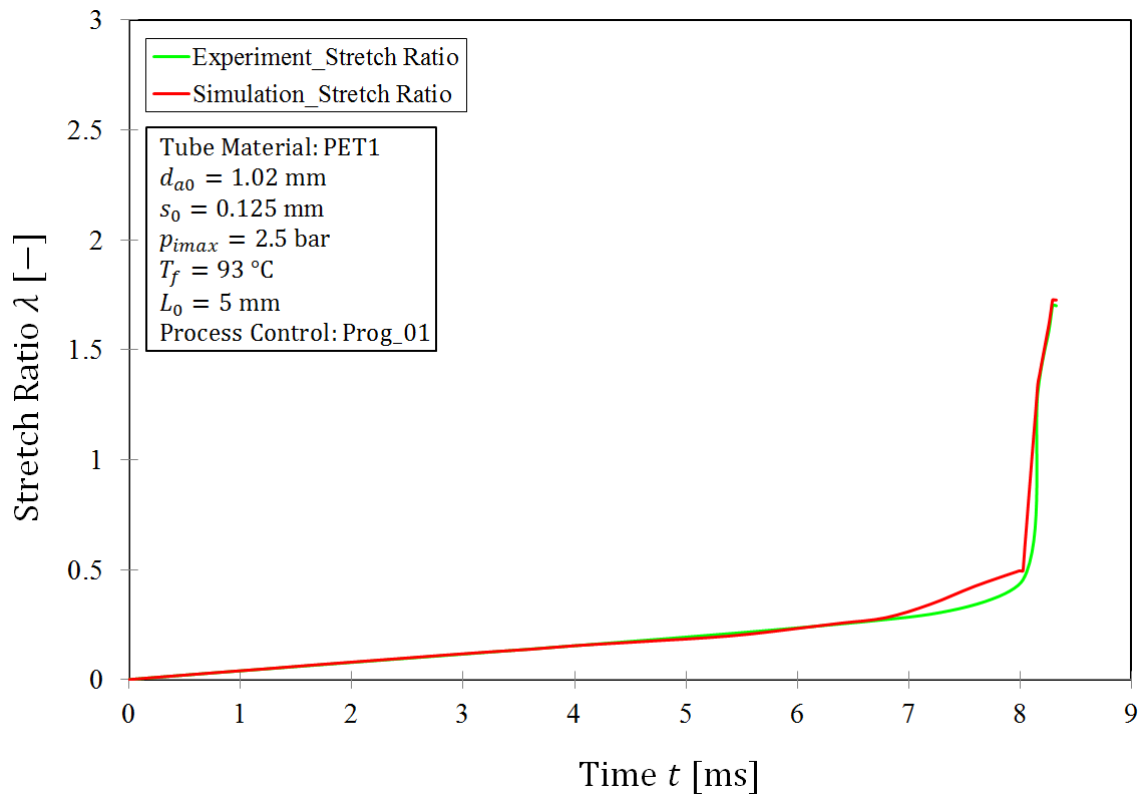


Figure 53 Stretch Ratio λ versus Time t development in the FE Analysis of the Experiment: $p_{imax} = 2.5$ bar and Process Control Prog_01. Tube Material: PET1

Compared to the result in Figure 52, the initial stage of the forming process was satisfactorily predicted in this Figure. The overall performance of the constitutive model is very satisfactory and in agreement with the experimental results shown in Chapter 6.

FE Analysis of the Experiment: $p_{imax} = 3$ bar and Process Control Prog 01. Tube Material: PET1

The FE analysis result of the experiment: $p_{imax} = 3$ bar and Process Control Prog_01 for the PET1 tube material is depicted in Figure 54 and illustrates the development of the stretch ratio λ against the forming time t .

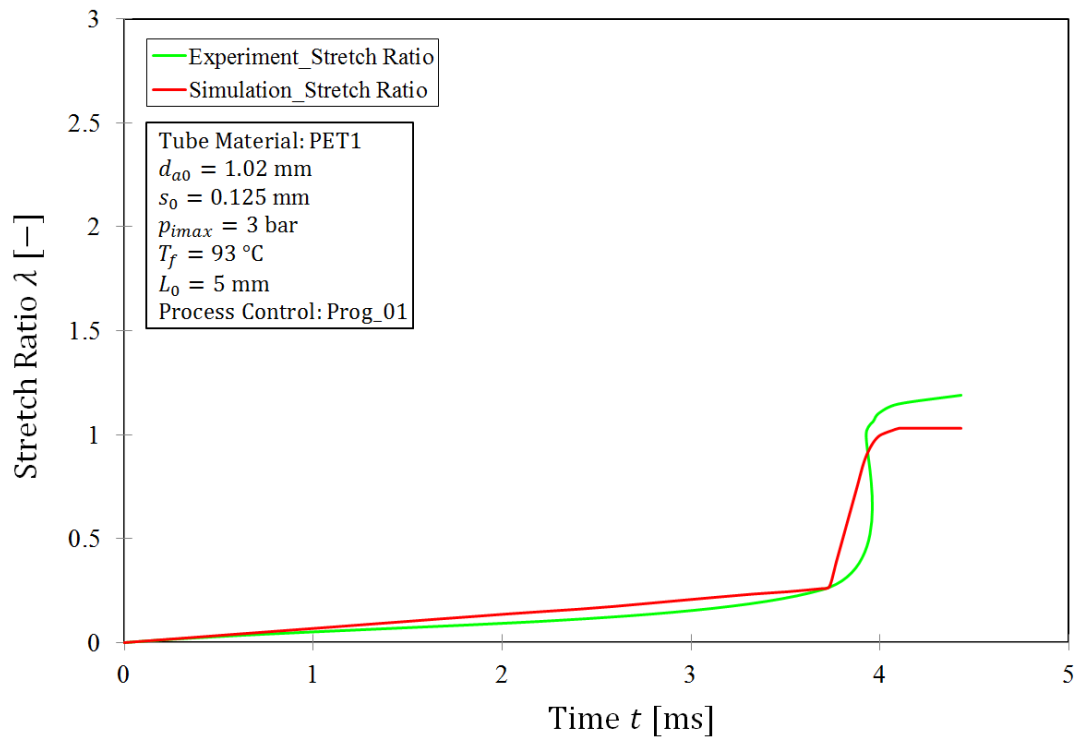


Figure 54 Stretch Ratio λ versus Time t development in the FE Analysis of the Experiment: $p_{imax} = 3$ bar and Process Control Prog_01. Tube Material: PET1

The model prediction of the experiment as illustrated in this Figure is also satisfactory. The prediction in Figure 54 was however more accurate. Beside the different p_{imax} and control programs in the experiment, the deviations in the tube material dimensions also significantly affected the experimental results. This influence was not relevant in the FE analysis, since the same tube dimensions were used in the analyses model.

FE Analysis of the Experiment: $p_{imax} = 6$ bar and Process Control Prog_02. Tube Material: PET1

Shown in Figure 55 is the development of the stretch ratio λ versus the forming time t in the FE analysis of the experiment: $p_{imax} = 6$ bar and Process Control Prog_02 also for the PET1 tube material.

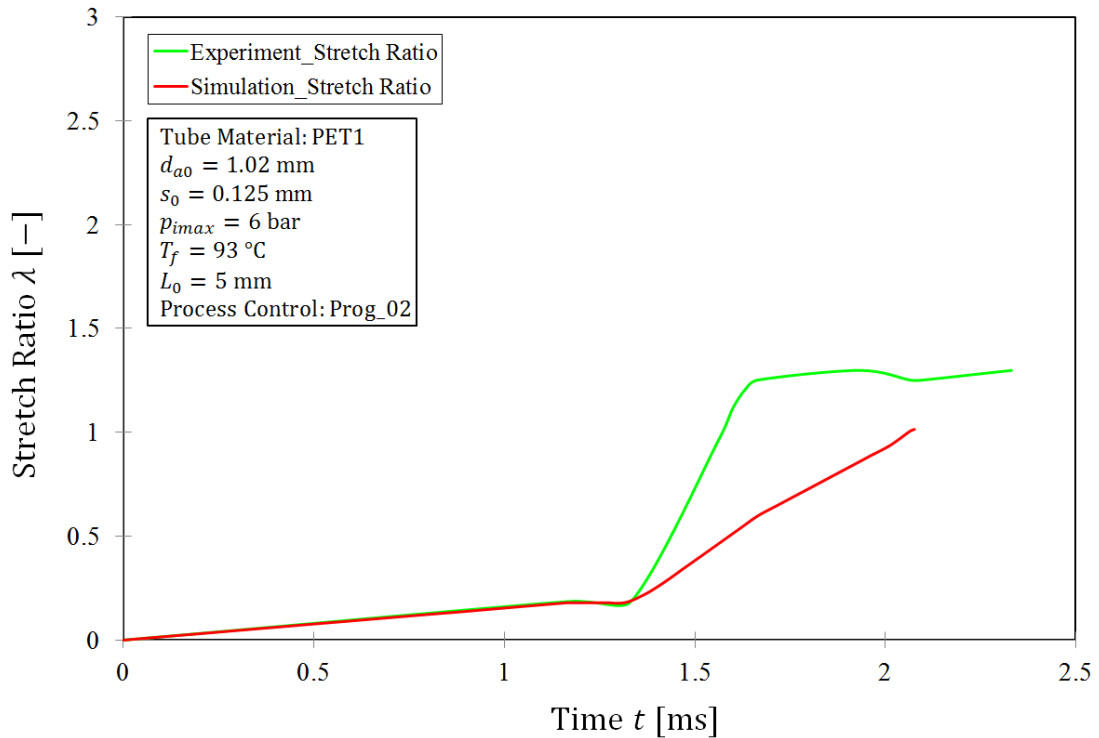


Figure 55 Stretch Ratio λ versus Time t development in the FE Analysis of the Experiment: $p_{imax} = 6$ bar and Process Control Prog_02. Tube Material: PET1

This Figure illustrates that the constitutive model performance is satisfactory within acceptable limits and in agreement with the experimental results shown in Chapter 6 and the failures discussed in Chapter 6.3. The FE analysis insensitivity to adiabatic heating and strain softening instability recoded in the experiment account mainly for the deviations of the simulated result. The analyses model was not developed to predict instability. Also, the CAX4R element used in the model can only deform under applied load or displacement.

FE Analyses: Evolution of the True Strain Rates $\dot{\epsilon}$. Tube Material: PET1

Depicted in Figure 56 is the evolution of the normalised true strain rates $\dot{\epsilon}$ as a function of the stretch ratio λ for the free forming experiments and FE-analyses of PET1 materials. The true strain rates were normalised to compare the experimental with FE-analyses results.

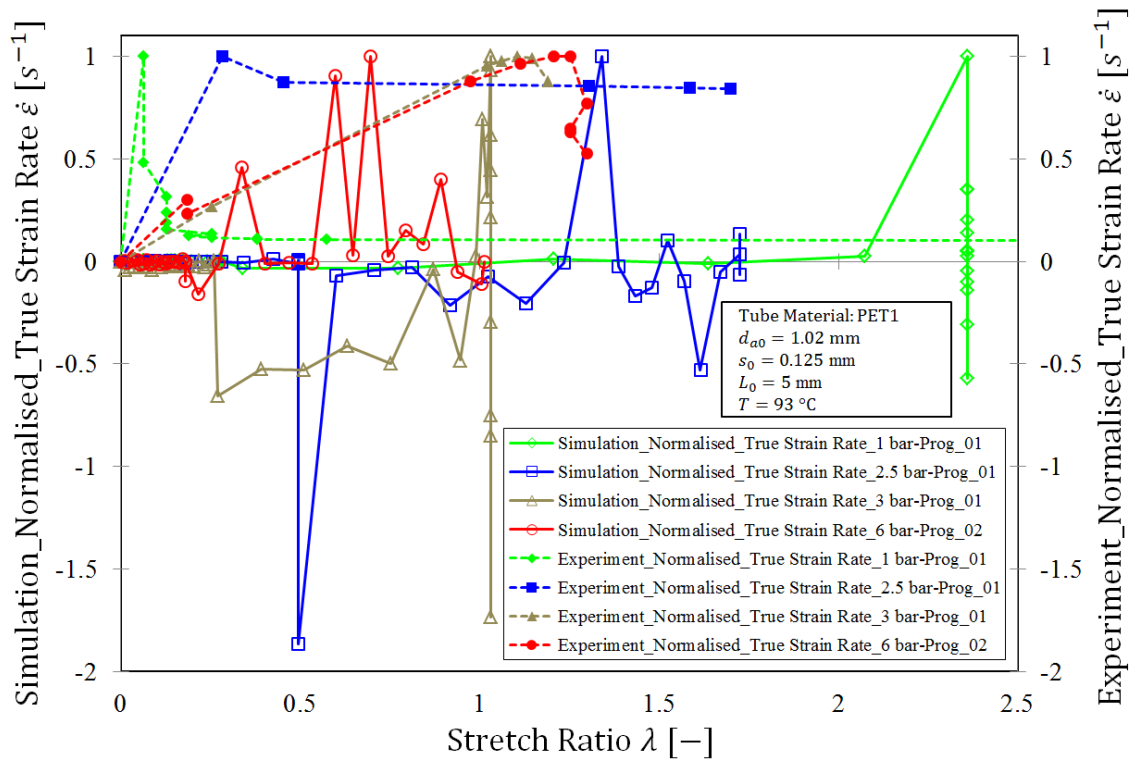


Figure 56 Comparison of the Normalised True Strain Rates $\dot{\epsilon}$ versus Stretch Ratio λ for the FE Analyses and the Experiments: $p_{imax} = 1, 2.5, 3$ and 6 bar with Process Controls Prog_01 and Prog_02. Tube Material: PET1

As expected the evolution of the true strain rate $\dot{\epsilon}$ as function of the stretch ratio λ in the FE Analyses deviated from the evolution in the experiments, since there was no tube dimensions deviation in the analyses compared to the experiments. In addition adiabatic heating discussed in Chapter 4.6, significantly influenced the deviation of the true strain rates $\dot{\epsilon}$ of the FE-analyses from the experiments. The model is not capable to account for adiabatic heating, which usually occur with large deformation of PET materials.

Further, instabilities recorded in the experiments contributed also to the deviations, as the negative strain rates $\dot{\epsilon}$ illustrated in Figure 56 for the FE-analyses started at the deformation zone associated with strain softening instability in the experiments. The deformation zones were illustrated in Chapter 6.3 for the results and discussions section of the free-forming experiments conducted.

Further, different result data point of collection and evaluation for the deformation evolution in the experiments and the FE-analyses contributed also to the deviation of the results. The experimental results were collected and evaluated at the maximum d_{at} – value points as described in Chapter 6. The FE-analyses results were correlated at the node with the maximum deformation in the radial or hoop (r – direction). Collected in Table 11 are the maximum stretch ratio λ_{max} recorded in the experiments and the FE-analyses at these points for comparison.

Table 17 Comparison of the Maximum Stretch Ratios λ_{max} recorded for the Experiments and the FE-Analyses for Tube Material PET1

Tube materials: PET1 Dimensions [mm]: d_{a0} 1.02 and s_0 0.125 Working Temperature T_f [°C]: 93		
Free Forming Experiments	Maximum Stretch Ratio λ_{max} [-]	
	FE Analyses	Experiment
$p_{imax} = 1$ bar, Prog Nr_01	2.36	2.74
$p_{imax} = 2.5$ bar, Prog Nr_01	1.73	1.70
$p_{imax} = 3$ bar, Prog Nr_01	1.03	1.19
$p_{imax} = 6$ bar, Prog Nr_02	1.01	1.30

In conclusion, the constitutive model predictions were quite satisfactory compared to the experimental results. The deviations can be attributed to complex material response and mainly due to the problem of temperature control. The experiments were conducted with 3 to 5 % temperature deviation recorded for most of the experiments, while adiabatic heating was not accounted for in the FE analyses. Temperature has a stronger influence on the variations such as mechanical properties in polymer processing as in blow forming [12-15, 46-51 and 56-58]. Instabilities of necking and strain softening are other important factors, which contributed to the deviations in the results. The FE analyses model was also not capable of accounting for the instabilities and will be subject of future improvement on the model.

In the FE analyses, the prediction of the deformation evolution in the experiments was most important in this study, which the analyses results with tube material PET1 for the Experiments: maximum internal pressures $p_{imax} = 2.5$ and 3 bar with the Process Control Prog_01 provided. The prediction of these experiments proved the potential of a less complicated constitutive model with four material parameters to predict polymer processing suitable for industrial applications.

9. Forming Limit Prediction in the Free-Forming of PET Micro Tubes

9.1 Introduction

During free forming of PET micro tubes or forming processes to induce large plastic deformation, there are limitations due to geometry and structure of the material as well as from the material history discussed in Chapters 4. Ductile failures are most often related to large deformations, plastic strains in metals, and irreversible strains in polymers and can occur during forming processes. They are however, associated with instabilities and the phenomenon of localization of strains and damage [138].

Although many polymeric materials behave as elastic solids for small deformations, there is a strain limit beyond which most polymers either fracture or undergo a continuing plastic deformation, called the yield process [12-15, 57].

Several researchers have to date used different ductile fracture or limit criteria to determine the limit strains and evaluate the forming limits for some metal forming processes [144-148] and [149-152] for polymers.

The basic assumption of these ductile fracture or limit criteria is that ductile fracture D_f occurs when the maximum damage value of a material exceeds a critical value C_f , which can be represented as in Equation 58 [148]:

$$\int D_f(\textit{deformation history})d\bar{\epsilon} = C_f \quad (58)$$

To date, no model predicts limit or fracture and failure had been determined to be suitable for all materials. Brozzo criterion in [146] is one of the mostly applied models to predict fracture and formability limit in metal sheet forming. The success of the model in the sheet metal forming makes it attractive in polymer forming, where the model has not been implemented until now. The significant of Brozzo criterion is mainly due to the consideration given to hydrostatic component of the stress state that has much influence in polymer forming and processing [82].

Moreover compared to other models, Brozzo criterion could be expressed in a simple mathematical form that involves only one material parameter C_f and was therefore chosen in this work to signify the first-time Brozzo criterion is been applied to polymer forming.

9.2 Forming Limit Prediction Concept

The importance of the concept of predicting forming limit consists in the possibility to establish the maximum strains that can occur before necking in a forming process [149].

In [146] the significant of predicting forming limits was defined on the deformation capability of a material, which would have been fully exploited at the onset of plastic instability. According to this assumption, [146] defined the forming limits of materials by the curves that describe the initiation of necking under different stress states and were represented by Equation 59 as:

$$\int_0^{\bar{\varepsilon}^p} \frac{2\sigma_1}{3(\sigma_1 - \sigma_m)} d\bar{\varepsilon} = C_{fmax} \quad (59)$$

where σ_1 is the maximum principal stress, $\bar{\varepsilon}^p$ the maximum effective plastic strain and σ_m the hydrostatic stress.

In this study this value was obtained from FE analysis up to inhomogeneous deformation (damage) for the free forming experiments. The maximum critical value C_{fmax} is a material parameter and can be obtained by a combination of the tensile experimental and the numerical simulation results [146, 148]. The FE analyses results were correlated at the integration point of the element with maximum equivalent plastic strain. The formability limit is achieved when the value of the integral equals the maximum critical value C_{fmax} as in Equation 59 [146].

To predict the forming limit in this study, the collected FE analysis results were post-processed (uncoupled analysis) in order to perform a backward-time integration of the limit criterion of Brozzo as depicted in the uncoupled approach in Figure 57 below. A fully-coupled analysis is costly [138].

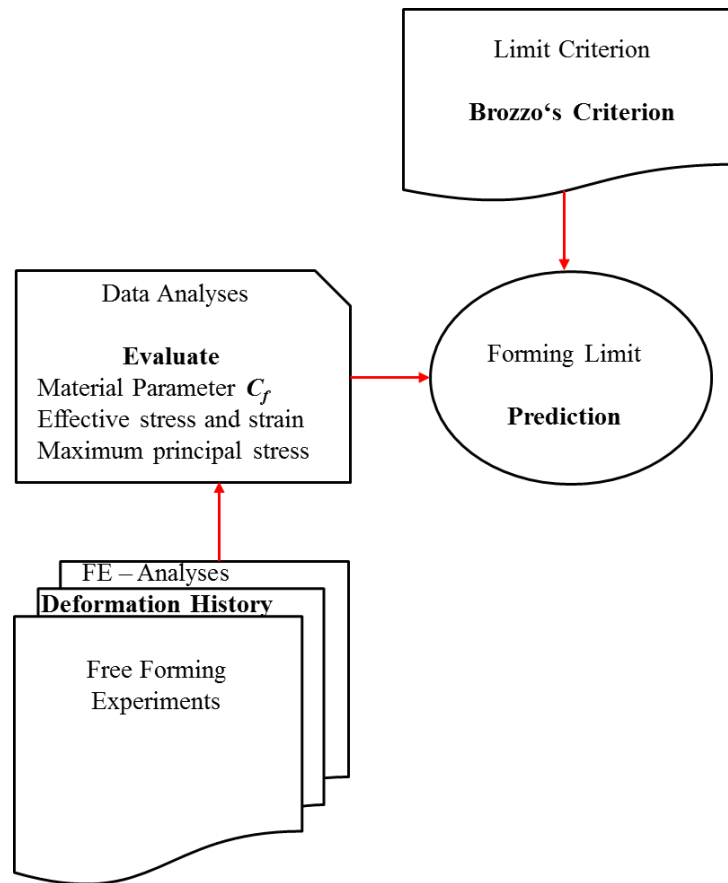


Figure 57 Uncoupled Approach to Predict Forming Limit in Polymer Forming using Criterion of Brozzo

For the limit prediction in this work, the FE analyses of the free forming experiment were simulated until damage. The FE analyses results of the maximum principal stress σ_1 and the hydrostatic stress σ_m as well as equivalent plastic strain $\bar{\epsilon}^p$ up to the damage points were correlated at the integration point of the element in the model with maximum equivalent plastic strain. Trapezoidal approximation method was used to implement Equation 59 with the collected FE analyses values to determine the maximum critical value C_{fmax} . The formability limit is achieved when the critical value C_f of the integral equals C_{fmax} as in Equation 59 [146].

The maximum critical value C_{fmax} of 1.44 was obtained for the experiment with maximum internal pressures $p_{imax} = 2.5$ bar and Process Control Prog_01. This $C_{fmax} = 1.44$ was chosen as the PET material parameter to relate Brozzo's criterion to the free forming experiments. The choice of this maximum critical value C_{fmax} was based on the experimental results analyses and physical observations of the process and the formed parts. The Experimental and FE Analyses results were presented in Chapters 6 and 8 above. The plot of the critical values C_f as function of the stretch ratio λ is depicted in Figure 58.

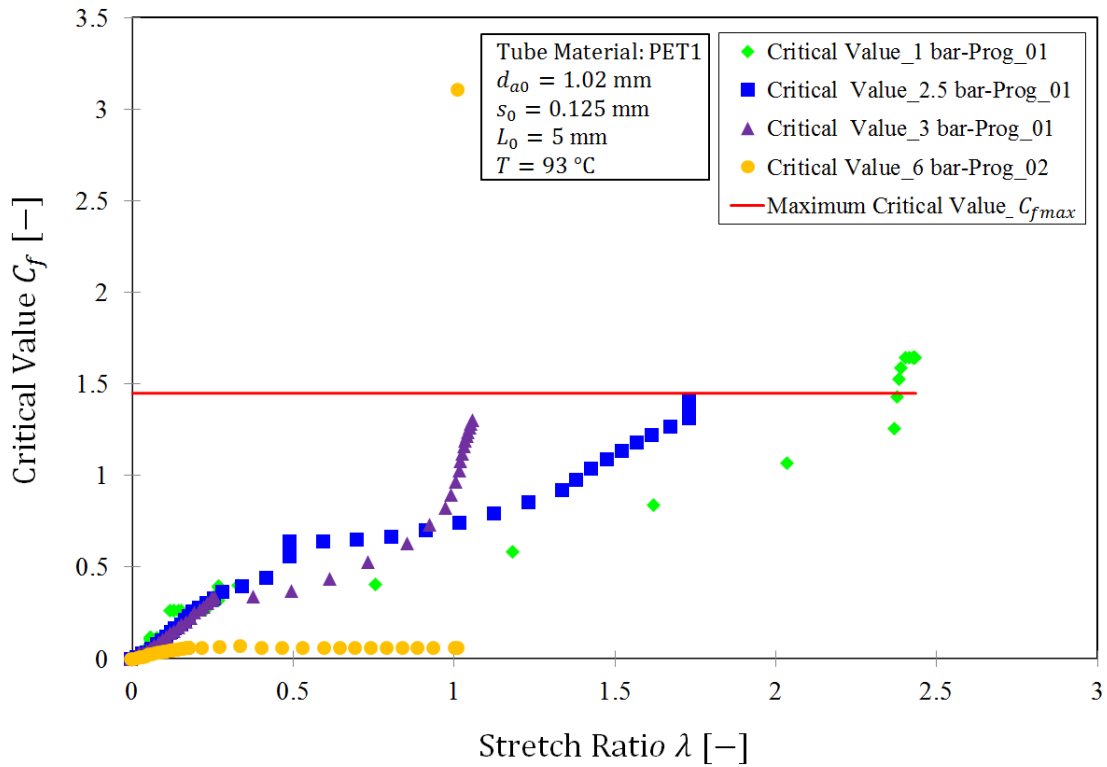


Figure 58 Critical Values C_f versus Stretch Ratio λ development. Tube Material: PET1 Tube

The plot in this Figure illustrates that for critical values $C_f > 1.44$ failure is recorded, since the defined maximum critical value C_{fmax} is 1.44. For Critical values $C_f < 1.44$ the formability limit is not achieved. Hence, the formability limit for PET1 tube material is achieved at maximum critical value $C_{fmax} = 1.44$. The evolution of the maximum critical value C_{fmax} for the experiment with maximum internal pressures $p_{imax} = 6$ bar and Process Control Prog_02 illustrates the significant of strain rate in the determination of maximum critical value C_{fmax} . The influence of strain rate in the formability limit analyses for polymeric materials with the criterion from Brozzo will be further investigated in the future research.

Similar to any new approach, the method will require more experiments to validate the robustness of the application and prove the applicability in industrial polymer process. This task will also be subject of future research and will be addressed in the planned future work on the blow forming of polymeric micro tubes.

10. Case Study-Forming of Tubular Micro-Components and Conclusions

10.1 Machine Concept for the Forming of Tubular Polymeric Micro-Components

Forming machine was developed in this study to extend the conventional injection stretch blow moulding technology reviewed in the forming of polymeric micro tubes. The machine design was based mainly on the free-forming experimental device and results presented in Chapter 6. The machine modules are depicted in Figure 59.

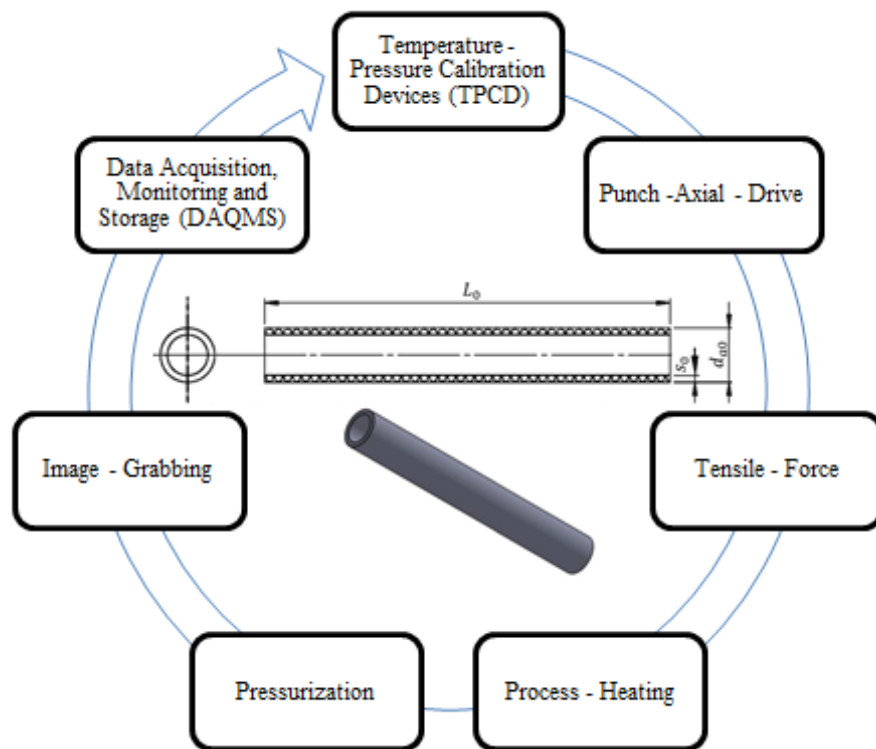


Figure 59 Design concept considerations of the Micro Blow Moulding Machine layout

The design concept consideration depicted in Figure 59 was implemented into the blow forming machine and platform design. The modular design strategy applied for the free-forming device enabled easy scale-up of the device to the blow moulding machine system depicted in Figure 60 below.

The machine enabled the precise selection of blow forming parameters and control of the sequence and timing of individual steps in a forming cycle. The machine design concepts enabled also the process parameters: tensile force F_z , working temperature T_f

and internal pressure p_i to be operated in both manual and automatic mode. The internal pressure p_i and the superimposed tensile force F_z interactions determine the achievable forming rate and stretch ratio λ . The tools design strategies applied in this work enabled easy part removal from mould-insert, manufacture of parts with high aspect ratio and suitability of micro blow moulding technology in micro manufacturing for volume production.

To address the challenges associated with the application of a stretch rod in the conventional blow moulding process, a new sealing and pressurization technique was developed and tested in the free-forming experiments in Chapter 6. The new strategy was necessary for a robust sealing and pressurization for micro blow moulding process application. Sealing system for micro blow moulding process has to be designed in a way that avoids a loss of process reliability which may be caused by imprecision while inserting the stretch rod or localized stress and strain [47] during the moulding process. To enable multidirectional stretching or orientation of the micro tube as provided by the stretch rod in conventional process, a strategy to superimpose axial tensile force F_z externally was implemented as presented in Chapter 6.

Most problems in micro moulding are coupled with demoulding. During demoulding, micro structures may be torn apart, deformed, or destroyed, if the micro part is not designed properly or unsuitable moulding parameters are chosen. An important factor in demoulding is the shrinkage of the polymer during cooling of the formed part in the mould. Demoulding forces are a function of the orientation of microstructures relative to the direction of shrinkage and the position of critical micro part structures relative to the center of shrinkage. An inclination angle of just 2° reduces demoulding forces significantly and is even more important than the roughness of the side walls [2]. The mould-insert defines part shape, but, as with other thermal processes, addition of shrinkage allowances is important [3-6, 29, 30 and 38]. Inclination of 2° and shrinkage allowances were implemented in the mould design for the investigations conducted in this work.

Parting lines with a symmetrical material distribution within the two forming mould-insert halves are recommended. For the case of parting lines that lead to unsymmetrical material distribution, a locally adapted thermal energy supply implemented in this work was necessary, in order to obtain the required forming result.

Adhesion of the heated and formed micro part to the surface of mould-insert represented also a significant impact on the process reliability and product quality. Exceeding a critical amount of adhesion force can result in distortion of the formed part on or during removal from the forming the mould-insert. The impact of adhesion forces is higher for formed micro parts compared with macro parts and could be attributed to the size-effect caused by increased ratio A/V . Although the adhesion forces are of similar dimension in both processes, the resulting stresses within the wall of the micro parts are higher considering the thinner wall thickness of these parts. In principle, common mould-release agents can be applied to reduce adhesion. However, this application means

additional effort and process time, as well as the eventual deposition of release agent residua in the mould-insert. Optimized mould-system-design and mould-insert coating are the measures employed in this study and recommended for industrial applications.

Proper venting as reviewed is also important in mould design. Venting for the mould-insert used in this work was achieved with small bores in the mould-insert. The tools design strategies applied in this work enabled easy part removal from mould-insert, manufacture of parts with high aspect ratio and suitability of micro blow moulding technology in micro manufacturing for volume production.

10.2 Micro Blow Moulding Machine for Polymeric Micro-Tubes

Figure 60 shows the assembled micro blow moulding machine system capable for the volume manufacture of polymer components made from micro tubes, designed on the basis of the findings developed in the investigations presented above. The machine system contains various actuators for the controlled application of the process loads, sealing, thermal management as well as for the component handling, and enables the pressurization and forming of micro-tubes below a diameter of about 1300 μm with pressures of up to 50 bar.

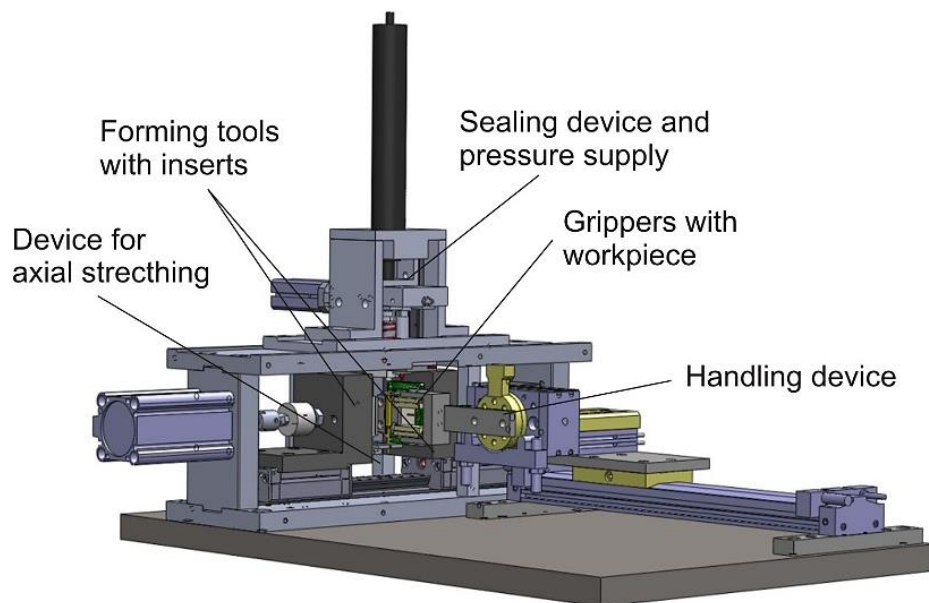


Figure 60 Micro Blow Moulding Machine System

The hardware for this machine system are scaled-up modules of the free-forming experimental device presented in Chapter 6. The results of the free-forming design were transferred to mould-insert design.

The optimization measure here focused mainly on the heating and cooling management with the mould-insert-system. Localized heating strategy was implemented to account for the size-effect associated with polymeric micro tubes and was discussed Chapter 3.2.

The investigations with the mould-insert were validated and quantified with the case study-demonstrators shown in Figure 61.

The developed machine in this Figure will address the problem with the mass production of components for medical and biomedical devices, pharmaceutical products and micro fluidic technology.

10.3 Case Study-Polymeric Tubular Micro-Components

Based on the results of investigations conducted, demonstrator micro components depicted in Figure 61 were designed and manufactured to investigate the requirements for suitable tool design in the manufacture of polymeric micro tubular (hollow) components. The demonstrators were formed from polymeric micro tubes, PA 6 and PET with initial outer diameter d_{a0} of 1340 μm and initial wall thickness s_0 of 170 μm .

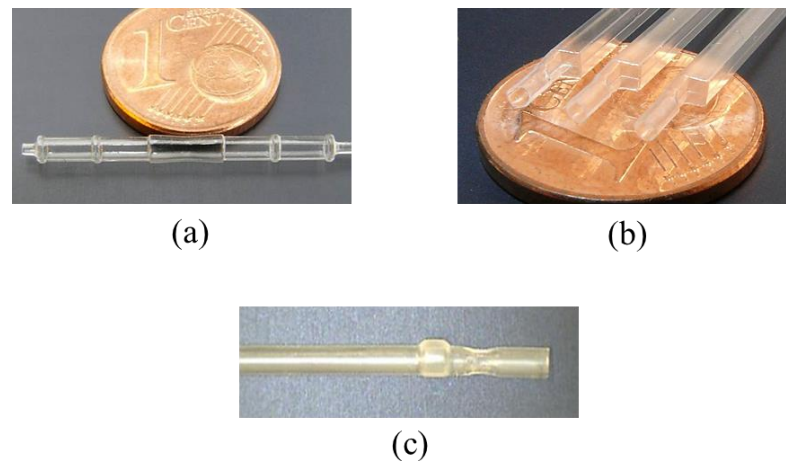


Figure 61 Demonstrators to validate Mould-Insert Blow Forming Process of Polymeric Micro Tubes: (a) Material PET; Fluidic Connector (b) Material PET; Micro Heat Exchanger Housing (c) Material PA 6; Component for a Sperm Cell Separator Device

As expected, the components made from the PA 6 material required higher working temperature T_f and lower p_{imax} than the parts made from PET. Influence of shrinkage on the formed part quality was higher by parts produced from PA 6 micro tube materials depicted in Figure 61 (c) than the formed demonstrators with PET micro tubes in Figure 61 (a) and (b).

Table 18 represents the essential forming parameters for the demonstrators manufactured with mould-inserts [153]. Suitable forming period of between 30 to 40 ms and a maximum formed hoop (radial) ratio of 2 were achieved. The ratio was determined by the mould-insert design and the initial micro tube dimensions based on the functional requirement of the manufactured parts.

Table 18 Forming Parameters for the Demonstrators [153]

Micro tube material	d_{a0} [mm]	s_0 [mm]	p_{imax} [bar]	T_f [°C]
PA 6	1.34	0.17	15	190
PET	1.34	0.17	18	90

10.4 Conclusions

Overall, the thesis presented investigations of blow moulding process for the manufacturing of tubular (hollow) shaped polymeric micro components and provided first fundamentals for applications. The forming principle of the developed process was based on the inner pressurization of a heated micro tube within mould-insert.

Conventional blow forming processes use mandrels to supply pressurized air into the pre-form. The mandrel, which has to be inserted with a certain precision into the tube end, is clamped by closing the forming die halves to achieve sealing. Sealing system developed and designed in this work prevents a loss of process reliability which may be caused by imprecision when inserting the mandrel into the micro tube, while the process design enabled precise control of the process parameters.

Micro blow moulding applied to serial production is a new manufacturing method for tubular polymeric micro components. The process principle is based on the forming of polymeric tubes by internal pressurization with a superimposed axial tensile stress under evaluated temperature. The objective of this thesis is to develop fundamentals for process and tools design to enable large scale manufacture of polymer tubular micro components through blow forming process.

The investigations were divided into fundamental research work (initial and second stages); the influence of process parameters on the feasible forming of polymeric micro tubes, and final or third stage which described the development of a functional blow forming machine depicted in Figure 60 to form polymeric micro tubes based on the results from the second stage of the investigations.

Micro components demonstrators in Figure 61 were produced to validate the optimized process. The second stage of the research is presented in this thesis, while detail of the final stage was presented in [154]. The Chapter provides an insight into the process principle, and particularities for the process development and design associated with scaling down conventional blow moulding processes to micro scale processing.

This thesis was structured into Eleven Chapters. Introduction in Chapter 1 presented immediately after the Abstract, detailed the background, objective and the methodology of the study. This Chapter served as an introduction and a guide in this fundamental investigation as well as the summary of the tasks in the study.

The literature review of blow forming of polymeric micro tubes was presented in Chapter 2 following the introduction of the study. In this Chapter the fundamentals of polymers, manufacturing in micro technology of polymer forming, and overview on micro manufacturing as well as micro blow moulding were reviewed.

The reviews in Chapter 2 provided the introduction of polymer forming and micro manufacturing processes, issues and challenges involved in designing these processes. In blow moulding process, the major concern is to choose the process variables such working temperature T_f , internal pressure p_i , and the rate of pressurization and the tensile force F_z so as to achieve multiaxial orientation of the formed polymer parts and improve their mechanical properties. Furthermore, tools and parts design need to be optimized to achieve defect free and high aspect ratio products. Size-effects and the challenges of down-scaling of conventional to micro manufacturing process were also discussed in this Chapter.

The process concepts design in the forming of polymeric micro tubes developed in this study were introduced in Chapter 3 after studying the deformation behaviour of thermoplastic polymers in Chapter 2. These concepts design were based mainly on the reviews in Chapters 2 and the background knowledge in micro forming technology. Adequate heating source, tensile force F_z , sealing force F_s and pressurization strategy suitable for micro manufacturing is significant in the equipment design for micro blow forming process and were addressed in this Chapter.

Chapter 4 described the classical theory of plasticity and deformation behaviour of thermoplastic polymers, yield criteria, plastic forming, hardening laws as well as instabilities during forming of materials.

The blow forming process involves plastic deformation of the micro tubes due to stresses applied by internal pressure p_i , and the tensile force F_z at an elevated working temperature T_f . In view of this, the review of the concept of the stress and strain were discussed in this Chapter. Yield criteria for isotropic materials covered in this Chapter, discussed the version of modified von Mises criterion, which accommodates the differences in tensile and compressive yield strengths and accounts for any dependence of yielding on the hydrostatic component of the applied stress state. There have been a number of detailed investigations of the influence of hydrostatic pressure on the yield behaviour of polymers, hence the importance of the discussion on the pressure dependent yield criterion. The influence of strain rate and temperature in processing thermoplastic polymers were also covered in this Chapter. Finally, crazing and shear failures as well as necking and strain softening instabilities in the processing of polymers were presented.

The first experimental results in this study were presented in Chapter 5. In the experiments, dynamic mechanical analysis (DMA) of the polymeric micro tubes were carried-out to determine their glass transition temperature T_g . Knowledge of the glass transition temperature T_g is necessary to design process, device and machine for the investigation of the formability of polymeric materials.

With the introduction and reviews of polymeric material behaviours and micro manufacturing in Chapters 1 and 2 respectively, the process concepts definition in Chapter 3 as well as the DMA results in Chapter 5, the free-forming experiments to investigate the formability of the polymeric micro tubes were conducted in Chapter 6.

In the fundamental deformation behaviour of materials discussed in Chapter 4, large, time dependent inelastic deformations such as viscoplastic behaviour in polymer materials, is based on the criteria of a yield surface or yield function giving the yield condition hardening rules. The hardening rules determine the change of the yield surface during deformations and on the relation of the stresses and plastic strains relations of materials in a multiaxial deformation also described in Chapter 4. These relations were used to formulate constitutive models and quantify materials responses during plastic deformations. The aim of Chapter 7 was to develop a simple and manufacturing oriented constitutive model for blow forming of polymeric hollow components. Since, there is no completely general model that describes all the features in a deformation process, in many application, only relevant aspect of material behaviours are represented in a constitutive model to accurately characterize the behaviour of the polymer tube materials.

To facilitate the numerical analysis of the blow forming process and enable the reduction of development time and cost in blow forming process, a constitutive model based on Hensel-Spittel model was presented in Chapter 7. The developed model was calibrated with biaxial PET material experimental data from the literature applying regression analysis method. Results of the parameter identification and the calibrated model were given in this Chapter.

Applying the constitutive model developed in Chapter 7, FE analyses of the free forming process were conducted in Chapter 8. The FE analyses enabled the validation and verification of the applicability of the developed constitutive model in polymer forming process. Free-forming experimental results given in Chapter 6 were used for the validation and verification of the constitutive model.

The significant of predicting forming limits on the deformation capability of a material, which would have been fully exploited at the onset of plastic instability, cannot be overstated. In view of the need to predict forming limits in the blow forming process and reduce cost and time to manufacture, numerical method to predict forming limit in polymer tube material was provided in Chapter 9.

Process design concepts in the forming of polymeric micro tubes developed in this study were introduced in Chapter 3 after the determination of the polymer materials glass transition temperatures T_g and studying the deformation behaviour of thermoplastic polymers in Chapter 3. These concepts were based on the reviews in Chapters 1 and 3 and the background knowledge in micro forming technology. Adequate heating source, tensile force F_z , sealing force F_s and pressurization strategy suitable for micro manufacturing is significant in the equipment design for micro blow forming process and were addressed in this Chapter.

Based on the results of the free-forming experiments conducted in Chapter 6, blow moulding machine concept and development to tubular micro components were carried-out in Chapter 10. In this Chapter the developed machine system for the volume production of polymeric micro components was presented in fulfilment of the aims and objectives of the study. Case studies with demonstrator components were presented in this Chapter to validate the objectives and aims of the investigations. Also in this Chapter the structure and conclusions in these fundamental investigations were detail.

Finally in Chapter 11, contribution of this study to knowledge and suggestions for future work were presented, due to increasing demand for micro components in large quantities for medical as well as non-medical applications. The required component are to a large extent a hollowed shaped made from polymers, hence the main aim of the future work is to enable industrial application of the results achieved in this important fundamental research work to address the challenge of existing demand and development of new products.

Results from the experiments presented above and the machine system depicted in Figure 60 proved that objectives and aims of the investigations as defined in Chapter 1 were successfully achieved.

11. Contribution to Knowledge and Suggestions for future work

With the objective to provide a technology for the economic mass production of complex shaped hollow components made from polymeric materials the novel process of micro blow moulding was developed and investigated. Based on conducted fundamental research work the manufacture of micro demonstrator parts (Study Cases) were successfully produced and depicted in Figure 61. Further, concepts and strategies for improvement of process reliability and suitable tool design have been provided.

Experimental method and plan developed in this study and detailed in Chapter 6 will close the gap in the forming of most highly viscoplastic materials such as polymers at very high strain rates required in the manufacturing industry. The flexibility provided in the design of the method and plan allowed the application to other hollow materials at high forming rates applying internal pressurization such as in hydroforming of metallic hollow parts.

Testing of polymeric preforms or semi-finished tubes at blow moulding conditions is an unexplored area of behaviour. The experimental equipment described in Chapter 6, which was developed in this fundamental research work will address the challenge of testing equipment for polymeric hollow samples for blow forming application. Beside the testing technique in [51], which merely characterizes polymer films for blow forming application, no equipment to wholly characterize polymeric tubes had been published up to date.

For the analytical and FE analyses of the stress state of the micro tube in the forming process, material experimental data based on the conditions applicable to blow forming process as with the experimental equipment in Chapter 6 will be more suitable for the analyses than the biaxial test data from the literature.

Hence future work plan include acquisition of the true stress and true strain material data of the forming process for the polymeric micro tubes with the experiment equipment described in Chapter 6. To achieve this objective, this equipment will be optimized and equipped with 3D Digital Image Correlation (DIC) System. Redesign and optimization of the equipment heating module is also been planned to achieve adequate and stable heat distribution module for micro tubes such as PA 6 and PC, which require higher working temperatures T_f as in the mould-insert design. The optimized designs will enable the application of the 3D DIC system, which is not applicable in the mould-insert process.

On successful optimization of the experimental equipment in Chapter 6, more free forming tests are planned to adequately verify and validate the potential of the constitutive model in Chapter 7 for the manufacturing of polymeric micro parts

application. In the FE analyses, more verification and validation on the forming limit application of the Brozzo criterion, which is applied for the first time in polymers processing will also be conducted. The successful application of this criterion in polymer processes will reduce time in the development of forming processes of polymeric parts.

Major advantages of micro blow moulding consist in the possibility to generate hollow shaped complex geometries in a single forming step from economically priced extruded polymeric micro tubes.

12. List of References

- [1] Y. Qin, Chapter 1 in Micro manufacturing Eng. and Tech., 1st Edition, edited by Yi Qin, (Elsevier, 2010).
- [2] M. Hecke, W. K. Schomburg, J. of micromech. and microeng. Review 14, (2004), R1-R14.
- [3] U. M. Attia et al., Microfluid Nanofluid 7, 1-28, (2009).
- [4] J. Giboz, T. Copponex, P. Mélé, Microinjection molding of thermoplastic Polym. Review. 17, (2007), R96-R109.
- [5] L. Weber et al., in Proceedings of Symp. Micromachining Microfabrication 156, (1996).
- [6] S. H. Park et al., in eXPRESS Polym. Letters 5, 11 p. 950–958, (2011).
- [7] C. Hartl, J. of Mat. and Proc. Tech. 167, p. 383-392, (2005).
- [8] C. Hartl, G. Anyasodor, in Proceedings of International conference on metal Forming, p. 1193-1996, (2010).
- [9] M. Saab, U.S. Patent 5, 624, 392 (1997).
- [10] M. Focke et al., in Proceedings VDE Mikrosystemtechnik-Kongress, (VDE-Verlag, 2009), p. 101-104.
- [11] N. Choudhury et al., Proceedings of the Polym. Processing Soc. 24th Annual Meeting, (2008).
- [12] J. Rösler, H. Harders, M. Bäker, Mechanisches Verhalten der Werkstoffe, 3. Auflage, (Springer, 2008).
- [13] C. E., Carraher, Jr., Polym. Chemistry, 6th Edition revised and expanded, (Marcel Dekker, 2003).
- [14] H.F. Brinson, L. C. Brinson, Polym. Eng. Sci. and Viscoelasticity-An Introd., (Springer Science, 2008).
- [15] D. I. Bower, an Introd. to Polym. Phys., (Cambridge University Press, 2002).
- [16] E. Rianda et al., Polym. Viscoelasticity, (Marcel Dekker, 2000).
- [17] M. F. Ashby, D. R.H. Jones, Eng. Mat. 2-An Introd. to Microstructure, Processing and Design, (Pergamon Press, Oxford, 1986).

- [18] W. Bergmann, *Werkstofftechnik, Teil 1-Grundlagen*, 3rd Edition, (Hanser Verlag, 2000).
- [19] R. N. Haward, *Introduct. in The physics of glassy polymers*, edited by R. N. Haward, (Applied science publishers Ltd., 1973).
- [20] M. Ward, J. Sweeney, *An introd. to the mechanical properties of solid polymers*, 2nd Edition, (Wiley, 2004).
- [21] D. R. Askeland, P. P. Fulay, *Essentials of Mat. Sci. and Eng.*, 2nd Edition, (CENGAGE Learning, 2009).
- [22] S. J. Hiermaier, *Struct. Under Crash and Impact Continuum mech., discretization and experimental characterization*, (Springer, 2008).
- [23] M. P. Groover, *Fundamentals of modern manufacturing*, 4th Edition, (Wiley, 2010).
- [24] A. Paulus et al., in *Proc. SPIE Microfluidic Devices and Systems*, Vol. 3515, Santa, Clara, CA 1998, pp. 94–103.
- [25] D. C. Duffy et al., *Analytical chemistry*, 70 (23), 4974-4984, (1998).
- [26] M. A. Burns et al., *Sci.* 282, 484–487, (1998).
- [27] Y. H. Chen, S. H. Chen, *Electrophoresis* 21, 165–170, (2000).
- [28] M. A. Shoffer et al., *Chip PCR I. Nucleic Acids Res* 24, 375–379, (1995).
- [29] L. Weber, W. Ehrfeld, in *Proceedings of the 56th annual technical conference* 3, (1998), p. 26-30.
- [30] A. K. Angelov, J. P. Coulter, in *Proceedings of the annual technical conference* 1, (2004), p. 16-20.
- [31] O. Rötting et al., *Microsystem Technologies* 8, (Springer 2002), 32-36.
- [32] Bartels Microtechnik, <http://www.bartels-mikrotechnik.de>, Accessed on 2014-10-02.
- [33] Microfluidic ChipShop GmbH, *Lab-on-a-Chip Catalogue 03/2014*, Available at <http://www.microfluidic-chipshop.com>. Accessed on 2014-10-02.
- [34] D. V. Rosato et al., *Injection Molding Handbook*, 3rd Edition, (Kluwer Academic, 2000).
- [35] B. H. Min, *J. Mat. Process Tech.* 136, p.1-6 (2003).
- [36] R. Surace et al., Chapter 4 in *New Technologies-Trends, Innovations and Research*, edited by C. Volosencu, (InTech 2012).
- [37] D. Rosato, D. Rosato, *Plastics engineered product design*, (Elsevier, 2003).

- [38] H. Belofsky, *Plastic-product design and process Eng.*, (Carl Hanser, 1995).
- [39] F. Vollertsen, in *Proceeding of the 1st colloquium process scaling*, (Bremen, 2003), p. 1-9.
- [40] U. Engel et al., *J. Mat. Proc. Tech.* 125-126, p. 35-44 (2002).
- [41] D. Drummer et al., *J. Mat. Sci. and Eng.* 2 (6), p. 347-362, (2012).
- [42] E. Mitsouli, Chapter 4 in *Modeling and simulation in Polym.*, edited by P. D. Gujrati and A. I. Leonov, (Wiley-VCH, 2010).
- [43] Y. Qin, *J. Mat. Proc. Tech.* 177, p. 8-18, (2006).
- [44] A. Dawson et al., *Polym. Testing* 27, p. 555-565, (2008).
- [45] L. Cosma, Chapter 2 in *Specialized molding techniques*, edited by Hans-P. Heim and H. Potente, (William Andrew, 2002).
- [46] J. A. W. M. Groot et al., *CASA Report* 11-27, 2011.
- [47] F.M. Schmidt et al., *J. Non-Newtonian Fluid Mech.* 64, p. 19-42, (1996).
- [48] M. Cakmak et al., *J. of Appl. Polym. Sci.* 30, p. 3679-3695, (1985).
- [49] Z. J. YANG et al., *Polym. Eng. and Sci.* 44, 7 (2004).
- [50] B. Cosson et al., *Int. J. Mat. Forming* 5, p. 39-53, (2012).
- [51] C.P. Buckley, C.Y. Lew, *Polym.* 52, p. 1803-1810, (2011).
- [52] J. J. Allen, *Micro electro mechanical systems design*, (CRC Press, 2005).
- [53] J. P. Holman, *Heat Transfer*, 6th edition, (McGraw-Hill, 1986).
- [54] K. S. Akhtar, S. Huang, *Continuum theory of plasticity*, (Wiley, 1995).
- [55] K. K. Chawla, M. A. Meyers, *Mechanical behavior of Mat.*, 2nd Edition, (Cambridge, 2009).
- [56] A. D. Drozdov et al., *Acta Mechanica* 154, p. 189-214, (2002).
- [57] M. C. Boyce et al., *Polym.* 41, p. 2183-2201, (2000).
- [58] P. G. Llana, M. C. Boyce, *Polym.* 40, p. 6729-6751, (1999).
- [59] G. Holzapfel, J. Simo, *Int. J. Solids Struct.* 33, p. 3019-3034, (1996).
- [60] J. S. Zaroulis, M. C. Boyce, *Polym.* 38, p. 1303-1315, (1997).
- [61] E. G. Septanika, L. J. Ernst, *Mech. Mat.* 30, p. 255-273, (1998).
- [62] E. M. Arruda, M. C. Boyce, *J. Mech. Phys. Solids* 41, p. 389-412, (1993).
- [63] B. J. Lee et al., *Polym.* 34, p. 3555-3575, (1993).

- [64] P. Le Tallec et al., *Comp. Meths in Appl. Mech. and Eng.* 109, p. 233-258, (1993).
- [65] H. G. H. van Melick, PhD. thesis, Technische Universiteit Eindhoven, 2002.
- [66] M. C. Boyce et al., *Mech. of Mat.* 7, p. 35-47, (1988).
- [67] O. A. Hasan et al., *J. of Polym. Sci. Part B: Polym. Phys. Edition* 31, p. 185-197, (1993).
- [68] E. M. Arruda, M. C. Boyce, *Int. J. of Plasticity* 9, p. 697-720, (1993).
- [69] M. C. Boyce et al., *Polym. Eng. and Sci.* 34, p. 716-725, (1994).
- [70] T. A. Tervoort et al., *Mech. Time Dep. Mat.* 1, p. 269-291, (1998).
- [71] A. F. Bower, *Appl. Mechanics of solids*, (CRC Press, 2010).
- [72] G.H. Menary et al., *Polym. Eng. & Sci.* 52, p. 671-688, (2012).
- [73] R. N. Haward, G. Thackray, in *Proceedings of the R. Soc. London Ser. A*, (1968), p. 302-453.
- [74] P. H. M. Timmermans, PhD. thesis, Technische Universiteit Eindhoven, 2002.
- [75] L.E. Govaert et al., *J. Eng. Mat. Tech.* 122, p. 177-185, (2000).
- [76] S. Matsuoka, B. Maxwell, *J. of Polym. Sci. XXXII*, p. 131-159, (1938).
- [77] G. A. Holzapfel, *Nonlinear Solid Mechanics*, (John Wiley, 2000).
- [78] D.W. Holmes et al., *Mech Time Dep. Mat.* 10, p. 281-313, (2006).
- [79] M. Polanco-Loria et al., *Int. J. of Impact Eng.* 37, p. 1207-1219, (2010).
- [80] F. Dunne, N. Petrinic, *Introd. to Computational Plasticity*, (Oxford University Press, 2006).
- [81] I. M. Ward, *J. of Mat. Sci. Review* 6, (1971), p.1397-1417.
- [82] R. Raghava et al., *J. of Mat. Sci.* 8, p. 225-232, (1973).
- [83] S. Rabinowitz et al., *J. Mat. Sci.* 5, p. 29-39, (1970).
- [84] P. B. Bowden, Chapter 5 in *The physics of glassy Polym.*, edited by R. N. Haward, (Applied science, 1973).
- [85] D. Roylance, *MIT Mat. Sci. and Eng.-Mech. of Mat. MA 02139*, (Cambridge, 2001).
- [86] S. S. Sternstein et al., in *Appl. Polym. Symp.* 7, (Interscience, 1968), p. 175.
- [87] S. Sternstein, L. Ongchin, in *Appl. Polym. Symp.* 7, (1968), p. 1117-1124.
- [88] R. Hill, *The Mathematical Theory of Plasticity* 38, (Clarendon Press, 1950).

- [89] W. Han-Chin, *Continuum mechanics and plasticity*, (CRC Press, 2005).
- [90] J. A. Sauer, K. D. Pae, *Colloid and Polym. Sci.* 252, p. 680-695, (1974).
- [91] P. W. Bridgman, *Studies in large plastic flow and fracture with special emphasis on the effects of Hydrostatic Pressure*, (McGraw-Hill, 1952).
- [92] B. I. Bereshev et al., *Some problems of large plastic deformation at high pressure*, (Pergamon Press, 1963).
- [93] J. Chakrabarty, *Theory of Plasticity*, 3rd Edition, (Butterworth-Heinemann, 2006).
- [94] P. J. Armstrong, C. O. Frederick, *Berkeley Nuclear Laboratories Report RD/B/N731*, 1966.
- [95] F. Yoshida, T. Uemori, *Int. J. Plasticity* 18 (5–6), p. 661–686, (2002).
- [96] W. F. Hosford, R. M. Caddell, *Metal Forming Mech. and Metallurgy*, Third Edition, (Cambridge University Press, 2007).
- [97] R. N. Haward, Chapter 6 in *The physics of glassy polym.*, edited by R. N. Haward, (Applied science publishers, 1973).
- [98] R. P. Chartoff et al., Chapter 5 in *Dynamic mechanical analysis (DMA) in thermal analysis of polym.- Fundamentals and Applications*, edited by J. Menczel, R. B. Prime, (Wiley, 2009).
- [99] D. W. van Krevelen, K. Te Nijenhuis, *Properties of polym.-their correlation with chemical structure: their numerical estimation and prediction from additive group contributions*, 4th completely rev. Edition, (Elsevier, 2009).
- [100] D. François et al., *Mechanical Behaviour of Mat.-Volume 1-Micro and Macroscopic Constitutive Behaviour*, (Springer, 2012).
- [101] Z. Zhou et al., *Polym. Eng. & Sci.* 35, 4, p. 304-309, (1995).
- [102] J. D. Menczel et al., Chapter 1 in *Dynamic mechanical analysis (DMA) in the thermal analysis of polym.-Fundamentals and Applications*, edited by J. Menczel, R. B. Prime, (Wiley, 2009).
- [103] L.E. Nielsen, *Mechanical Properties of Polym.*, (Van Nostrand Reinhold, 1962).
- [104] L. E. Nielsen, R. F. Landel, *Mechanical Properties of Polym. and Composites*, 2nd Edition, (Marcel Dekker, 1994).
- [105] R. P. Chartoff, *Thermoplastics in thermal characterization of polymeric Mat.*, 1st Edition, edited by A. E. Turi, (Academic Press, 1997), p. 483-743.
- [106] B. Wunderlich, *J. Phys. Chem.* 64 , 1052, (1960).
- [107] B. Wunderlich, *Thermal Analysis* , p. 417-431, (Academic Press , 1990).

- [108] K. H. Grote, J. Feldhusen, *Dubbel - Taschenbuch für den Maschinenbau*, (Springer, 2007).
- [109] P. Elsner et al., *Kunststoffe, Eigenschaften und Anwendungen*, 7., neu bearbeitete und erweiterte Auflage, (Springer, 2008).
- [110] E. Hering et al., *Taschenbuch der Mathematik und Physik*, (Springer, 2009).
- [111] C. E. Koning et al., *Polym.* 37, 25, p. 5619-5625, (1996).
- [112] F. Bedoui et al., *Acta Materialia* 54 , 6, p. 1513-1523, (2006).
- [113] A. Keller, *Rep. Prog. Phys.* 31, p. 623-704, (1968).
- [114] R. P. Daubeny et al., in the *Proceedings R. Soc. London, Ser. A, Math. Phys. Sc.* 226, (1954), p. 531-542.
- [115] K. Akhtar, H. Zhang, *Int. J. of plasticity* 17, p. 1167-1188, (2001).
- [116] R. B. Dupaix, M. C. Boyce, *Polym.* 46, p. 4827-4838, (2005).
- [117] B. Cosson et al., *Int. J. Mat. Forming* 5, p. 39-53, (2012).
- [118] A. C. Middleton, *J. Appl. Polym. Sci.* 79 , p. 1825-37, (2001).
- [119] G. H. Michler, *Electron Microscopy of Polym.*, (Springer, 2008).
- [120] M. Itoa et al., *Polym.* 42 , p. 241-248, (2001).
- [121] M. Itoa et al., *Polym.* 39, p. 4593-4598, (1998).
- [122] N. S. Murthy et al., *Polym.* 36, 20, p. 3863-3873, (1995).
- [123] M. Danielssona et al., *J. of the Mech. and Phys. of Solids* 55, p. 533-561, (2007).
- [124] A. Dwivedi, *Army Research Laboratory Report No. ARL-TR-5899*, 2012.
- [125] Y. W. Chang, J. H. Cheng, *J. of the Chinese Inst. of Engineers* 35, 8, p. 967-978, (2012).
- [126] Z.X. Hou et al., *J. of Mat. Proc. Tech.* 151, p. 312-315, (2004).
- [127] Y. Nanzai et al., *JSME Int. J.* 41, 1, p. 31-39, (1998).
- [128] M. Heilig et al., *Microsyst. Tech.* 17, 4, p. 593-600, (2011).
- [129] M. C. Boyce, R. B. Dupaix, *Mech. of Mat.* 39, p. 39-52, (2007).
- [130] M. Jerabek et al., *Polym. Testing* 29, p. 407-416, (2010).
- [131] Y. Wang et al., *Adv. Eng. Mat.* 13, 10, (2011).
- [132] Y. A. Çengel, J. M. Cimbala, *Fluid mechanics-fundamentals and applications*, 1st Edition , (McGraw-Hill, 2006).
- [133] G.H. Menary et al., *Polym. Eng. and Sci.* 50, 5, p. 1047-1057, (2010).

- [134] H. J. Trussel, Chapter 8 in *The Essential Guide to Image Processing*, edited by A. Bovik, (Elsevier, 2009).
- [135] M. Petros, Chapter 13 in *The Essential Guide to Image Processing*, edited by A. Bovik, (Elsevier, 2009).
- [136] M. Jerabek et al., *Polym. Testing* 29, p. 407–416, (2010).
- [137] C. G'Sell et al., *Int. J. of Solids and Struct.* 39, p. 3857–3872, (2002).
- [138] J. Lemaitre, R. Desmorat, *Eng. Damage Mechanics*, (Springer, 2005).
- [139] ASM International, *Characterization and Failure Analysis of Plastics*, p. 204-210, (2003).
- [140] A. Hensel, T. Spittel, *Kraft- und Arbeitsbedarf bildsamer Formgebungsverfahren*, (Deutscher Verlag Grundstoffindustrie, 1978).
- [141] M. Spittel, T. Spittel, *Deformation parameters*, (Springer-The Landolt-Börnstein Database, 2009).
- [142] P. H. Mott et al., *Scientific Instruments Review* 78, (2009).
- [143] Hibbit, Karlsson & Sorensen, Inc. *Abaqus-User's Manual Ver. 6.11* (2011).
- [144] M. G. Cockcroft et al., *J. Inst. Metals* 96, p. 33-39, (1968).
- [145] M. Oyane et al., *J. Mech. Work. Tech.* 4, p. 65-81, (1980).
- [146] P. Brozzo et al., in the *Proceedings of the 7th Biennial Conference Int. Deep Drawing Research Group 7.1*, (1972), p. 3.1-3.5.
- [147] L. Părăianu et al., *Adv. Methd. in Mat. forming*, p. 151-165, (Springer, 2007).
- [148] M. Saboori et al., *AIP Conference Proc.* 1353, p. 301-306, (2011).
- [149] J. Takahashi et al., *Intl. J. mechanical Sci.* 52, p. 266-276, (2010).
- [150] G. Z. Voyiadjis et al., *Int. J. Plasticity*, (2011).
- [151] G. Spathis, C. Maggana, *Polym.* 38, 10, p. 2371-2377, (1997).
- [152] G. Halsey et al., *Text. Res. J.* 15, (1945), p. 295-311.
- [153] G. Anyasodor, C. Hartl, *Key Engineering Materials* 597, (2013), p. 153-158.
- [154] C. Hartl, G. Anyasodor, Chapter in *Micro manufacturing Eng. and Tech.*, 2nd Edition, (2014), accepted for publication.

A. Appendix-Materials Properties at Room Temperature
[9, 99 and 108-114]

	PMMA	PEEK	PEHD	PP	Cu	AL	Air
	Poly-(methyl methacrylate)	Poly-etherether ketone	High Density Poly-ethylene	Poly-propylene	Copper	Aluminum	-
Polymer class	Thermo-plastic: amorphous	Thermo-plastic: semi-crystalline	Thermo-plastic: semi-crystalline	Thermo-plastic: semi-crystalline	Thermo-plastic: amorphous	-	-
Density ρ x 10³ [kgm⁻³]	1.18-1.2	1.3-1.32	0.95	0.90	8.90	2.70	1.29
E-Modulus E (GPa)	2.7-2.9	3.76-3.95	1.07-1.09	1.37-1.58	1.26x10 ⁵	7.2x10 ⁴	-
Poisson's Ratio ν	0.365-0.375	0.378-0.393	0.41-0.427	0.399-0.407	0.35	0.34	-
Tensile Stress at Yield σ_{YT} [MPa]	72.2-79.6	70.3-103	22.1-31	22.5-33.5	450	14	-
Compressive Stress at Yield σ_{YC} [MPa]	75.8-131	118-130	18.6-24.8	39.9-41.9	1.4x10 ⁵	7.5x10 ⁴	-
Elongation at Break [%]	2-7	30-150	150	50	0.02	0.5	-
Hardness [Rockwell M]	80-120	95-105	31-35	59.8-75.8	-	-	-
Fracture Toughness [MPa·m^{1/2}]	0.7-1.6	2.73-4.3	1.52-1.82	1.66-1.75	-	-	-
Melting Temperature T_m [°C]	123-260	322-346	130-137	161-170	1083	660.4	-
Glass Transition Temperature T_g [°C]	96-104	143-157	-125-(-90)	-14-(-6)	-	-	-
Maximum Crystalline Region [%]	0	-	90	75	-	-	-

Coefficient of Heat Transfer λ_h [Wm ⁻¹ K ⁻¹]	-	-	0.38–0.51	0.20	384	221	0.026
Specific Heat Capacity c_p [Jkg ⁻¹ K ⁻¹]	-	-	2100-2700	1800	390	920	1007
Coefficient of Thermal Expansion [10 ⁻⁶ K ⁻¹]	-	-	260-	150	16.8	23.8	-
Water Absorption [% per 24 h]	-	-	< 0.01	< 0.02	-	-	-

Note:

- Mechanical properties are for bulk material at room temperature.
- Melting point: Temperature at which a material turns abruptly from solid to liquid. For polymers, a melting point is only reported for semi-crystalline materials. For the amorphous material listed in the table, the temperature given in the Melting point column is actually the melting temperature required to achieve stable processing characteristics. Melt temperature is one of the processing properties for amorphous material.